Laser Induced Breakdown Spectroscopy (LIBS) as an analytical tool for geological samples

Diana Capela
Mestrado Integrado em Engenharia Física
Departamento de Física e Astronomia
2020

Orientador
Dra. Diana Guimarães, INESC TEC

Coorientador
Prof. Dr. Pedro Jorge, Faculdade de Ciências

U.PORTO

FACULDADE DE CIÊNCIAS
UNIVERSIDADE DO PORTO

Todas as correções determinadas pelo júri, e só essas, foram efetuadas.

O Presidente do Júri,

Porto, _____/_____/_____

UNIVERSIDADE DO PORTO

MASTERS THESIS

Laser Induced Breakdown Spectroscopy (LIBS) as an analytical tool for geological samples

Author:

Diana CAPELA

Supervisor:

Diana GUIMARÃES

Co-supervisor:

Pedro JORGE

A thesis submitted in fulfilment of the requirements
for the degree of MSc. Engineering Physics

at the

Faculdade de Ciências da Universidade do Porto
Departamento de Física e Astronomia

January 7, 2021

" If you have the habit of taking things with joy, you will seldom find yourself in difficult circumstances. "

Roberts Baden-Powell

Acknowledgements

I would like to start by thanking my supervisor, Diana Guimarães, for guiding me during this year, with all the dedication, sharing, concern, and friendship. Your enthusiasm for science is contagious and helped keeping me motivated. You managed to awaken the research bug in me, when I thought that this was not my vocation. Even when you were on maternity leave you always kept in contact and never left me adrift. For all of this, Im grateful to you. My co-supervisor, Prof. Pedro Jorge, was also important for this work, as he contributed with his knowledge in this area every time I needed his help.

On a more personal note, Im grateful to my parents and grandparents for all the love, support and teachings, and for always motivating me to never give up on my goals, and for having a lot of patience for this long period where, even while being at home, I was not so present.

I could never forget to give a special mention to my sweetheart, André, for all the love, help, patience and for being an inspiration to me. You always cheered up to me when things looked less good. Thank you for being part of my life and for being always there.

Thanks also to my friend Célia for all the friendship, for putting up with my outbursts and for knowing that I can always count on you. I am grateful too to Sofia, my friend since the 2nd cycle and may our friendship last forever. I would like to thanks my high school friends, as well as my group of friends that Physics brought together, that are too many to properly mention here.

Thanks to the Clagodiana who despite being in forced stand by, keep the music bug in action.

Thanks to Hugo who, besides being my friend, was also my thesis colleague. He was a true Brothers in Arms!

I could never forget to mention the LIBS team and be thankful for their contribution. In special, Miguel, for all the time you lost teaching me how the system works, even when it broke down and for all the help. Filipe, for always getting along in the setbacks, for all his good mood and for making the laboratory a more pleasant place. Luís Coelho for the profilometry measurements. Luisa, for the exceptional person you are and for the support when I was feeling less well.

Lastly, I would like to thankful INESC TEC and FCT for the Research Initiation Grant with reference AE2020-0038 within the scope of the FLAPSYS, funded by Fundo Europeu de Desenvolvimento Regional (FEDER) through the Operational Programme for Competitiveness and Internationalisation - COMPETE 2020 Programme, and by National Funds through the FCT - Portuguese Foundation for Science and Technology, I.P., project (reference PTDC/EEI-EEE/31165/2017 (POCI-01-0145-FEDER-031165)).

UNIVERSIDADE DO PORTO

Abstract

Faculdade de Ciências da Universidade do Porto
Departamento de Física e Astronomia

MSc. Engineering Physics

Laser Induced Breakdown Spectroscopy (LIBS) as an analytical tool for geological samples

by Diana CAPELA

With the growing importance that Laser Induced Breakdown Spectroscopy has been presenting, and with a wide adoption in various areas, there is a need for a more in-depth study of the LIBS system prototype to be used. This study will provide a detailed analysis of its capabilities and limitations, alongside some ideas to bypass them. Thus, this study begins precisely by addressing the different figures of merit in the system.

Afterwards, work towards through the construction of a tool that allowed the spectral analysis of geological samples which, are of high complexity due to their intrinsic characteristics. To this end, it was necessary to carry out an entire study on the existing spectral databases, NIST and OSCAR, in order to determine the most suited to the conditions of the system, that will be used as a reference. Different algorithms were studied to simulate the baseline of LIBS spectra such as Asymmetric Smoothing of Least Squares (ALSS), Median Filter (MF) and Rolling Ball (RB). The performance of those methods was measured, with the ALSS being the optimal one. Bearing all these points in mind, an analysis tool was then developed which proved to be able to correctly find the elements present in all tested pure samples and 85% of the chemical composition of the studied minerals.

Finally, different geological samples were studied. In the first case study, the existence of Li infiltrations in Turquoise is addressed, in a sample of a hydrothermal vein, composed of Montebrasite, Turquoise and Quartz. To this end, a qualitative analysis was carried out making mappings in the sample. A mapping of LIBS was also carried out on a petrography blade, which was the first successful study of this kind, presenting results in agreement with the expected ones. A study of the damage caused by the laser shots was

made by a microscopic analysis and a profilometry. In the second case study, a differentiation was performed between two minerals of similar chemical composition, Spodumene and Petalite. To do so, a Principal Component Analysis (PCA) was used, with a good performance. The last case study is related to a Li prospection drill hole, 18PNR RC 005, in which it was intended to make a quantification of this element, meter by meter. The goal was to evaluate the viability of extracting Li from the region. A semi-quantitative approach was made, on 3 levels, by applying Neural Networks, resulting in a success rate of 74%. Although just 50% of the samples showed good concentrations of this element, whereby the extraction will not be very viable.

UNIVERSIDADE DO PORTO

Resumo

Faculdade de Ciências da Universidade do Porto
Departamento de Física e Astronomia

Mestrado Integrado em Engenharia Física

Espectroscopia de Plasma Induzido por Laser como uma ferramenta de análise para amostras geológicas

por Diana CAPELA

Com a crescente importância que a Espectroscopia de Plasma Induzido por Laser (LIBS) tem vindo a apresentar, sendo já vasta a sua aplicabilidade em diversas áreas, surgiu a necessidade de desenvolver um estudo mais aprofundado do protótipo de sistema LIBS a utilizar. Este estudo permitirá analisar detalhadamente as suas potencialidades e limitações, assim como desenvolver ideias para contorná-las. Desta forma, o referido estudo começa precisamente por abordar as diferentes figuras de mérito do sistema.

O trabalho passou pela construção de uma ferramenta que permita a análise espectral de amostras geológicas que são de elevada complexidade devido às suas características intrínsecas. Para tal, foi necessário fazer toda uma análise relativa às bases de dados espectrais existentes, NIST e OSCAR, com vista a descobrir qual a que mais se adaptava às condições do nosso sistema, para ser utilizada como referência. Foram estudados diferentes algoritmos para simulação da baseline dos espetros de LIBS, tais como: Suavização Assimétrica dos Mínimos Quadrados (ALSS), Filtro de Medianas (MF) e Bola Rolante (RB), e encontrados métodos para correção do offset daí resultante, tendo-se definido o ALSS como o método mais ajustado ao pretendido. Tendo todos estes pontos em mente, foi então desenvolvida a ferramenta de análise que mostrou ser capaz de encontrar corretamente os elementos presentes em todas as amostras puras testadas e 85% da composição química dos minerais estudados.

Por fim, foram estudadas diferentes amostras geológicas. No primeiro estudo de caso é abordada a existência de infiltrações de Li na Turquesa, numa amostra de um filão hidrotermal, composto por Montebrasite, Turquesa e Quartzo. Para tal, foi realizada uma

análise qualitativa, efetuando mapeamentos na amostra. Foi ainda realizado um mapeamento de LIBS numa lâmina de petrografia, pela primeira vez com sucesso que apresentou resultados de acordo com o esperado. Ainda na mesma amostra, foi feito um estudo do perfil das crateras provocadas pelos disparos sendo, para isso, realizada uma análise microscópica e uma profilometria.

No segundo estudo de caso, foi feita a diferenciação entre dois minerais de igual composição química, a Espodumena e a Petalite, com recurso a algoritmos de Análise da Componente Principal (PCA) que mais uma vez apresentou resultados muito positivos.

O último estudo de caso é referente a um furo de prospeção de Li, 18PNR RC 005, no qual se pretendeu fazer uma quantificação deste elemento, metro por metro, com vista a verificar se a zona é viável para uma possível extração. Optou-se por uma abordagem semi-quantitativa, em 3 níveis, com recurso a algoritmos de *machine learning* com utilização de redes neurais, tendo-se obtido uma taxa de sucesso de 74%. No entanto, uma vez que apenas 50% das amostras apresentaram boas concentrações deste elemento, a extração não será muito viável.

Contents

List of Figures

Glossary

ALSS	Asymmetric Least Squares Smoothing
CCD	Charged Coupled Device
CF-LIBS	Calibration-Free LIBS
EDS	Energy Dispersive Spectroscopy
FWHM	Full Width Half Maximum
ICP-MS	Inductively Coupled Plasma Mass Spoctrometry
LIBS	Laser Induced Breakdown Spectroscopy
LOD	Limit of Detection
LOQ	Limit of Quantification
LR	Logistic Regression
MF	Median Filter
MPL	Multi-Layer Perceptron
Nd:YAG	Neodymium-doped Yttrium Aluminium Garnet
PCA	Principal Component Analysis
PCR	Principal Component Regression
PLS	Partial Least Squares
RB	Rolling Ball
RDS	Relative Standard Deviation
SVR	Suport Vector Regression
XRF	X-Ray Flourescence

Chapter 1

Introduction

1.1 Motivation

Minerals and rocks are powerful natural resources that are used today on a large scale to allow the quality of life and comfort that everyone got used to having. Its analysis is of extreme importance in several areas such as mining, environmental monitoring, toxicology and even for the geoscience.

Geological samples containing Lithium (Li) have been attracting more and more attention particularly due to their importance in renewable energy industry. The explosive adoption of Li batteries that started in 2010, caused the greatest change, driving forward the demand for this material. In Figures 1.1 and 1.2, there is a depiction of the huge revolution that took place in Li markets, in a small time frame of approximately 20 years.

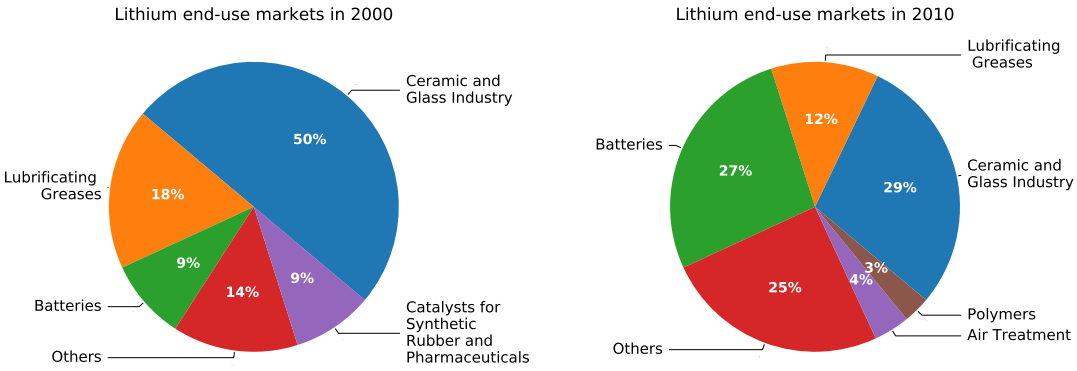

FIGURE 1.1: Lithium end-use markets in 2000 and 2010, according to U.S. Geological Survey [1, 2].

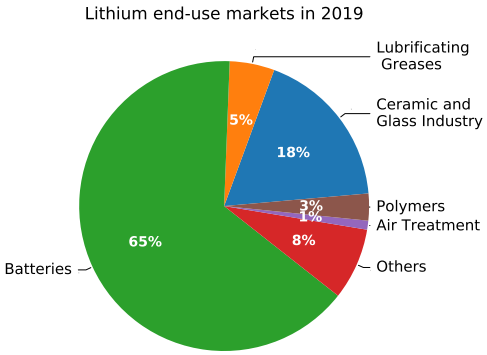

FIGURE 1.2: Lithium end-use markets in 2019, according to U.S. Geological Survey [3].

This spread of the Li used for batteries production in a worldwide scale has created the necessity of increasing the capacity of both Lithium exploration and subsequent treatment. In Figure 1.3, it can be seen the evolution of the global consumption and production of Lithium over a period of 13 years, from 2005 to 2017.

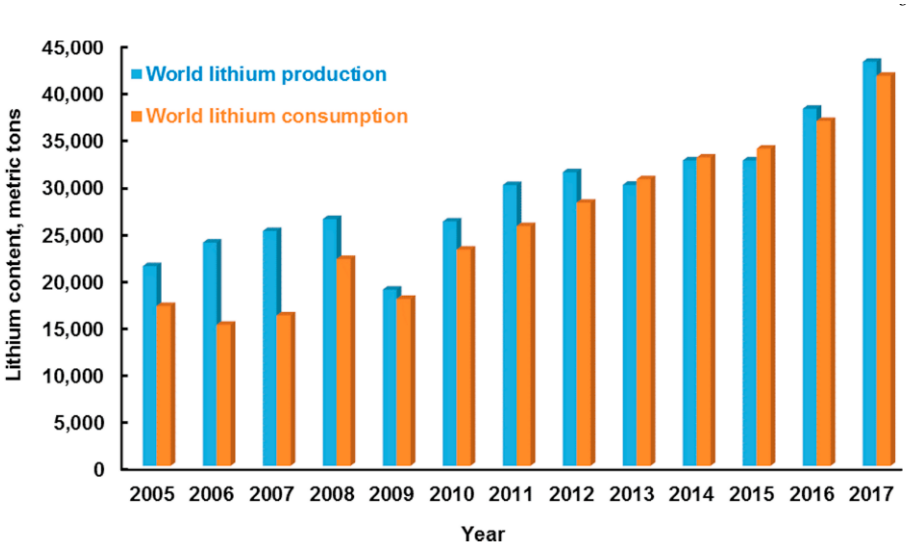

FIGURE 1.3: Lithium production and consumption - an estimation. Graphic from [4].

From Figure 1.3, it is possible to see that between 2005 and 2009 the demand was not always constant and it was always inferior than the production rate. Although, from 2009 onward, there was a sharp growth of Lithium consumption at a worldwide scale, eventually surpassing the production in a short period of 3 years, from 2013 to 2015, making clear the large economical interest in the exploration of Li. In this regard, it is possible to see the relevance of understanding the mineralogical reserves from our country. By

studying a wide array of Li-bearing samples, it is possible to have a clearer view of the location and quantity of the reserves, allowing for an evaluation of the economic feasibility of extracting them.

TABLE 1.1: Lithium reserves, per country, in 2019 according to Unites States Geological Survey [3]

Country	Reserves (Ton)	Country	Reserves (Ton)
Chile	8 600 000	Canada	370 000
Australia	2 800 000	Zimbabwe	230 000
Argentina	1 700 000	Brazil	95 000
China	1 000 000	Portugal	60 000
United States	630 000	Other	1 100 000

Lithium reserves in Portugal are placed in the 10 largest ones, as seen in Table 1.1. However, when dealing with the extraction of the material, the ecological footprint of the operation must not be forgotten, so that there is a minimization of the environmental impact.

With this in mind, the Laser Induced Breakdown Spectroscopy, henceforth LIBS, emerges as a viable tool to perform such an analysis. It allows a cost reduction and a maximization of the profitability in all the Li extraction, mining and recycling process, contributing to a decrease in the ecological footprint. The conventional analytical techniques such as X-Ray Fluorescence, XRF, has difficulties in detecting light elements (Z*<11) such as H (Z=1), He (Z=2), Li (Z=3), Be (Z=4) and C (Z=6), due to two main factors: the atmosphere absorption of the low energy fluorescent X-rays emitted by these elements and the relevant effect of Auger emission. The Inductively Coupled Plasma-Mass Spectrometry, ICP-MS could be a good option, however, it is very limited, due to the impossibility of being used in field. On the other hand, LIBS can successfully detect Li (atomic number, Z=3), and other low Z elements [5, 6] and can be applied in situ, transforming this method into a potential technique for qualitative and quantitative analysis of Li minerals.

1.2 LIBS - A Brief Description

The Laser Induced Breakdown Spectroscopy is a promising method of Chemical Analysis. It consists in focused pulsed Laser shots, with high energy and short pulse duration (frequently in the nanosecond order), that reaches the sample surface and produces plasma.

*Atomic Number

This laser-matter interaction causes an atomic excitation, ionization and recombination. When the de-excitation occurs, there is light emission containing the spectral information of the sample that can then be recorded by a spectrometer. Using this spectrum the sample composition can be determined [7, 8].

This methodology is a very versatile tool, as shown by its applications to a large number of scientific areas. As an example, it has been applied in medicine, for the study of chemical composition of gallstones [9] and teeth samples [10], in geology [5], in archaeology and cultural heritage, for study of pigments, stones and metals [11, 12], in agriculture, for studies about plant leaves, pastures and vegetables [13], in food, for quality and compositional analysis of food products [14], in space exploration, mainly in Martian rock analysis [15], in pharmaceutical products [16] and in deep ocean [17].

LIBS presents a set of interesting features that make the method much more attractive than other approaches [18, 19]. First, the analysis can be done in a short amount of time, as there is a real-time spectral response. Second, there is little to none sample preparation. Third, only a very small amount of sample is needed and, fourth, it can be made in situ. Lastly, and most interestingly from an economical point of view, it is a non-expensive technique comparing with other gold standard analytical techniques.

1.3 Overview of LIBS in geological samples

Geological samples, such as rocks and minerals, are complex materials. They are the oldest elements in the Earth, storing a small piece of the planet formation. They are composed by many chemical elements, resulting in spectra with hundreds of lines that require time-consuming analysis to be decoded. Furthermore, their characteristics, i.e., color, hardness, opacity, roughness, grain size and homogeneity, influence the line intensity from shot-to-shot [20, 21].

Currently, with the ascension of the LIBS, mainly in the last decade, there are many studies made in this field. In 2011, Pace *et al.* used it to study minerals and rocks in order to determine the characteristic lines of Earth's crust major components, such as, Si, Al, Fe, Ca K and Mg [20]. In 2014, Mcmillan *et al.* performed geochemical mapping using LIBS in a Copper ore, as well as provenience determination of a set of rubies from Madagascar and Tanzania, using Principal Component Analysis and Partial Least Squares Regression algorithms. This work has shown success rates higher than 95% [21]. In 2015, Sweetapple *et al.* performed a LIBS study of Lithium in Pegmatite minerals, making in situ

mappings and analyzing their textural information [5]. Streubel *et al.*, in 2016, applied the LIBS method to scanning a drill core in order to qualify and quantify the resources presents in ore deposits and mine residues [22]. In 2017, Hu *et al.* used LIBS to study the Iron concentrations in a set of standard geological samples, originated from United States Geological Survey (USGS). For the concentration determination, artificial networks were used [23]. Zhang *et al.*, in 2018, analyzed a set of minerals and rocks in order to classifying them into calcium sulfates ($CaSO_4$), iron oxides (Fe_2O_3) or other. For this purpose, a multivariate analysis with Principal Component Analysis was used [24]. In 2019, Harmon *et al.* showed how LIBS can be used for grain size analysis, geochemical fingerprinting, as well as, qualitative and quantitative analysis applied to geological samples, with the possibility of being made in situ [6].

These are just some examples, highlighting the capability of this technique when applied to the geological field. Although, spectral treatment techniques, including baseline and matrix effect corrections, still need to be improved in order to allow higher precision in shot-to-shot measurements, solving the quantification problems that are often present in these systems.

1.4 Goals of the thesis

The goals of this thesis can be separated in the different items. First, assessing the performance of the LIBS prototype system used in this study. Second, developing an algorithm to search the presence of chemical elements in geological samples. Third, perform analysis of different geological samples.

In the first point, a more in-depth analysis will be made, in order to determine the limitations of the system, with regard to the spectrometer and the laser used in the LIBS system. Its figures of merit will be studied alongside with a quality control analysis.

Regarding the search elements tool for geological samples, before the development of the tool itself, a study about the chemical databases and the atmosphere lines will be performed, as well as the analysis of the best baseline removal method for LIBS spectra. In the same line of thought, a LIBS interface will be made in order to simplify the LIBS system handling.

Lastly, some real geological samples will be analyzed, with the goal of system optimization for Li measurements.

Chapter 2

Laser Induced Breakdown Spectroscopy

In this chapter, basic concepts of Laser Induced Breakdown Spectroscopy will be reviewed, as well as a brief history and evolution of this technique. In addition, the LIBS system used during this thesis will also be showcased.

2.1 History and Evolution

Laser Induced Breakdown Spectroscopy's history began with the birth of the first Ruby pulsed laser, in 1960, by Teodore Mainman [25]. This discovery allowed, in a short time, the creation of the first plasma through laser induction, by Brech and Cross [26].

Three years later, Debras-Guédon and Liodec reported the first analytical study of surfaces using spectrochemical analysis [27]. In 1964, the first laser induced breakdown in gas was observed by Maker *et al.* [28]. Similarly, Runge *et al.* used a pulsed Q-Switched Ruby laser to produce direct spark excitation in metals [29].

In 1966, Young *et al.* presents the characteristics of laser induced in air sparks [30]. Between 1964 and 1967, the first commercial instruments, based on laser ablation, were produced by Zeiss, Jarrel-Ash and JEOL. The excitation of the sample was made by a spark followed by a laser pulse to ablate the sample [7, 31].

From the 80's, with the improvement of the components used, as CCDs and lasers with higher beam quality, this technique began to be used for different applications such as: detection of Beryllium in air, filters, detection of hazardous gases, aerosols and liquids and analysis of steels and metals in solid forms and soils all of them developed by Cremers

and Radziemski [32–38]. In 1981, the technique was, for the first time, coined as LIBS [7, 31].

In the following decade, there was an increase in its applications and developments. In 2000, Zayhowski reports the working of a passively Q-Switched Nd:YAG laser [39]. In the same year, a LIBS system is implemented into a NASA Mars rover [7].

Lastly in the XXI century, appears the first books about this method, and an explosive number of peer-reviewed articles about this method were published. LIBS began to be applied in many different settings, such as biology, medicine and chemistry analysis [7].

2.2 Technique Description

LIBS typical setup is composed by a pulsed laser, a focusing lens, a light collection system, a detection system and a computer, as shown in Figure 2.1.

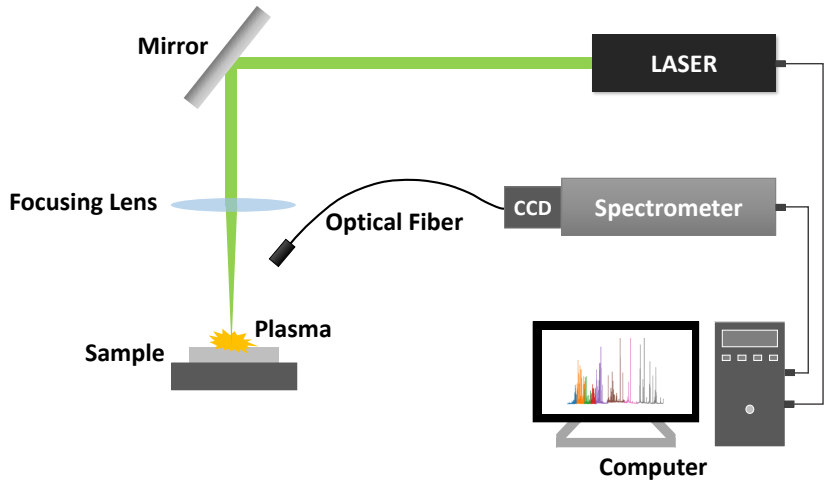

FIGURE 2.1: Typical setup of a LIBS system.

The laser is responsible for the production of high energy densities, with the help of focusing lens that will decrease the spot size of the laser in the sample surface, thus increasing the energy density. There are different types of lasers that can be used in LIBS, each with its own specific characteristics, as can be seen in Table 2.1. However, the most popular is the Nd:YAG laser [15, 20, 40–44].

TABLE 2.1: Lasers usually used in LIBS systems and theirs specifications [7].

Type	Laser Medium	Wavelength (nm)	Pulse Width (ns)	Repetitions Rate (Hz)
Nd:YAG	solid	Fundamental: 1064	6-15	ss to 20
		Harmonics: 532, 355, 266	4-8	
Excimer	gas	XeCl : 308	20	ss to 200
		KrF: 248		
		ArF:194		
CO_2	gas	10600	200	ss to 200
Microchip	solid	1064	<1	1-10 K
Fiber Laser	solid	Nd^{+3}: 900	<50	25-500 K
		Pr^{+3}: 1060		
		Er^{+3}: 1540		

The light collection system is composed by one or more optical fibers alongside with collimators, which are used to direct the light. The optical fibers will guide the signal to the CCD detector, where the light is dispersed into the spectral range. Finally, a computer is responsible for controlling the laser shooting, the spectrometer gate and for performing the signal acquisition.

2.2.1 Laser Emission and Properties

The abbreviation LASER means Light Amplification by Stimulated Emission of Radiation. Laser light has unique characteristics that are fundamental for plasma formation:

- Monochromaticity - the laser light is emitted in a specific and very limited width of wavelengths;
- Directionality - the laser emission produces a collimated beam;
- High Radiance - the radiance is defined as optical power (radiant flux) per unit area and solid angle; its units are Wcm^2sr^1. The LIBS laser energies usually varies between 10 to 500 mJ (in case of Nd:YAG lasers) that, when combined with an highly focused beam, originates a high radiance.

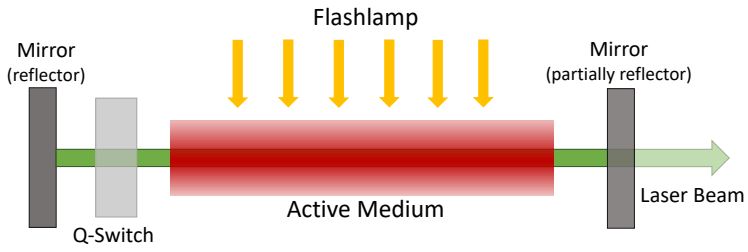

FIGURE 2.2: Operation of a Q-Switched Nd:YAG laser.

The operation of a Q-Switched Nd:YAG laser, typically used for LIBS, is described by Figure 2.2. The Q-Switching method is used to produce higher energy laser pulses with short pulse duration. The process begins with the excitation of the active medium by the Flashlamp, that works as a pumping light. The Nd^{3+} ions, present in the YAG crystal, can absorb a reduced part of this light, and when the excitation energy is higher than the binding energy of the electron in E_0, their electrons pass from the E_0 to the pump level, E_3 as illustrated in Figure 2.3.

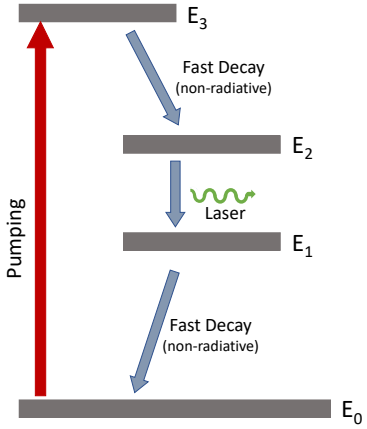

FIGURE 2.3: Schematic of a four level laser. Graphic adapted from [45].

As this level is unstable, there is a quick decay of the electrons to the E_2 energy level, that is a meta-stable level. As level E_2 has a longer life time when comparing to E_3, the number of electrons in this level increases, resulting in an inversion of the population, due to the upper level E_2 having more population than the lower one, E_1. When one electron in the E_2 level decays to E_1, it emits one photon (spontaneous emission), that can interact with the other electrons in E_2 level and trigger the same process (stimulated emission). While the Q-Switch is opaque, the resulting photons are prevented from traversing the entire cavity formed by the two mirrors. Thus, the stimulated emission is blocked and the losses into the cavity are higher. As the pumping continues, the population inversion increases into the active medium, translating into an increase of gain with time. When the Q-Switch is activated, by either becoming transparent or due to a shutter being opened (in case of an active Q-Switch), the photons can go over the resonant cavity, stimulating the photon emission and originating a very short and high-power laser pulse. A part of this pulse passes through the partial transparent mirror, giving up the laser emission [7].

Although the process above refers to an active Q-Switch, there are also passive Q-Switches in which the triggered Q-Switch is replaced by an absorber material. In this

case, the absorber becomes temporarily transparent when the intensity of spontaneous emission exceeds a certain threshold [7].

In both cases, the Q-Switch process is based on a rapid change of the Q-factor. This factor represents the quality of laser cavity, that is calculated as the ratio between the energy stored into the cavity and the energy losses per optical cycle. At the beginning, the Q-Switch is deactivated, the losses in the cavity are higher, the laser emission cannot occur and the gain into the cavity increases, due to the pumping light. In this regime only spontaneous emission occurs, originating a fluorescence light into the active medium. When the Q-Switch is activated, the losses are drastically decreased. At this time, the light is amplified by the round trips into the cavity and stimulated emission occurs, generating a large increase of laser radiation power. Under the regime of gain saturation, the laser pulse peak is reached, and there is a decrease of both the energy in the cavity and the pulse's power, as shown in as illustrated in Figure 2.4 [46, 47].

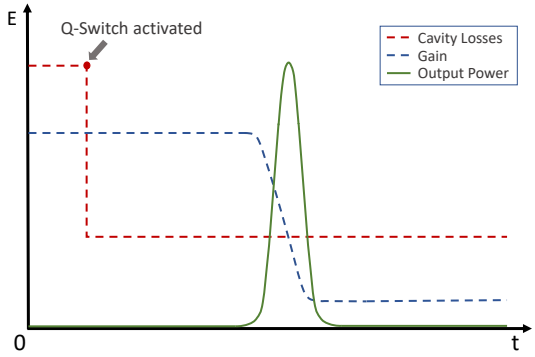

FIGURE 2.4: Laser cavity gain and losses evolution when Q-Switch is activated. From the Q-Switch activated time, the output power begin to increase, but very slowly, reaching its maximum when gain saturation occurs. According to [47].

In the case of active Q-Switches, it is important to understand the meaning of the Q-Switch Delay and how it is related with the laser energy.

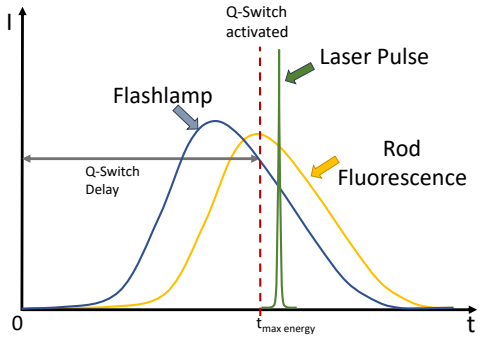

FIGURE 2.5: Q-Switch Delay and Flashlamp relation.

As can be seen in Figure 2.5, the Q-Switch Delay is defined as the time between the beginning of the Flashlamp pumping routine and the moment in which the Q-Switch is activated, allowing for the laser to emit. When the pumping begins, after a certain short time, the fluorescence into the Rod increases, due to the increase of the population inversion, until a saturation value is reached. At this point, if the Q-Switch is activated, the laser pulse energy will reach its maximum value. However, if the Q-Switch is activated whilst the Flashlamp current is decreasing and the cavity fluorescence is decreasing too, the power into the cavity will be lower and the laser pulse energy is smaller. In table 2.2 the relation between the laser pulse energy and Q-Switch Delay, for a Quantel CFR200 laser, can be seen.

TABLE 2.2: Pulse energy values and respectively Q-Switch Delays for a Quantel CFR200 laser. The energy values were obtained using an Power Meter.

Q-Switch Delay (μs)	Pulse Energy (mJ)	Q-Switch Delay (μs)	Pulse Energy (mJ)
410	3.7	320	63.2
400	6.9	310	72.3
390	15.2	300	80.7
380	21.0	290	91.2
370	28.0	280	101.2
360	35.1	270	111.5
350	41.7	260	121.9
340	48.5	250	132.3
330	56.2	240	143.2

Observing the Table 2.2, can be concluded that the energy of the laser beam is higher as the Q-Switch Delay is shorter.

2.2.2 Plasma Formation, Emission and Properties

When a high energy pulsed laser interacts with the matter there is plasma formation. When focused onto the surface, the laser beam causes a localized and rapid heating of the focal spot, by energy absorption, promoting the dissociation, excitation and ionization of the matter constituents (Figure 2.6 - a)). In this process, when the temperature reaches the boiling temperature, a small amount of sample matter is ablated and vaporized, forming an assembly of atoms and giving rise to a crater in the sample surface (Figure 2.6 - b)) [7, 8]. When this assembly of atoms absorbs more energy, it promotes ionization and creates plasma (Figure 2.6 - c)).

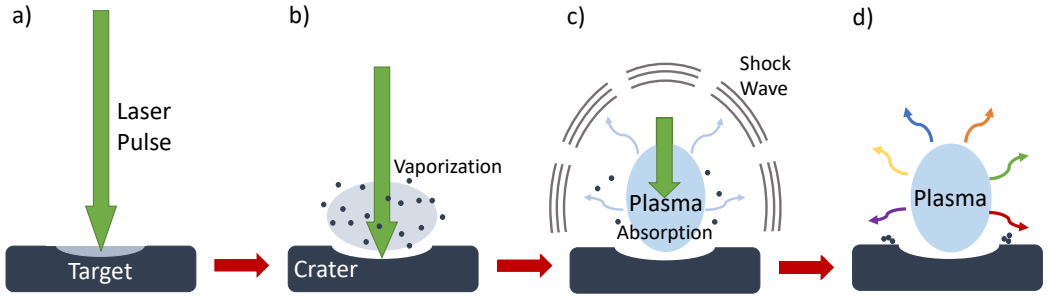

FIGURE 2.6: LIBS Plasma formation description.

When the plasma cools down, a de-excitation process occurs in which atoms, ions and, with a lower probability, molecules, suffer transitions between two bounded states (bound-bound). During this operation, there is emission of photons, giving rise to the traditional spectral lines (Figure 2.6 - d)). However, two more events happen simultaneously, which are responsible for the appearance of a continuous background: Bremmstrahlung radiation and recombination radiation. The Bremmstrahlung radiation (free-free transition) is a result of the emission of photons caused by electron acceleration and deceleration processes, during collisions with atomic particles, e.g. ions. Under such conditions, the electron loses kinetic energy while it is deflected by another charged particle and, consequently, emits a photon [48, 49].

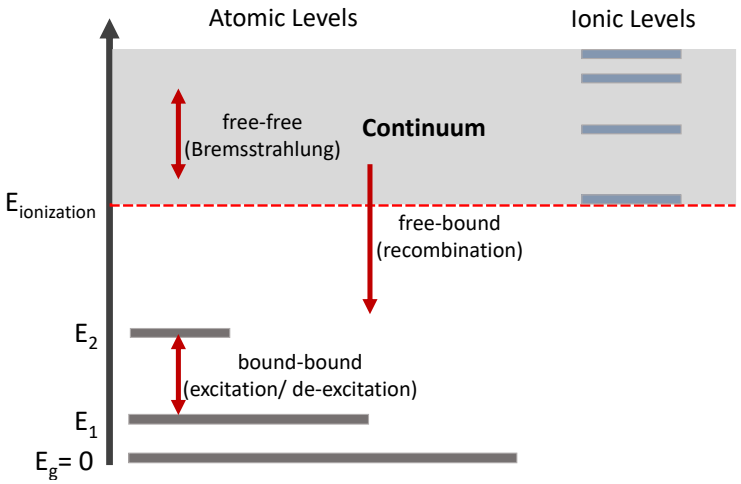

FIGURE 2.7: Atomic and Ionic transitions that typically occur in plasma radiation.

In turn, recombination radiation (free-bound transition) occurs when a free electron is captured by an upper bounded ionic or atomic level, transforming its excess of kinetic energy in the form of a photon [8, 48].

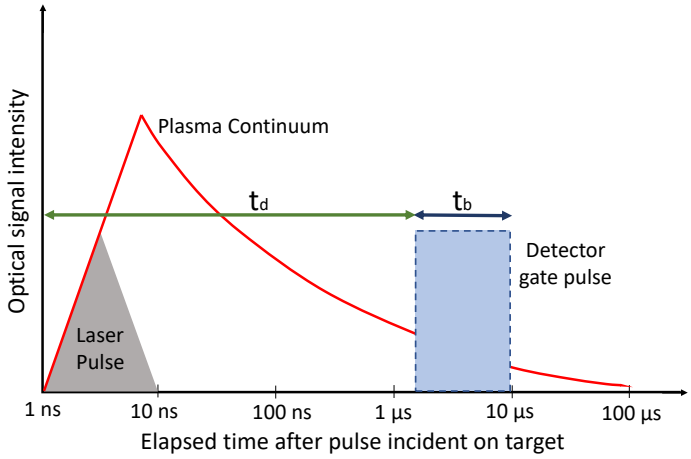

FIGURE 2.8: Plasma temporal evolution with optimal time scale for a plasma started in air, with a Nd:YAG laser pulse, with duration between 5 to 10 ns. The t_d represents the delay time between the laser pulse starts and detector gate open and the t_b represents the detector acquisition time. Graphic adapted from [7].

Figure 2.8 illustrates the plasma evolution, starting from the moment when the laser emission begins. The t_d represents the time that passed between the beginning of the laser emission and the opening of the detector gate. The t_b represents the amount of time that the detector gate is open, which is equivalent to the acquisition time. The continuum background decays quickly over time, in such way that from t>1 μs its intensity is less than half of its maximum value. As the spectral lines have a longer life span, the acquisition window can be adjusted in order to minimize the contribution of the spectral background [7].

The plasma is characterized by its temperature, typically above 5000 K and by the electron densities higher than $10^{16}\ cm^{-3}$. The spectral line intensities can be determined by the Equation 2.1 [7],

$$I_{\lambda_{ki}} = \frac{hcNg_kA_{ki}}{4\pi\lambda_{ki}Z(T)}e^{\frac{-E_k}{k_BT}} \tag{2.1}$$

where $I_{\lambda_{ki}}$ is the line intensity, λ_{ki} is the line wavelength, h is the Planck constant, c is the light velocity in vacuum, N is the total number density, g_k is the statistical weight, A_{ki} is the transitions probability between the energy levels k and i, E_k is the energy of the upper level, k_B is the Boltzmann constant, T is the plasma temperature and Z(T) is the partition function [7]. The partition function of a system in thermodynamic equilibrium represents its statistical properties and can be calculated using the Equation,

$$Z(T) = \sum_{i=1}^{N} g_i e^{-\frac{E_i}{k_BT}} \tag{2.2}$$

where N is number of possible states [50].

Through the Boltzmann distribution, the relative number densities between two distinct energy states can be calculated as indicated in Equations 2.3 and 2.4, relative to the ground state and to an arbitrary state, respectively [7],

$$\frac{N_j}{N_0} = \frac{g_j}{Z(T)} e^{\frac{-E_j}{k_B T}} \tag{2.3}$$

$$\frac{N_j}{N_i} = \frac{g_j}{g_i} e^{\frac{-(E_j - E_i)}{k_B T}} \tag{2.4}$$

where N_0 is the atomic density number and N_i and N_j are the ionic density numbers of ions in i and j ionization states.

Taking the logarithmic from the Equation 2.1 and with a small rearrangement, Equation 2.5 is obtained in the linear form ($y = mx + b$). Making LIBS measurements of different line intensities relative to distinct energy upper levels, its plot can be made, the so-called Boltzmann plot. The plasma temperature can then be obtained through the slope of a linear regression: m=$-\frac{1}{k_B T}$ [7, 51].

$$ln\left(\frac{I_{\lambda_{ki}} \lambda_{ki}}{g_k A_{ki}}\right) = -\frac{1}{k_B T} E_k + ln\left(\frac{hcN}{4\pi Z(T)}\right) \tag{2.5}$$

The electron density, N_e, in its turn, can be obtained by the Saha Equation 2.6 [7],

$$\frac{N_{r+1} N_e}{N_r} = \frac{2(2\pi m_e k_B T)^{\frac{3}{2}}}{h^3} \frac{2Z(T)_{r+1}}{Z(T)_r} e^{\frac{-E_{ion}}{k_B T}} \tag{2.6}$$

where m_e is the electron mass, E_{ion} is the ionization energy for each neutral species, N_r and N_{r+1} are the number density of ionized species in ionization states r and N_{r+1}, and $Z(T)_r$ and $Z(T)_{r+1}$ its their partition function, with r being the ionization state number, taking as a 0 for neutral atoms [7].

2.2.3 Detection and Light Collection

The light collection systems typically used for LIBS are based on gratings and Charge Coupled Devices, CCDs. The light, collected by the optical fibers, is directed to the grating that is responsible for the spatial dispersion of the incident light and diffracting it into different directions, as illustrated in Figure 2.9 [52, 53].

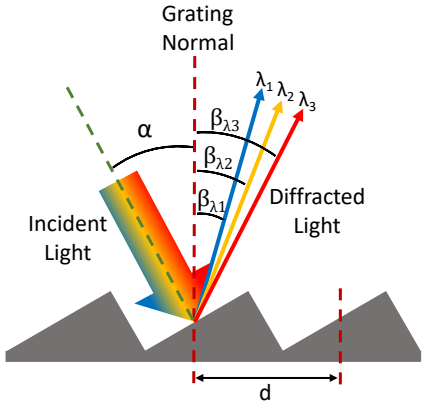

FIGURE 2.9: Schematic of a diffraction grating.

Each wavelength has a particular diffraction angle, as described by the grating equation, given by the equation 2.7,

$$m\lambda = d(sin\alpha + sin\beta) \tag{2.7}$$

where m is the diffraction order, λ the incident wavelength, d the grating period, α the incidence angle and β the diffraction angle. Unwanted diffraction orders are filtered out.

The diffracted wavelengths are guided to the spectrometer CCDs. These devices are composed by one- or two-dimensional arrays of pixels that are light sensitive. Thus, when the diffracted wavelengths reach its surface, they fall into a given pixel. Within it, the photons are collected during a certain amount of time, the integration time. After it has passed, the photons are read out from the device, pixel by pixel, forming the spectra. How much higher be the incident light in a certain wavelength, higher will be the correspondent line intensity [7, 53].

2.3 LIBS Setup

The LIBS home-made setup used in this study is composed by a Q-Switched Nd:YAG laser (Quantel CFR200), with a pulse duration of 8 ns and 200 mJ of maximum energy, operating at the fundamental wavelength, 1064 nm. The beam diameter is 4.74 mm, with a quality factor of 5.32. A set of lens and mirrors is employed to focus the laser pulses onto the sample surface. The convergent lens of the instrument has a focal distance of 20 cm and is followed by a sapphire window, positioned 10 cm from the lens, presenting a refractive index of 1.7545. The laser beam arrives to the sample surface with a spot size

in the order of hundreds of micrometers. Two diode lasers are used to signalize the laser-sample alignment and to indicate the ideal Z position for the sample, due to their crossing point being close to the lens focal distance. The sample holder is based on a set of three translation stages, with two of them being controlled by a motion controller, that receives movement instructions from `Python`, allowing for bi-dimensional movement, in the x and y direction. The third one is responsible for movement in the vertical (z) component.

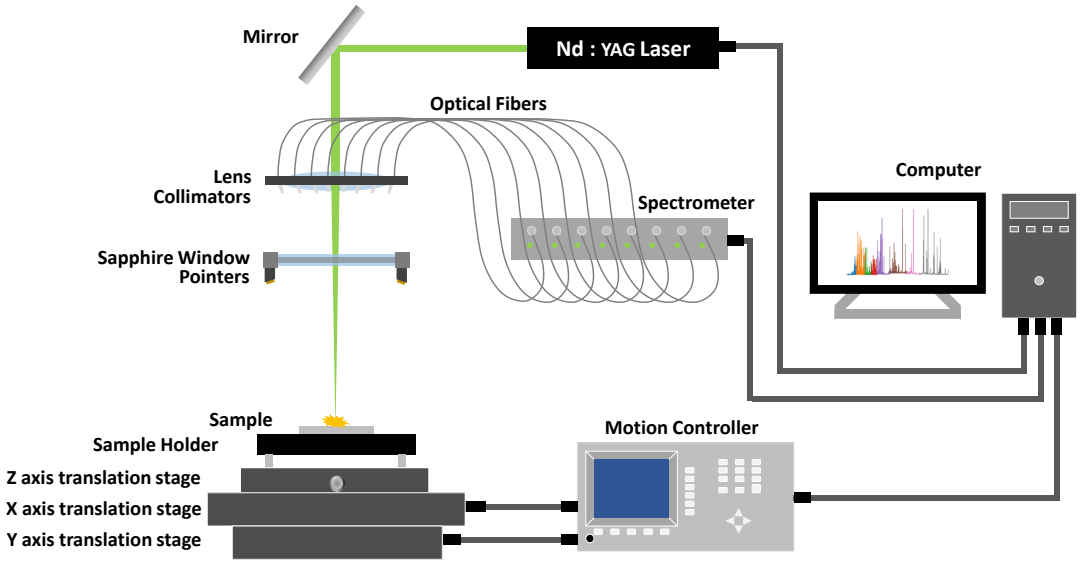

FIGURE 2.10: LIBS system schematic.

An Avantes CCD Spectrometer was used to collect the plasma light. It covers a wavelength range from 180 to 920 nm, spread over 8 independent channels, each connected to its own optical fiber. The set of optical fibers are composed by seven Sarspec Optical Fibers UV/VIS*, with 200 cm of length, 200 μm of core diameter and stainless stell protection tubing and the 8-th is an Avantes FC-UV200-1.5-SR Optical Fiber †, with 150 cm of length, 200 μm of core diameter and solarization resistant. The collimators are placed at the edge of optical fibers. Due to them and the fibers, the plasma signal is guided to each CCD of the spectrometer. Lastly, the Avasoft software ‡ was used to collect the spectral data. A representative scheme can be seen in Figure 2.10.

*http://sarspec.com/docs/Optical_Fibers_Probes_Sarspec.pdf
†https://www.avantes.com/introductions/961-introduction-fiber-optics/468-product-codes
‡https://www.avantes.com/products/software/item/223-avasoft-basic-software

Chapter 3

LIBS Prototype Performance Assessment

In this chapter, aspects related to the system performance will be studied. First, the resolution of the different spectrometer channels will be evaluated, as well as its overlapping regions. Afterwards, the laser energy drift and its Full Width Half Maximum will be assessed for different energies. Finally, a quality control evaluation will be made and figures of merit such as limit of detection and precision will be determined.

3.1 Spectrometer

The spectrometer used in this LIBS system has a wavelength range between 177.84 and 926.62 nm and is composed by eight 2048-pixel CCD detectors, that translate into 8 channels with different resolutions and distinct bandwidths.

TABLE 3.1: Wavelength range, grating and optical resolution of each spectrometer channel, according to the manufacturer.

Channel	1	2	3	4	5	6	7	8
Wavelength Range (nm)	177.84 to 254.69	250.50 to 315.62	309.95 to 363.91	359.78 to 402.42	400.42 to 493.65	493.21 to 625.79	619.67 to 727.33	725.36 to 926.62
Grating	UF-3600 lines/mm	UF-3600 lines/mm	UF-3600 lines/mm	UF-3600 lines/mm	VE-2400 lines/mm	VD-1800 lines/mm	VD-1800 lines/mm	NC-1200 lines/mm
Optical Resolution (nm)	0.06	0.06	0.05	0.05	0.08 - 0.11	0.10 - 0.16	0.10 - 0.16	0.18 - 0.22

In Table 3.1 the wavelengths distribution across the eight independent channels is presented. From the 5-th channel (inclusive) until the last, there is an increase in the wavelength range and a decrease in the grating number of lines per mm, resulting in a poorer resolution. The grating efficiency is also an important parameter that depends on the wavelength and on the incidence angle of the light. The efficiency curves of each grating referred in Table 3.1 can be seen in Figure 3.1.

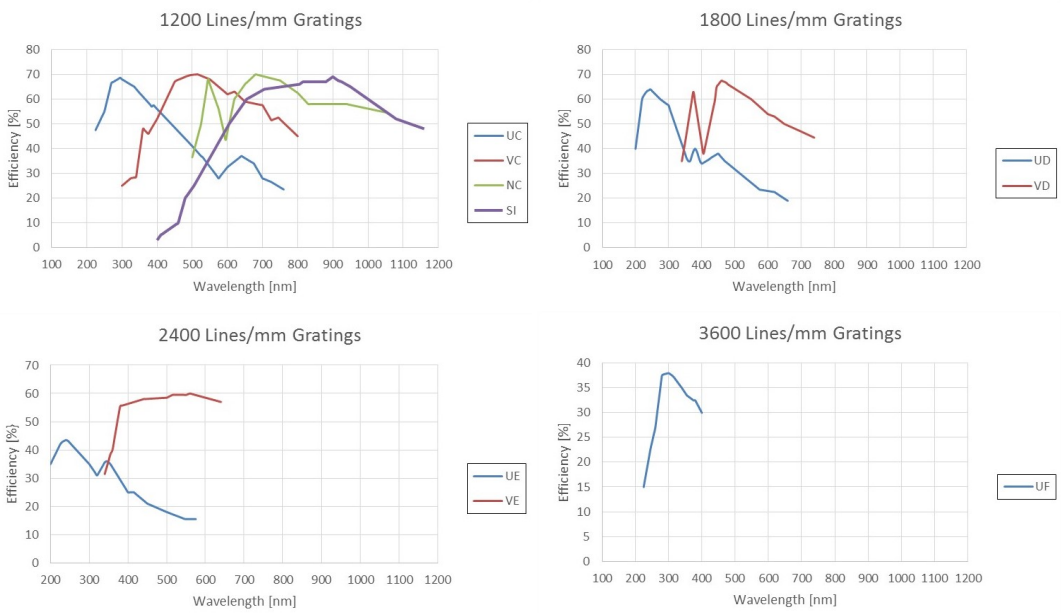

FIGURE 3.1: Efficiency curves for each spectrometer grating. Images from [54].

In Figure 3.1, it is clear that the grating efficiency suffers sudden variations with the change of wavelength, not following a clear trend. This leads to an inhomogeneous response at the peak energies, over the entire range, with the wavelength being the deciding factor, resulting in different efficiencies and resolutions for each channel, as will be seen with more detail.

3.1.1 Channel CCDs Resolution

The CCDs resolution for each spectrometer channel was determined considering the wavelength calibration of each individual pixel. This resolution was calculated by subtracting the wavelength of a given point from its adjoining point. The result can be seen in Figure 3.2.

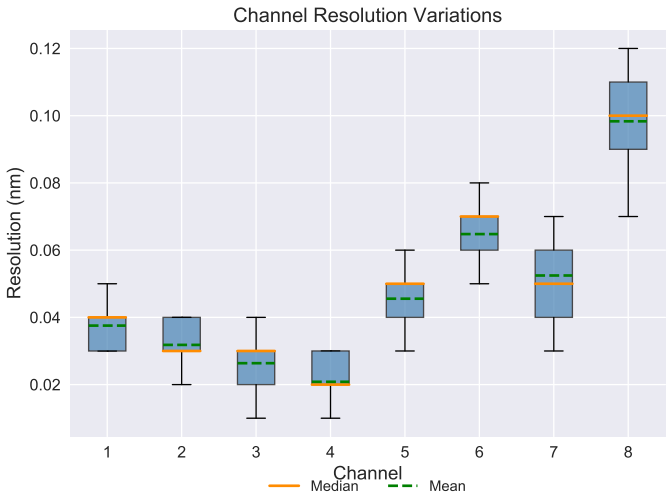

FIGURE 3.2: CCD resolution variations for each spectrometer channel. The orange line represents the median value of the resolution, the green line represents the mean value and the bars the outliers.

Figure 3.2 highlights a limitation of the LIBS system: the resolution is not only variable from channel to channel, but also undergoes very large variations within each channel. The best resolution values are found in the first 4 channels of the spectrometer, with values ranging from 0.01 nm to 0.05 nm and covering wavelengths in the interval [180 - 402] nm. The channel that stands out for presenting the worst resolution is channel 8, where it varies between 0.07 nm and 0.12 nm.

TABLE 3.2: CCD channels resolution.

Channel	1	2	3	4	5	6	7	8
CCD Resolution (nm)	0.03-0.05	0.02-0.04	0.01-0.04	0.01-0.03	0.03-0.06	0.05-0.08	0.03-0.07	0.07-0.12

The low resolution present in the last channels of the spectrometer may cause serious problems in the identification of elements that emit in those wavelengths, as different lines will be detected in the same pixel. This information will be taken in consideration in the development of a tool for element search in the spectra.

3.1.2 Channels Overlap

Paying attention to the wavelengths range of each spectrometer channel, all channels have an overlap region, i.e., the end value of the previous channel is not lower than the first of the following one. Thus, there are ranges of wavelengths that are included in two different channels. In Table 3.3, those regions can be seen.

TABLE 3.3: Overlap regions between the spectrometer channels.

Channels	1-2	2-3	3-4	4-5	5-6	6-7	7-8
Overlap Wavelengths (nm)	250.50 to 254.69	309.95 to 315.62	359.78 to 363.91	400.42 to 402.42	493.21 to 493.65	619.67 to 625.79	725.36 to 727.33

In this sequence, when a given line is emitted in an overlap region, both channels will ideally detect it, providing two peaks for the same line. In this case, it is important to know which peak should be chosen. Thus, a study was performed with a set of pure targets and discharge lamps, to discover what is the best channel for each overlap region.

The discharge lamps used were: Ar, Kr, He, Hg, Ne and AvaCal (AvaLightCal-Mini* composed by Ar and Hg), and the information relative to pure targets† can be found in Table 3.4.

TABLE 3.4: Information of the pure targets used to find the optimal channel.

Target ID	Element	Reference	Purity (%)
Cr	Chromium	C6-9000-D146	99.999
Cu	Copper	C8-9000-D70	99.999
Fe	Iron	I4-9000-D29	99.95
Si	Silicon	S4-9000-D50	99.999
Ti	Titanium	T8-9000-D22	99.995

For all targets, a LIBS analysis was performed with a Q-Switch Delay of 310 μs. A clean shot with a Q-Switch Delay of 410 μs was also performed before the shots in order to remove the dirty on sample surface. For the lamps, an integration time of 1000 ms was used, allowing for the detection the highest possible number of spectral lines. However, the AvaCal lamp required shorter integration times, so 200 ms was chosen.

To perform this, it was made a comparison between the theoretical NIST values and the experimental lines detected, selecting the experimental lines closest to the theoretical. For this process, a `Python` script was developed.

*https://www.avantes.com/products/light-sources/item/1151-avalight-cal-mini-spectral-calibration-source

†www.testbourne.com/pure-metal-targets - accessed in February 2020

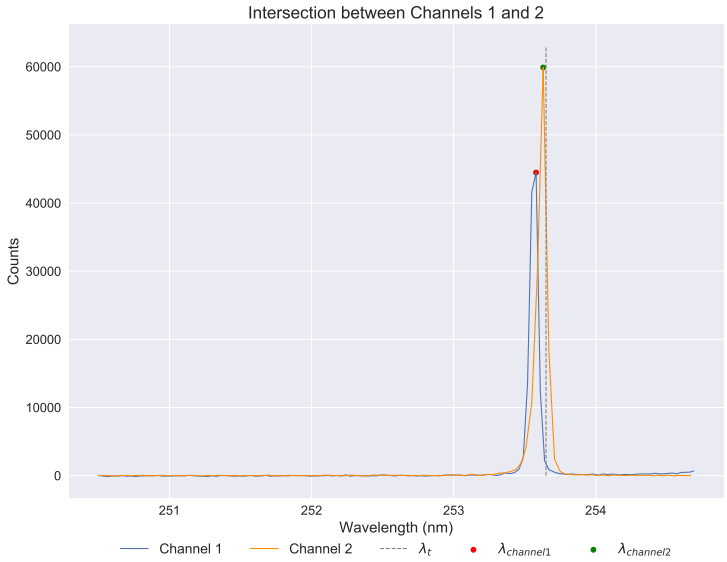

FIGURE 3.3: AvaCal spectrum in overlap region between channel 1 and 2.

For each overlap region, priority was given to the discharge lamp results, because they are not influenced by the atmosphere, and to the highest peak intensities. The obtained results are shown in Table 3.5. An illustrative graphic of an overlap zone, obtained with the AvaCal lamp, is given in Figure 3.3.

TABLE 3.5: Best Channel for each channels overlap. The '—' represents situations without detected peaks or with insufficient information.

		Sample	Channels Overlap						
			1-2	2-3	3-4	4-5	5-6	6-7	7-8
Best Channel for each Overlap	Targets	Cr	—	3	3	—	5	—	—
		Ti	1	3	3	—	—	—	—
		Cu	—	—	—	—	—	—	—
		Si	—	—	—	—	—	—	—
	Lamps	Ar	—	—	—	—	—	—	7
		Kr	—	—	—	—	—	7	—
		He	—	—	—	—	—	—	—
		Hg	—	3	—	—	—	—	—
		Ne	—	—	—	—	—	7	—
		AvaCal	2	3	—	—	—	—	7
Best Channel			2	3	3	—	5	7	7

As can be seen in Table 3.5 the best channel for all overlap regions was found with the exception for the 4-5 overlap. To try to solve this problem, a mineral with high Cesium (Cs) concentration, Pollucite (27.98%, according to [55]), was chosen. Cs has emission

lines at 400.56, 401.49 and 401.49 nm, that correspond to the overlap region. However, none were found by the spectrometer.

As the overlapping regions are formed by the less sensitive areas of the gratings, the response to those wavelengths can be considerably weaker, and may not even exist, as evidenced by the overlap between channel 4 and 5. This problem may be solved, in the future, with the purchase of a Cesium discharge lamp. Although, it is not relevant for the case studies of Li, as there is no emission of Li lines in this wavelength range.

The results obtained will be integrated in all the studies performed from now on.

3.2 Laser Pulse Study

The effect of different parameters, such as system temperature, Q-Switch delay and number of repetitions, on the laser pulse shape was assessed, in order to know how the system performance can be affected by them. This study allows to a general idea about the laser stability and how it can influence the measurement results and consequently the system precision. It is to note that, all the values of laser energy or power mentioned in this analysis are relative and not absolute.

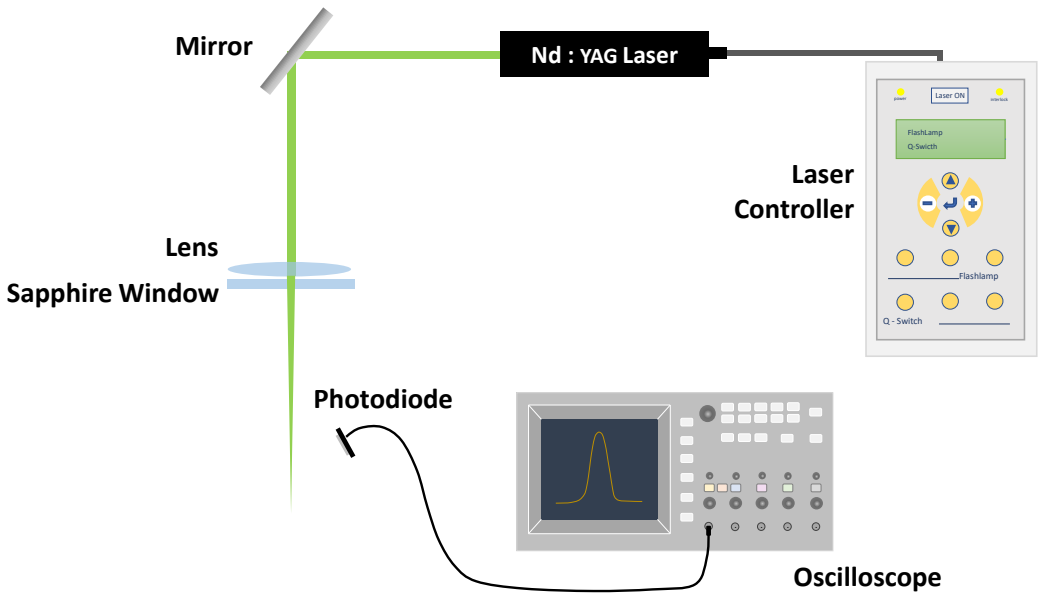

FIGURE 3.4: Setup for laser pulse study.

For the study, an OptoElectronic Components photodiode, InGaAs based (reference GAP168), covering wavelengths from 800 nm up to 1700 nm, was used. The photodiode was placed away from the laser beam focus, and parallel to it, in order to get the laser

impulse by diffuse reflection, also called scattering, as seen in the schematic of Figure 3.4. In this case the shots are made in air, since no sample was used. To collect the pulse forms, a four channel Agilent Technologies oscilloscope was used, reference DSO1024A, with a sample rate of 2 GSa/s and 200 MHz of bandwidth.

The pulse energy was obtained by the integration of the pulse area. The power of the pulse was calculated using Equation 3.1

$$P = \frac{E}{\Delta t * R_{Load} * R_{Pho} * G} \tag{3.1}$$

where P is the pulse power in Watt (W), E is the energy of the pulse in Volt.second (V.s) (obtained by the integration of the pulse form), Δt is equal to the full width half maximum (FWHM) of the pulse in seconds (s), R_{Load} is the impedance of the oscilloscope in Ohm (Ω), R_{pho} is the responsivity of the photodetector in Ampere per Watt (A/W) and G is the circuit gain. As there is no interest in absolute power measurements but, instead, only on relative ones, the gain factor can be safely discarded. The responsivity was estimated to be $\sim$0.55 A/W, using a second-degree polynomial regression made with the information provided by the photodiode datasheet indicated in Table 3.6 and illustrated in Figure 3.5.

TABLE 3.6: Photodiode responsivities according to the datasheet.

Wavelength (nm)	Responsivity (A/W)
850	0.2
1300	0.9
1550	0.95

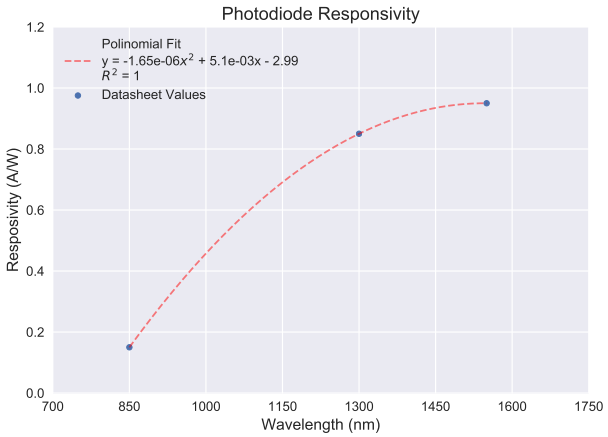

FIGURE 3.5: Fotodiode responsivity values and polynomial fit approach.

3.2.1 Pulse Power Behavior with System Temperature

The dependence of pulse power values with temperature is of utterly importance, as consecutive measurements typically result in heating of the system. A Q-Switch Delay of 370 μs was chosen to perform the study and the Flashlamp was working from start to finish without any interruption. The laser cooling group temperatures (CG) were recorded, and the results can be found in Figure 3.6.

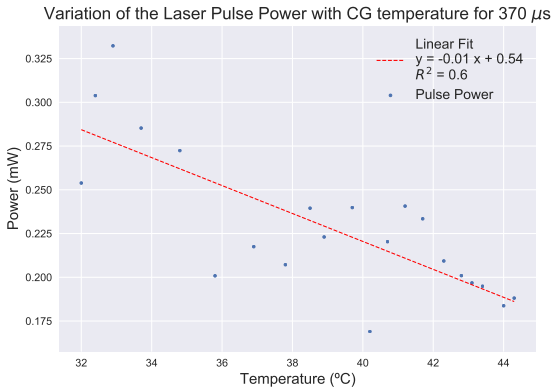

FIGURE 3.6: Variation of the laser pulse power with the system temperature. The red line represents the linear regression.

The results in Figure 3.6 show that the pulse power follows a quasi-linear trend, as can be seen by its correlation coefficient of 0.6. A downwards trend is evident in the data, suggesting that the rise in the temperature leads to weaker pulses. As during the measurement sets the laser working cannot be interrupted there is no way to prevent this increase in temperature from happening. Although, it should be taken in account that there will be a decrease in the intensities of the final spectra when compared to the initial ones.

3.2.2 Pulse Power Behavior with Q-Switch Delay

In the sequence of the previous study, there was an analysis of the pulse power behavior for different Q-Switch Delays. As the intent was to study it in the maximum power condition and, due to the rapid increase of the temperature, the minimum CG temperature at which the measurements were performed was 33.1 °C.

A range of Q-Switch Delays was studied, between 410 and 310 μs and for each Q-Switch Delay, 3 pulses were recorded and their mean was calculated. These mean results can be seen in Figure 3.7.

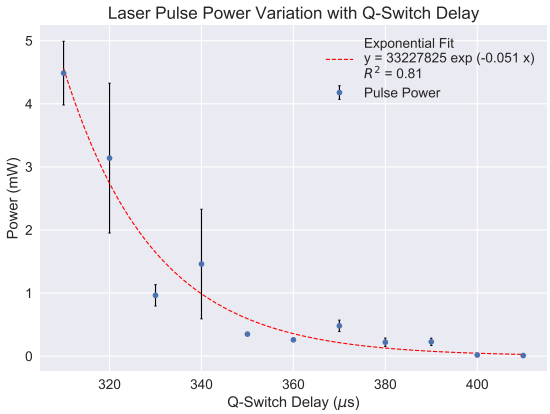

FIGURE 3.7: Variation of the laser pulse power with Q-Switch Delay.

The results proved to follow an exponential behavior with a determination coefficient (R^2) of 0.81. The highest pulse power values were found for the lowest Q-Switch Delays, as expected. The pulse shape for the different Q-Switch Delays showed a large number of oscillations, however a Gaussian shape was always perceptible, as can be seen in Appendix B.1.

3.2.3 Pulse Power Variation with Number of Shots

The study started with the variation of the pulse power for twenty consecutive measurements, after warming up, at a CG temperature set to a value of 33.1 °C. The procedure was repeated for two different Q-Switch Delays: 370 μs and 340 μs that corresponds to energies of 28 and 48.5 mJ, respectively, and that are typically used to perform Lithium detection. For each Q-Switch Delay, twenty shots were made.

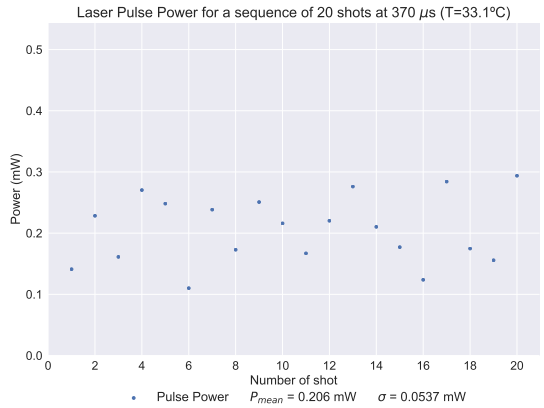

FIGURE 3.8: Laser pulses for a set of twenty measurements with Q-Switch Delay of 370 μs.

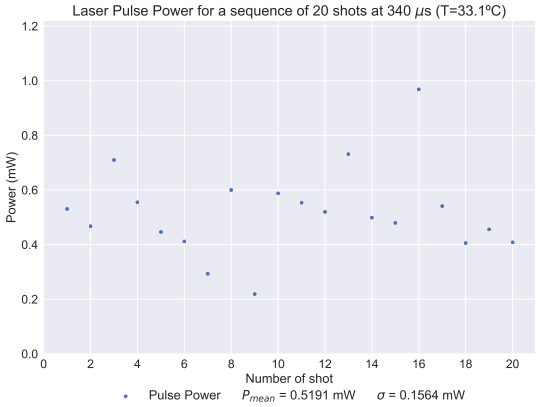

FIGURE 3.9: Laser pulses for a set of twenty measurements with Q-Switch Delay of 340 μs.

Figures 3.8 and 3.9, relative to Q-Switch delays of 370 μs and 340 μs, reveal that the laser pulse power has a standard deviation of 0.03mW and 0.16mW, corresponding to percentual relative standard deviations (%RSD) of 26% and 30%, respectively.

So, it is possible to conclude that the laser pulses showed larger oscillations. Furthermore, the data dispersion increases with the decrease of the Q-Switch delay and the pulse variability is between the 20% and 30%. However its results may have been influenced by reflections into the chamber captured by the photodetector and the dust released by the Fe blade used to protect the stages. Thus, these values are not only consequence of the influence of the laser precision itself.

3.2.4 Pulse Width Behavior with Q-Switch Delay

According to the information on the Quantel CFR200 Laser manual *, the laser has a pulse duration of 8 ns. This parameter is important in the determination of the laser power density, also called irradiance (W/cm^2), due to larger laser durations lead to lower power densities. To determine the experimental pulse duration, a study of the Full Width Half Maximum (FWHM) for different Q-Switch delays between 410 to 300 μs, in steps of 10 μs, was made. For each Q-Switch value, 3 shots were made and, once again, their mean and standard deviation values were calculated.

In Figure 3.10, the results obtained are shown.

*https://www.quantel-laser.com/en/products/item/cfr-200-400-mj–133.html

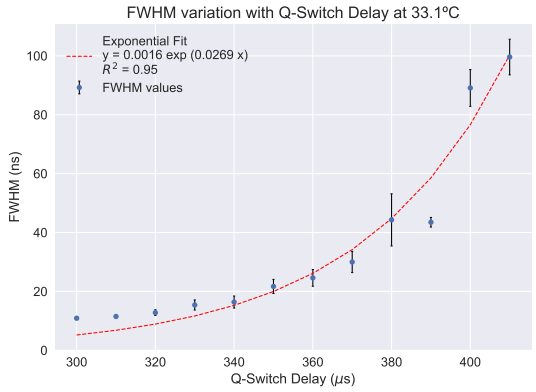

FIGURE 3.10: Variation of the FWHM with Q-Switch delay. The red line represents the exponential fit.

The FWHM presents an exponential behavior, with a clear tendency to decrease the pulse width for lower Q-Switch delays, i.e., for more energetic pulses. The manufacturer value of 8 ns was never met and the closest value was 10.5 ns for 300 μs. For lowest energies, there are laser pulses up to twelve times longer, which is not at all desired, because the irradiance may not be enough to form plasma in a given sample that has higher plasma threshold value.

3.3 Quality Control Evaluation

Quality control evaluation is an important step to monitor the performance of analytical runs. The development of a quality control scheme is a good laboratory practice and can help detecting, reducing and correcting deficiencies in a laboratory setting. With this in mind, a Testbourne Ltd pure metal target of Iron* (ref: I4-9000-D29) with a purity of 99.95%, was used as a quality control sample. Measurements were performed every day the instrument was used.

The protocol for the realization of this study is presented in Figure 3.11.

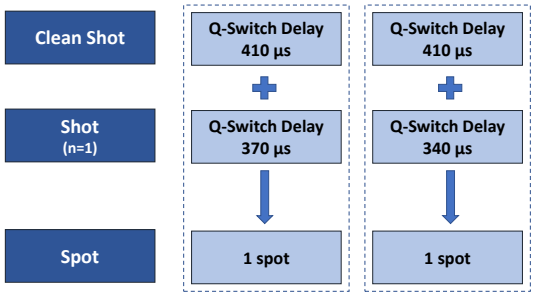

FIGURE 3.11: Experimental protocol for Quality Control study.

*More information in http://www.testbourne.com/pure-metal-targets

This protocol was executed in the beginning and end of the planned experiments for the day, frequently coinciding with the beginning and end of the day.

3.3.1 Iron lines selection

According to the literature (Table 3.7), several lines are used to identify Fe in geological and environmental samples.

TABLE 3.7: Fe lines used in literature.

Paper	Wavelength (nm)	Reference Database
Qualitative Analysis and Plasma Characteristics of Soil from a Desert Area using LIBS Technique [40]	438.35	NIST
	440.48	
	441.51	
Determination of elemental concentration in geological samples using nanosecond Laser Induced Breakdown Spectroscopy [56]	302.00	NIST
	358.12	
	404.58	
	427.18	
	428.24	
	430.79	
	433.57	
	437.59	
	438.35	
	440.48	
	441.51	
	517.16	
	522.72	
	526.95	
	527.04	
Analysis of Minerals and Rocks by LIBS [20]	275.1	Unknown
Classification of Geological Samples based on Soft Independent Modeling of Class Analogy using LIBS [24]	251.81	NIST
Handbook of Laser Induced Breakdown Spectroscopy [7]	248.33	Unknown
Study on Emission Spectral Lines of Iron, Fe in LIBS on Soil Samples [43]	374.94	NIST
	374.55	
	381.71	
	382.18	
	404.58	

Taking these values as a starting point, an observation of these wavelengths in NIST and OSCAR databases was made. After the validation from both databases, there was a search for the same values in LIBS experimental spectra. In both cases, lines too far from

the referenced literature value (more than 0.12 nm), were discarded, as well as lines with very low counts (under 1000 counts).

When assigning specific lines to an element, it is necessary to analyze if a given line is not also present in the spectral signature of other elements. For example, the LIBS chamber of the prototype used in this study has a known contamination of Na, presenting spectral lines at wavelengths that can interfere with Fe ones. Using the Na NIST spectrum as a reference, all the lines that were present in both, experimental Fe and Na NIST spectra, were discarded. Lastly, the peaks with highest counts, without self-absorption, i.e., singlet peaks, and no other peaks close-by, were selected.

The study revealed that the best Fe lines are 430.79 nm, 438.35 nm and 440.48 nm.

3.3.1.1 Fe Lines Peak Area

For each of the selected lines, the peak area was calculated using the set of wavelengths comprised between the local minimum to the left and right of the central wavelength and its intensisty values. The %RSD and the variation in the mean value in the beginning and end day measurements were determined. The results obtained can be found in Table 3.8. The same study was performed for the peak height, but the results showed worst %RSD values, so in this type of study is advisable to use the peak area instead of peak height values.

TABLE 3.8: Mean, %RSD and variation between beginning and end of the day measurements, along thirty days, for the Fe Lines mentioned in the literature.

Q-Switch Delay (μs)		430.79 nm			438.35			440.48		
		Mean	%RSD	Variation beg-end (%)	Mean	%RSD	Variation beg-end (%)	Mean	%RSD	Variation beg-end (%)
340	beg	1334	22	5	1750	20	3	988	19.6	- 1
	end	1411	38		1806	16		981	16	
370	beg	636	22	14	885	19	10	505	21	6.0
	end	736	18		979	16		537	18	

As can be seen in the tables above, the %RSD values were mostly in the orders of 20%, being within the laser precision. So, the beginning and end of the day measurements are, in most cases, statistically equal and the percentual variation throughout the day is contained in the laser variation.

Finally, the best Fe spectral line to perform a systematic quality check, was selected 438.35 nm based on the best %RSD value and greater peak area.

3.3.2 Total Spectrum Area

The spectrum total area was determined by a discrete sum of all intensities. The results can be observed in Figure 3.12.

FIGURE 3.12: Total spectrum area behavior, over time, for Q-Switch Delay of: Top - 370 μs; Bottom - 340 μs.

With the analysis of the entire spectrum, over the time, an increasing tendency was observed. This is confirmed by the linear regression performed for both Q-Switch delays, always having a positive slope. This temporal analysis was calculated in terms of variation in relation to the initial value and the results obtained are shown in Table 3.9.

TABLE 3.9: Mean, standard deviation, %RSD and temporal variation of the total spectrum areas.

Q-Switch Delay (μs)		Mean	Standard Deviation	%RSD	Temporal Variation (%)
340	ini	241591	41046	17	39
	end	241151	32237	13	29
370	ini	129118	13622	11	25
	end	136504	12720	9	18

With regard to the comparison of end of day and beginning of day measurements, one more time, the results are statistically equal, as the values of %RSD are within the laser precision as referred Subsection 3.2.

However, it is possible to conclude that the temporal variation is significant, due to its values being mostly above 20%. These data were obtained between winter and summer and the increase of the ambient temperature into the laboratory may explain this increase over the time. As follow up to the presented analysis this trend should be studied as the winter approaches, to validate if the trend is the reverse of the current one.

3.3.3 Quality Control Graphics

To process the data obtained, a `Python` script was created. This script creates the graphics with the data points, the average value, the average ± standard deviation and the average ± 2 x standard deviation. The 438.35 nm line was chosen to perform the study. The results obtained between March and July of the current year for 370 μs are in Figure 3.13.

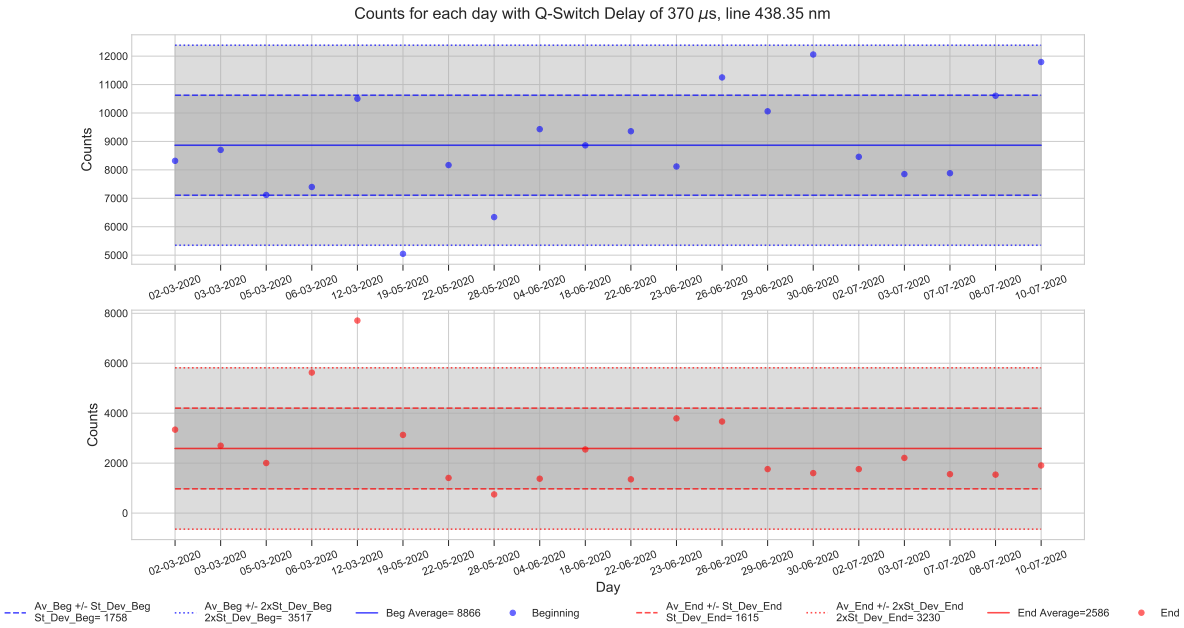

FIGURE 3.13: Quality Control Graphic for 438.35 nm line using a 370 μs Q-Switch Delay. The points representing the day measurements, the continuous line the mean, the dotted line the mean ± standard deviation and the dashed lines the mean ± 2 × standard deviation.

Observing all the graphics, it was possible to concluded that, in the majority cases, the results fluctuate in the window between average ± 2 x standard deviation, as expected.

Although, if a quality control measurement is obtained outside this interval, it should be discarded. After this, the lenses of the system should be cleaned, alongside a verification that the sample is well aligned. The quality control procedure is then repeated and when the measurements is within the expected values, the LIBS is ready to be used.

Once the measurement of the Fe target needs to be made every time that the LIBS system is used, it was necessary to create an user-friendly interface, that would allow to automate the process. The working of this interface is explained in Appendix A.1.

3.4 LIBS instrument performance evaluation

In order to make a characterization of the system performance, a calibration curve and different figures of merit such as limit of detection, precision and accuracy were calculated.

3.4.1 Precision

The precision of a system gives information about the repeatability of the measurements, evaluating the dispersion associated with each set of LIBS data. To evaluate the LIBS system an Iron (Fe) target, with 99.95% (I4-9000-D29)* of purity, was chosen. Similarly to the Quality Control (subsection 3.3.1), the Fe line used was 438.35 nm. Two types of precision were studied: the inter-day precision and the intra-day precision [57]. All the data used in the study was previously treated, having been subtracted the component related to the baseline, using the Asymmetric Least Squares Smoothing algorithm (subsection 4.3.1.2) as discussed in Subsection 4.3.2.

The precision of the measurements can be determined by the relative standard deviation.

3.4.1.1 Intra-day Precision

With the intra-day precision, there was a study of the dispersion of the measurements performed within the same day. As the target is homogeneous, the measurements were made at different spots, guaranteeing the same experimental conditions. If that was not the case, consecutive shots in the same spot would lead to an increase of its depth and, consequently, a decrease of intensity.

*More information in www.testbourne.com/pure-metal-targets

The selected protocol can be seen in Figure 3.14 and it was applied in a single day [58].

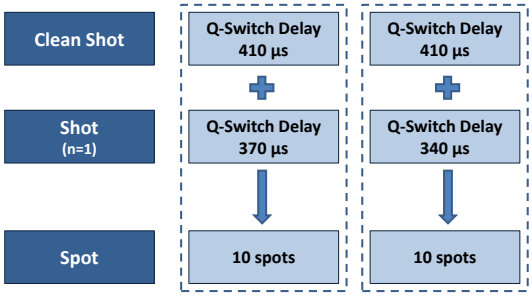

FIGURE 3.14: Protocol chosen to apply the intra-day precision study.

The precision values obtained for each Q-Switch Delay and Fe line can be seen in Table 3.10.

TABLE 3.10: Intra-day precision results for 438.35 nm Fe line.

Q-Switch Delay (μs)	%RSD
370	7.83
340	10.85

The %RSD values obtained were between 7.83% and 10.85%, showing that the data suffers some of variations, however, these are perfectly acceptable values for this type of system.

3.4.1.2 Inter-day Precision

The inter-day precision allows to study the dispersion of the measurements performed in different days.

The protocol used can be seen in Figure 3.15 and it was applied for 5 consecutive days [58].

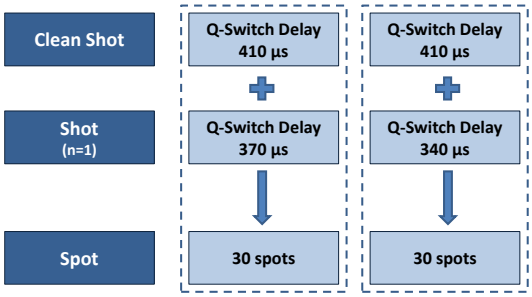

FIGURE 3.15: Protocol chosen to perform the inter-day precision study.

The results of the inter-day precision, for the different Q-Switch Delay values and Fe lines, can be found in Table 3.11.

TABLE 3.11: Inter-day precision results for 438.35 nm Fe line.

Q-Switch Delay (μs)	%RSD
370	23.59
340	15.37

Taking in account both studies and as the worst case must be always considering, all the measurements performed with the LIBS system must be following by the indication $\pm$ 20%.

3.4.2 Calibration Curve

A calibration curve was created with the goal of determining the relation between the spectral intensities (counts) and the Li concentrations, to allow the calculation of the system limit of detection for this element. For this purpose, a set of Li_2CO_3 (Lithium Carbonate) pellets were made, covering a range of Li concentrations between 35 ppm and 2480 ppm. The compound used to dilute the Li_2CO_3 (+99%) (Sigma-Aldrich, LOT SZB92820) concentration was KBr (+99%) (Fluka, LOT I2690), as its spectral lines don't overlap with Li. The compound masses used to made the different pellets can be found in Table 3.12. It is important to stress that the use of these pellets to perform this study represents an ideal condition. With real samples as minerals and rocks, the results would be very distinct.

TABLE 3.12: Masses of Li_2CO_3 and KBr to obtain the desired Li concentration.

Sample ID	KBr (g)	Li_2CO_3 (mg)	Li (ppm)	Error (%)
35 ppm	1.5020	0.56	35.1	0.29
90 ppm	1.5020	1.41	88.1	2.11
175 ppm	1.5034	2.83	176.5	0.86
425 ppm	1.5023	6.85	426.4	0.33
850 ppm	1.5056	13.4	849.5	0.06
2480 ppm	1.5030	40.77	2480.8	0.03

One 100% KBr pellet was also created, which will correspond to the 0 ppm point of the calibration curve.

The pellets were made using a Specac Manual Hydraulic Press* of 15 Ton illustrated in Figure 3.16.

*https://www.specac.com/en/products/sample-prep/hydraulic-press/manual/manual

FIGURE 3.16: Specac Manual Hydraulic Press. Image from https://kaplanscientific.nl/product/atlas-manual-hydraulic-press-15t-25t/.

The tonnage used was 10 Ton. The complete sample preparation is explained with more detail in Appendix C.1.

Because mixing 2 powders normally raises heterogeneity issues, the Li distribution in the pellets was studied. For this, 8x8 point matrix was mapped, with a step of 1 mm between spots and a cleaning shot followed by 3 shots per spot. The Q-Switch Delay selected was 390 μs, in order to be able to analyze two lines from Li, 812.62 nm and 610.37 nm, without any of them being saturated. This study was performed in two pellets: the pellet with 2840 ppm of Li and the pellet with 100% Li_2CO3, for comparison since the last is not mixed with another compound.

The results obtained for 812.62 nm line, normalized to the highest intensity value for each pellet, can be seen in Figure 3.17. Each node of the graphic is result of an average of the 3 shots performed in each spot of the map.

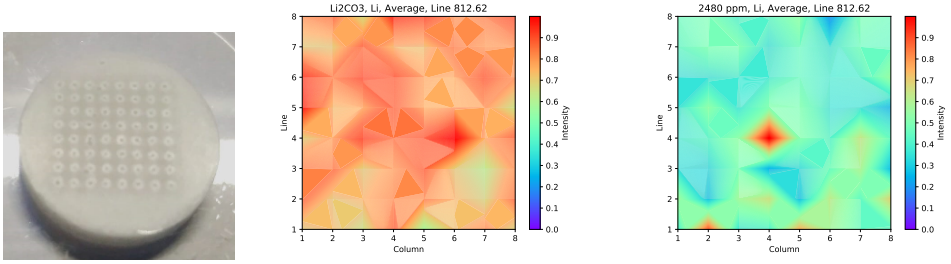

FIGURE 3.17: Left - 2480 ppm pellet and map zone. Homogeneity maps for: Center - 2480 ppm pellet; Right - 100% Li_2CO_3 pellet.

Observing these maps, the graphic of the 100% Li_2CO_3 pellet map appears to be slightly more homogeneous than the previous one so, it is possible to say that the small existing heterogeneities are essentially the result of powders mixture process. To mitigate

this effect, it was decided to use more than one spot for each energy. Thus, for the calibration curve each pellet with a different concentration was measured according to the protocol in Figure 3.18.

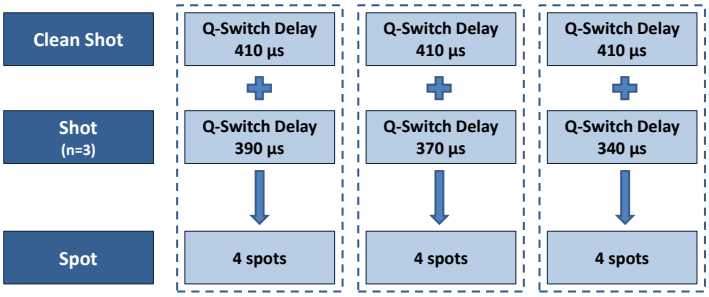

FIGURE 3.18: Protocol applied to each pellet of the calibration curve.

The Li lines used for the study, were 610.37 and 812.62 nm (NIST wavelengths) that are the most intense Li line and an exclusive line of this element, respectively. This guarantees that its emission intensities weren't influenced by any other lines [5].

As can be seen in Figure 3.18, for each Q-switch delay there are 12 spectra. The mean of these spectra was used as the intensity value. The only spectra correction that was applied was the baseline removal, using Asymmetric Least Squares Smoothing method (subsections 4.3.1.2 and 4.3.2)

A univariate method was applied, to find the calibration curve for the pellets data set. In this model the element lines intensity and its concentration in the sample follows a linear regression [19, 59], as indicated in Equation 3.2,

$$I_\lambda = b_0 + b_1 C \tag{3.2}$$

where I_λ is the intensity of the analyte line, C is the known concentration, b_1 is the curve slope and b_0 is a constant. Thus, the mean peak values of interest Li lines versus the respective concentration for the 7 pellets were plotted and a calibration curve was created.

The calibration curves with a correlation coefficient closest to 1 was the calibration curves obtained with a Q-Switch delay of 370 μs and is shown in Figure 3.19. The other Q-Switches, 390 μs and 340 μs, shown worse correlation coefficients of 0.979 and 0.773 for 610.37 nm, and 0.981 and 0.886 for 812.62 nm Li line.

FIGURE 3.19: Calibration Curve obtained for Q-Switch Delay of 370 μs: Left - line 610.37 nm; Right - line 812.62 nm.

As can be seen in Figure 3.19, a correlation value (R^2) of 0.984 and 0.989 was obtained for lines 610.37 and 812.62 nm, respectively. These representing a very good proximity between the experimental values and the linear regression estimated, due to in the literature, values of 0.99 for Li calibration curves were reported [5].

Spectra normalization can be implemented in order to diminish the signal fluctuations caused by energy laser variations, plasma conditions and sample properties itself [60]. Normalization of the peak of interest to the total area of the spectrum [60, 61] was also performed but no improvements were obtained in the R^2, so this method was discarded.

3.4.3 Limit of Detection and Limit of Quantification

The limit of detection (LOD) represents the smallest amount of analyte that is detectable by the system [62]. The LOD can be calculated using the Equation 3.3,

$$LOD = \frac{3\sigma_B}{S} \tag{3.3}$$

where σ_B represents the standard deviation of the background and S the slope of the calibration curve [63].

The limit of quantification (LOQ), on the other hand, is the figure of merit used as a reference for quantification purpose and is given by Equation 3.4 [64].

$$LOQ = \frac{10\sigma_B}{S} \tag{3.4}$$

With the slope of the Li calibration curve for lines 610.37 and 812.62 nm, determined in subsection 3.4.2 and calculating the background standard deviation, a LOD of 6 ppm and 65 ppm was found, respectively. Regarding the LOQ, the values were 21 ppm for

610.37 nm and 215 ppm for 812.62 nm. The 610.37 nm LOD value is in the same order of magnitude of the values found in the literature [65]. No information was found for line 812.62 nm however, because the intensity of this peak is lower it was expectable for the detection limit to be higher. It is important to have these into account and choose the best line according to our interests when trying to detect and quantify lithium: as there are a lot of spectral interferences, maybe 812.62 nm is the best line, but some sensitivity is lost. If no spectral interference is present 610.37 nm should be used.

3.4.4 Accuracy

Accuracy is a measure of how close the LIBS quantification to the reference value is. The accuracy can be quantified by the %BIAS in Equation 3.5,

$$\%BIAS = \frac{x_{exp} - x_{ref}}{x_{ref}} \times 100 \tag{3.5}$$

where x_{exp} is the experimental value, x_{ref} is the reference value, often obtained by ICP-MS (Inductively Coupled Plasma Mass Spectrometry).

This value can be influenced by the laser energy drift, the matrix effect and the calibration curve used to perform the quantification [7]. However, it is very difficult to obtain certified reference materials samples with concentrations spreading through a range of values of interest. Using real samples to do this is another way to address this problem but, it will depend on the case study as will be seen in the next chapters.

3.5 Analysis Overview

The study of the spectrometer resolution shows that there is a loss of resolution in the last channels of the spectrometer raises the need to pay a special attention for the spectral peaks that are emitted at these wavelengths, due to a higher number of distinct wavelengths can fall within the same pixel.

The analysis of the overlapping regions allows the determination of the optimal channel for 6 out of 7 overlap regions. This information will be incorporated and used every time a spectrum is analyzed.

The study of the laser pulse behavior leads to the conclusion that the LIBS laser shows a large number of fluctuations in the pulse power, revealing a decreasing trend in power

with the increase of the temperature and an exponential increase of power with the Q-Switch delay. The laser precision values were between 20% and 30%. An unexpected result of this study was finding that the pulse duration varies with the Q-Switch delay, as it is typically assumed to be constant and independent of the energy. For Q-Switch delays between 410 and 300 μs the 8 ns of pulse was never reached, showing that the 8 ns is probably the pulse duration for the highest laser energy, obtained using a 180 μs Q-Switch delay.

The analysis of the system quality control allows to study the laser drift. The %RSD values obtained for the peak areas for beginning and end measurements were within the laser precision, 20%, being statistically equal, as well as the percentual beginning-end variations. The total spectrum area analysis showed significant temporal variations, with an increase of the total area over the time. In the quality control graphics, the measurements were mostly between the average $\pm$ 2 standard deviation.

The calibration curve for Li was built with pellets of Li_2CO_3, showing a very good proximity between the experimental data and the linear regression. A correlation coefficient of 0.984 for 610.37 nm line and 0.989 for 812.62 nm line was found. With this, it was possible to determine the limit of detection for Li, being 6 ppm for 610.37 nm line and 65 ppm for 812.62 nm line, using a Q-Switch Delay of 370 μs. The limit of quantification was 21 ppm and 215 ppm, respectively.

Regarding the precision of the system, the inter-day and intra-day values accentuate once again the fluctuations in the system, showing %RSD between 7.83% and 10.85% for intra-day and 15.37% and 23.59% for inter-day. Focusing on the results, it can be concluded that the system precision is within the order of %20.

Chapter 4

Spectrum Analysis

In this chapter, it will be discussed the different aspects inherent of spectrum analysis. The identification of the characteristic element lines depends on the existence of a chemical database that can be used as a reference for the experimental spectral lines. After that, they can be classified between atmospheric lines, i.e., those that are frequently found in the spectra due to the measurement environment, air, and those from intrinsic elements of the sample. Before developing a tool to automatize the procedure, the baseline must be removed in order to correct the spectral intensities. Finally, there will be a discussion regarding both element identification and the results obtained by the `Python` routine.

4.1 LIBS Databases

The main goal of LIBS is to discover which chemical elements are present in each sample, through a spectral analysis. Each chemical element has a set of fixed wavelengths in which it emits, creating lines in the spectrum, and to properly characterize a sample all different elements must be identified. However, there may be an overlap of the emission wavelengths, between different elements.

In an attempt to find the database that's most suitable to be used as a reference for the experimental spectra, two databases were studied: the OSCAR (Optical Science Center for Applied Research at Delaware State University) database [66] and NIST (National Institute of Standards and Technology) database [67].

4.1.1 NIST and OSCAR Databases

In the NIST database, it is possible to choose the atmosphere in which the wavelengths are desired, with the choice being between vacuum and air. Following NIST recommendations, the vacuum wavelengths between 180 and 200 nm and air wavelengths between 200 and 920 nm were chosen, although our measurements are done in air.

An important aspect is that this database has no information regarding some more complex chemical elements, given in Table 4.1. Consequently, those are not accounted for in this study.

TABLE 4.1: Elements without spectral information according to NIST database [67].

Elements with no NIST data								
Rn	Uuo	Uus	Uuh	Uup	Uuq	Uut	Fm	Np
Se	Cn	Rg	Ds	Mt	Hs	Bh	Md	Pu
Sg	Db	Rf	Pm	Ac	Th	Pa	No	Am
Cm	Lr	At	Po	Bk	Cf	Es	—	—

In this way, 87 chemical elements can be detected, whilst the other 31 elements of the periodic table are inaccessible. Although, the majority of elements without information are radioactive natural elements, synthetic radioactive elements or rare natural elements, that will not be used in these studies.

Regarding to OSCAR database, the spectra were acquired using a Helium atmosphere, with exception for Ar and N elements, for which another atmosphere was adopted. This atmosphere change results in lines with different intensities, when comparing against the data from the NIST database. It has spectral information for only 37 elements of the periodic table, indicated in Figure 4.1 with a blue, green and yellow border.

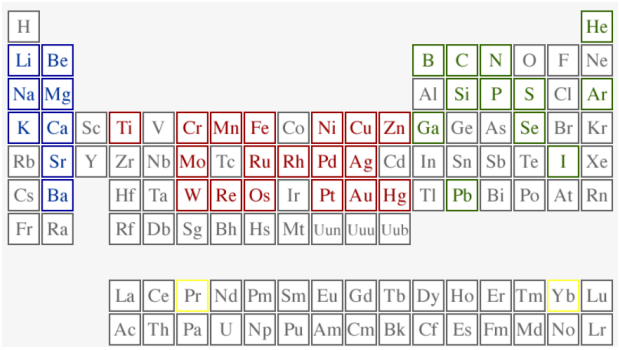

FIGURE 4.1: Elements with spectral information in OSCAR database (adapted from OSCAR LIBS database [66]).

As the OSCAR information is in a spectrum form, and not in discrete elemental characteristic wavelengths, some spectral treatment needs to be made such as the baseline removal, to obtain the correct intensities. It is important to refer that, as OSCAR does not have information about the statistical weights, the transition probabilities and the levels energy, it was not possible to calculate the Boltzmann Intensity associated with each line.

Thus, the NIST database proved to be the most complete one, so it will be used as a reference and OSCAR will only be used to clarify doubts.

4.1.1.1 Correlations between NIST and OSCAR databases

To conclude the study about the most widely used databases, it was relevant to analyze the presence of correlations between them. With both databases ready to be worked, there was a search for similarities between them. For it, a `Python` script was made, in order to search the line matches for each common element lines. The study was made for all element lines in NIST and OSCAR databases. The results showed that 22 of the 37 elements that are part of OSCAR had lines in common. However, there was a low amount of matches, with the exception of Fe, as can be seen in Table 4.2

TABLE 4.2: Elements with common lines between NIST and OSCAR Databases.

Element	N° of common lines	Element	N° of common lines	Element	N° of common lines
Ag	1	Fe	79	Pt	3
B	1	Ga	1	Rh	2
Ba	2	Mg	3	S	8
C	5	Mn	8	Si	1
Ca	6	Mo	16	Ti	15
Cr	5	Ni	3	W	14
Cu	4	Pr	4	Yb	1

Table 4.2 shows that the use of this information, with the goal of a future study about the elements present in the LIBS experimental spectrum, will not be a valid option to follow, because there is a very large loss of elements data.

4.1.2 NIST Exclusive Lines

Element exclusive lines are lines that emitted in specific wavelengths, that do not overlap with the ones from other elements (considering the resolution limitations). Those are characteristic of the given element and, to study them, a `Python` routine was developed.

Alongside the search for wavelength matches, i.e., lines that appear in more than one element, those that fall within a tolerance of 0.03 nm from each peak are also discarded. This tolerance was chosen as half of the resolution of the best channels (3 and 4) (see Subsection 3.1.1), in a rounded-up value.

With this process, only ten elements with NIST data, present no exclusive lines, as shown in Table 4.3.

TABLE 4.3: Elements without exclusive lines according to the `Python script` results.

Elements without exclusive lines				
Os	Ru	Sb	Tb	Te
Tl	Yb	As	Hf	I

As some of these elements have a high relevance, mainly in the soil sample studies due to their higher toxicity, relaxation of the restrictions placed on detection can be made, in order to discover their exclusive lines.

To finish the study, for each element exclusive line, the Boltzmann intensity was calculated. A higher Boltzmann Intensity indicates an increased probability that a given line will be detected by the spectrometer. Each line has different transition probabilities (A_{ki}) and Boltzmann Intensities (I_λ). Because NIST database only provides an Relative Intensity, the Boltzmann Intensity associated with all exclusive lines was calculated, using Equation 4.1,

$$I_\lambda = g_k \cdot A_{ki} \cdot e^{-\frac{E_k}{k_B}} \tag{4.1}$$

were I_λ represents the emission intensity for a given wavelength (λ), g_k the statistical weight for upper energy level (k), A_{ki} the transition probability, E_k the energy of the upper level and k_B the Boltzmann constant. The g_k, A_{ki} and E_k values were all discriminated in NIST data.

The results of this study will have a great importance for the search elements routine implementation, as will be mentioned later.

4.1.2.1 Organizing and exporting the exclusive lines data

To better visualize the results obtained by the script, a txt file named `NIST_exclusive_lines_organized.txt` was created, where all results are saved. The exclusive lines are sorted by the Boltzmann Intensities of each element, with the highest at the top of the file,

ensuring that the lines most likely to be detected are placed first in each of the elements. It is also possible to find information regarding the respective transition probability (A_{ki}) and relative intensity (I_r).

4.2 Atmosphere Elements

In a LIBS system, when no vacuum is used in the chamber, the probability of atmosphere lines appearing in the sample spectrum is very high. In the LIBS system used, the atmosphere is the terrestrial atmosphere, composed by Nitrogen (N), Oxygen (O), Argon (Ar) and Carbon Dioxide (CO_2) according to the information contained in [68]. The proportions are indicated in Figure 4.2.

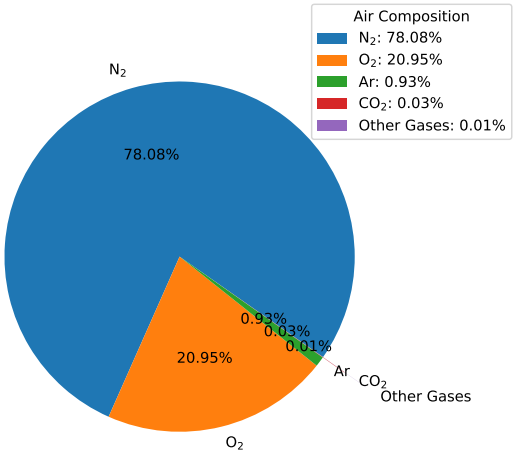

FIGURE 4.2: Atmosphere composition and respective percentages according to [68].

Thus, it is extremely important to know which lines of the experimental spectrum correspond to atmosphere elements, allowing to avoid wrong associations with other elements.

4.2.1 Identification of atmosphere lines

The first step was to obtain an air plasma spectrum. To do so, the laser was shot having no sample on its focal point. Using a Q-switch of 240 μs, corresponding to 143.2 mJ, plasma in air occurred systematically. An example of air plasma spectrum can be seen in Figure 4.3.

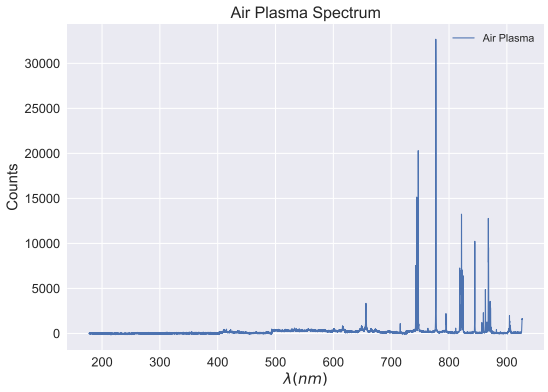

FIGURE 4.3: Air Plasma spectrum obtained for Q-Switch delay of 240 μs.

Because the variations are very wide from spectrum to spectrum, some pure targets of metallic elements were used to obtain information that contained only lines of the elements in question and the lines of the atmosphere. The targets chosen were: Fe 99.95% of purity (I4-9000-D29), Ti 99.995% of purity (T8-9000-D22), Cr 99.95% of purity (C6-9000-D146), and Si 99.999% of purity (S4-9000-D50)*. For the first two samples, a 340 μs Q-Switch delay was used and for the last two samples, a 310 μs, to guarantee that all spectra were not saturated.

Using that information, a `Python` script was made in order to find common lines to all of these four spectra.

This script obeyed to the following steps:

1. Baseline removal: the baseline of each spectrum was removed using Asymmetric Least Squares Smoothing (Subsections 4.3.1.2 and 4.3.2);

2. Search for peaks in spectrum: all peaks corresponding to spectral lines were determined using the `find_peak` † function from `scipy`;

3. Threshold definition: all lines with counts less than 600 were discarded (approximately three times the noise level);

4. Looking for common lines based on:

   - The four line wavelengths are equal;
   - Three of the four line wavelengths are equal and the other one are in 0.12 nm after or before the line wavelength;

*More information in http://www.testbourne.com/pure-metal-targets
†https://docs.scipy.org/doc/scipy/reference/generated/scipy.signal.find_peaks.html

- The four line wavelengths are equal two by two and the difference between them was less than 0.12 nm.

Once the common lines were identified, the NIST database [67] was used to discover their respective elements, assuming a tolerance of 0.12 nm to account for the resolution of the 8^{th} channel (channel with the larger number of atmosphere lines).

Some results can be seen in the Table 4.4 where all matches NIST line - Experimental Line are indicated.

TABLE 4.4: All matches between experimental and NIST lines.

Element	Exp. WL	NIST WL	Element	Exp. WL	NIST WL
N	422.72	422.77	O	251.58	251.72
	742.34	742.36		280.24	280.31
	744.20	744.23		777.12	777.19
	746.75	746.83		777.34	777.42
	818.46	818.49		822.25	822.18
	818.77	818.8		844.58	844.62
	821.53	821.63		926.17	926.08
	822.25	822.31		926.32	926.27
	824.18	824.24	Ar	285.18	285.19
	859.30	859.40		393.31	393.25
	862.85	862.92		396.8	396.84
	867.94	868.03		413.11	413.17
	868.21	868.34		422.72	422.7
	870.23	870.32	C	656.91	656.87
	871.05	871.17		766.40	766.24
	871.77	871.88	Na	588.87	589.0
Na	288.13	288.11		589.47	589.59

This investigation revealed the existence of experimental lines for all air elements, with Nitrogen (N) being the dominant one. The Sodium (Na) contamination lines were, once again, very present in the spectrum, with counts near the saturation value.

4.3 Baseline Correction

Whenever a LIBS measurement is performed, the captured spectrum (y) is composed by three components (Equation 4.2): the isolated emission lines, commonly called signal (S), the plasma continuum background (B), and instrumental noise (D), e.g. stray light and dark current [69]. Thus, the baseline is given by the sum of the contribution from B and D.

$$y = S + B + D \tag{4.2}$$

When comparing the weights of components B and D, the latter contribution is easily neglected. Plasma continuum background occurs due to the occurrence of two types of phenomena in the plasma: Bremsstrahlung radiation and recombination radiation [70], as discussed in Subsection 2.2.2. These phenomena add a randomly linear, or nonlinear, contribution that can decrease or increase the intensity, as a cause of different effects [71]:

- Samples characteristics, such as surfaces, matrices and emission lines;
- Plasma formation conditions;
- Fluctuations in the laser power.

As it is impossible to find the ideal situation in which this type of components results in a null (zero) contribution, it is important to make a baseline correction, so that the spectrum remains only with the information related to the emission lines.

4.3.1 Methods of Baseline Removal

According to the literature, some methodologies used for baseline simulation are: Asymmetric Least Squares Smoothing [72, 73], Median Filter [74] and Rolling Ball [75]. All of them were tested and the one with the best performance was selected. In the following subsections the different approaches will be discussed.

4.3.1.1 Median Filter or Model-Free Algorithm

The Median Filter method or Model-Free algorithm was introduced by Friedrichs in 1995 [74]. It consists on the determination of the median value of the extrema points in the spectrum (maximum and minima) within a delimited region, henceforth window. This window is centered in each point of the spectrum and slide over it, until the entire wavelength range is covered. The only parameter to be chosen is the width of the window, W, that should ensure that the number of points of the noise must be higher than the number of peaks. After that, Gaussian weights are used to smoothen the results [76][74]. The algorithm is described by the equation 4.3.

$$B(i) = \sum_{j=i-(W/2)+1}^{i+(W/2)} M(j)G(i-j) \tag{4.3}$$

$$\sum_{k=-(W/2)}^{(W/2)-1} G(k) = 1 \tag{4.4}$$

where M(j) is the median value of the window centered in point j and G(k) is the Gaussian weight of the medians in the same region, as given by equation 4.4. Figure 4.4 shows an illustration of a Median Filter simulation.

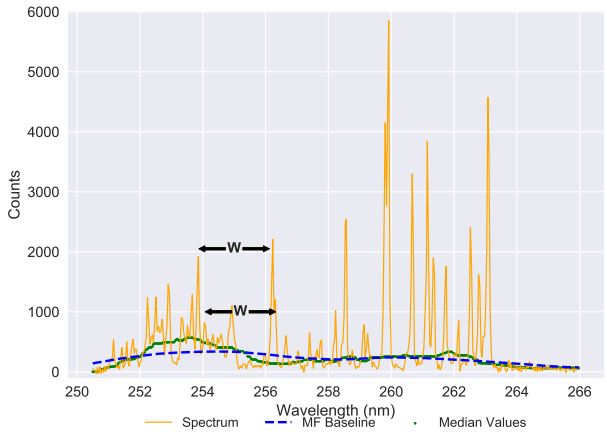

FIGURE 4.4: Example of Median Filter simulation. The spectrum is shown in orange, the median values in green and, in blue, the baseline resulting from the smoothing of the median values. The W letter exemplifies the window width sliding over the spectrum.

4.3.1.2 Asymmetric Least Squares Smoothing

The Asymmetric Least Squares Smoothing is a method of baseline simulation reported by Eilers and Boelens [72, 73] and later by Liland et al [76] that can be represented by the algorithm in equation 4.5

$$S = \sum_i w_i (y_i - z_i)^2 + \lambda \sum_i (\Delta^2 z_i) \tag{4.5}$$

where y are the spectral values, z is the first baseline estimation that needs to be smooth but representative to y too, in order to minimize the penalized least squares function, shown in equation 4.6.

$$S = \sum_i (y_i - z_i)^2 + \lambda \sum_i (\Delta^2 z_i) \tag{4.6}$$

Finally $\Delta^2 z_i = (z_i - z_{i-1}) - (z_{i-1} - z_{i-2}) = z_i - 2z_{i-1} + z_{i-2}$, λ is responsible for the balance between the first and the second term of the equation 4.5 and w_i is a vector of weights that is used to minimizes the function. This vector is $w_i = p$ if $y_i > z_i$ and

$w_i = 1 - p$ if $y_i < z_i$, where p is an introduced parameter in order to attribute a larger weight to negative residuals $(y - z)$ and can have values between 0 and 1. To obtain the ideal baseline is necessary to find the best values for these parameters, w and p [72].

4.3.1.3 Rolling Ball

The Rolling Ball method consists in a simulation of a ball with large dimensions rolling under the spectrum. For each wavelength, the baseline is obtained through the top coordinate of the ball. This algorithm was referred by Kneen and Annegarn in 1996 [75]. The equations of this method are in the equations 4.7 and 4.8.

$$Y_i = f_G(i) = max\{f_{i-\nu}^{(1)}, ..., f_i^{(1)}, ..., f_{i+\nu}^{(1)}\} \tag{4.7}$$

and,

$$f_i^{(1)} = min\{f_{1-\nu}, ..., f_i, ..., f_{1+\nu}\} \tag{4.8}$$

where, $f_i^{(i)}$ is an expanding square wave filter.

First, the window dimension must be defined and, afterwards, three steps are sufficient to determine the baseline values. The first step allows for the determination of the minimum points within the window. The second one is a search for the maximum points between the points of local minima. The last step is an average over the points collected in the second step, resulting in the smoothing of the baseline curve [76].

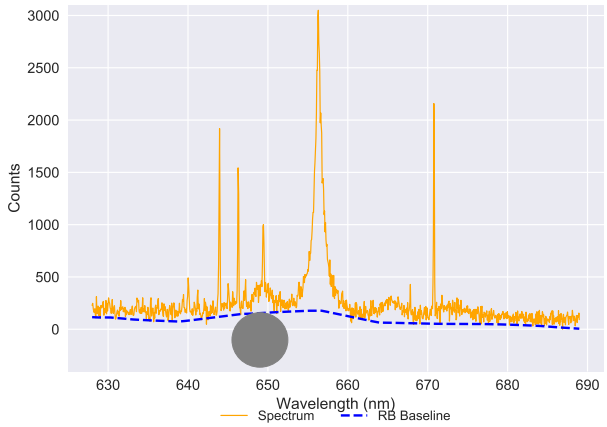

FIGURE 4.5: Example of Rolling Bal simulation. The spectrum is shown in orange and, in blue, the baseline resulting the under spectrum rolling ball (gray ball).

A visual representation of the algorithm is given in Figure 4.5.

4.3.2 Selection of the Best Method

Using `Python`, all of these methods mentioned in subsection 4.3.1 were applied to Fe spectra, with the goal of determining the optimal one for the LIBS. In all cases, the baseline-corrected spectrum was obtained by subtracting the simulated baseline from the original spectrum.

The first method to be tested was the Median Filter (MF), using the `medfilt`* function of `scipy`. In this case, the only one parameter to be chosen was the best window local size.

A large amount of values was tested (between 30 and 100 points), until the resulting baseline was not only sufficiently adjusted to the spectrum but also very smooth. This process resulted in the choice of a window width of W=50.

The median filter baseline simulation and the correction result can be seen in Figure 4.6.

FIGURE 4.6: Fe spectrum with: Left - simulated baseline using MF; Right - baseline removed using MF.

To see the baseline correction with high detail, consult Appendix D.1, Figure D.1.

Another method tested was the Asymmetric Least Squares Smoothing (ALSS). In this case more parameters need to be determined and the chosen values are given in Table 4.5.

TABLE 4.5: Optimal parameters for the Asymmetric Least Squares Smoothing Method.

Parameter	Function	Value
p	weigth of the residuals	10^{-3}
n	number of iteractions	10
λ	balance between equation terms	10^4

*https://docs.scipy.org/doc/scipy/reference/generated/scipy.signal.medfilt.html

The baseline simulation and the correction results for the Fe spectrum are shown in Figure 4.7.

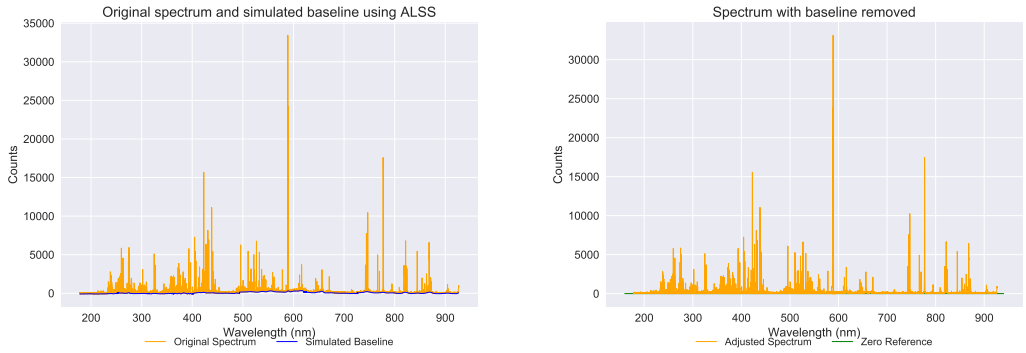

FIGURE 4.7: Fe spectrum with: Left - simulated baseline using ALSS; Right - baseline correction using ALSS.

To see the baseline correction with high detail, consult Appendix D.1, Figure D.2.

This algorithm needs an extra correction, since the noise level is not centered at zero, but slightly above. To correct this shift, three different methods were tested, which were named "mean shift", "bin shift" and "percentile shift". The one showing best result was the "percentile shift" method that will be described in more detail. It is determined using the 75^{th} percentile of the spectral intensities histogram. After that a Gaussian was fitted to it, as seen in seen in Figure 4.8. The removal of data was employed in guarantee that the fit was not affected by the outliers, i.e., by bins corresponding to spectrum lines, as it is expected that the majority of the data is at the baseline level. The shift value was determined as the central value of the fitted Gaussian. The result graphic can be seen in Figure 4.9 and the shift value estimated was 83.63.

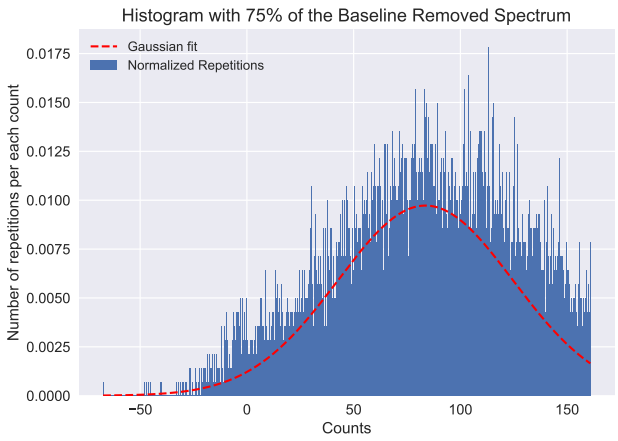

FIGURE 4.8: Percentile with 75% of the spectrum data.

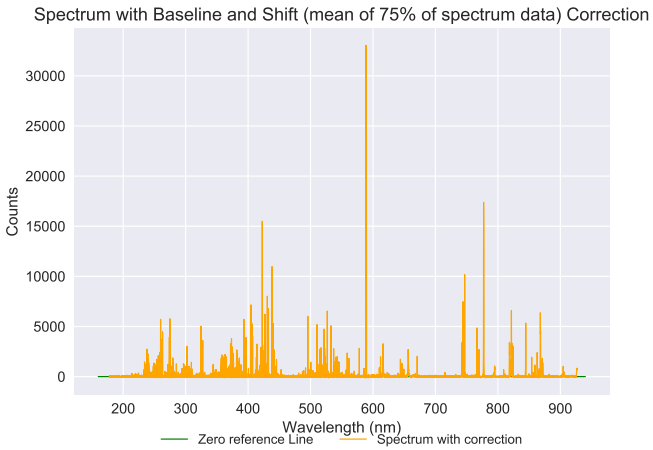

FIGURE 4.9: Result of Asymmetric Least Squares Smoothing baseline removal combined with percentile shift

At the end, the Rolling Ball (RB) algorithm was also tested. Once again, the local window size (W_l) needs to be estimated, as well as the size of the smoothing window (W_s). The values with best results were W_l=80 and W_s=70. The baseline estimated by the method can be seen in left side of Figure 4.10 and the baseline removal result in the right side.

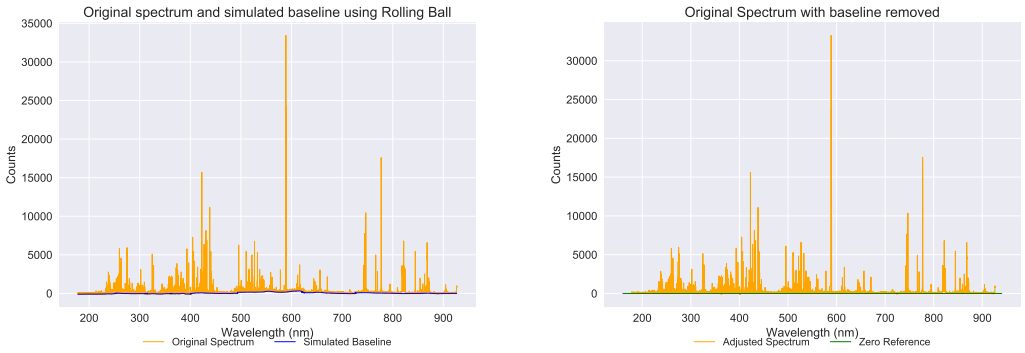

FIGURE 4.10: Fe spectrum with: Left - simulated baseline using RB; Right - baseline correction using RB.

To see the baseline correction with more detail, consult Appendix D.1, Figure D.3. This method also needs a shift correction similarly to ALSS.

To conclude which is the best baseline simulation method for LIBS spectra, a quantitative analysis was made. For this purpose, the outliers percentage was calculated, i.e., the spectrum points that are below the general noise level are counted and divided by the total number of points in the spectra. The outliers percentage, calculated for each method, are reported in Table 4.6.

TABLE 4.6: Outliers percentage obtained for each baseline method.

Method	Outliers (%)
MF	8.6
ALSS	2.1
RB	2.5

As can be seen, these results are in accordance with Figures 4.11, 4.12 and 4.13.

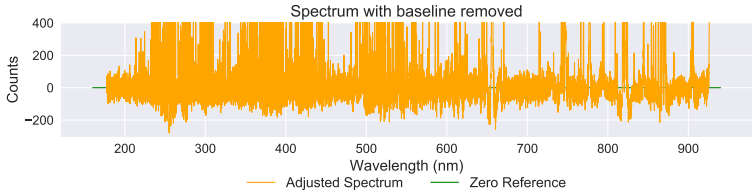

FIGURE 4.11: Zoom in results for Median Filter baseline correction.

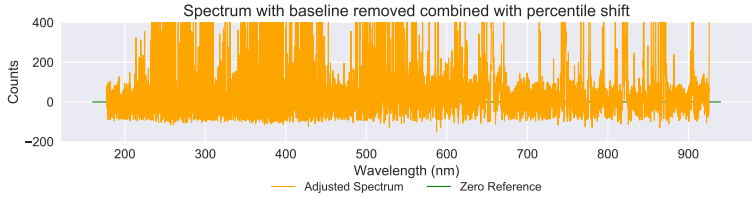

FIGURE 4.12: Zoom-in results for Asymmetric Least Squares Smoothing baseline correction combined with "percentile shift approach.

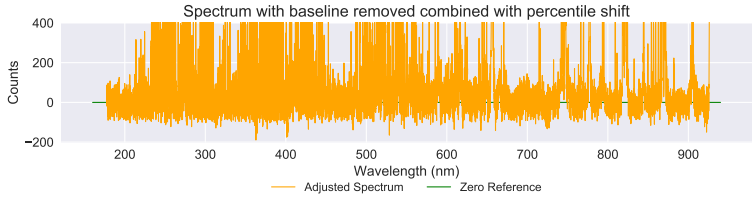

FIGURE 4.13: Zoom-in results for Rolling Ball baseline correction combined with "percentile shift approach.

The ALSS method shows the lowest percentage of outliers at the noise level, being selected as the best baseline simulation approach. The Rolling Ball was the closest to the result obtained by the ALSS and the Median Filter was the one with the worst result.

4.4 Search Elements Tool

After knowing the exclusive lines of each element, as well as the lines of the elements present in atmosphere and corrected the baseline of the spectrum, the next step is to discover the composition of a given sample through its LIBS spectrum. For this, it was necessary to create a tool that can search for each line in the experimental spectrum.

4.4.1 Routine Description

In the development of this routine, many cases had to be considered, and the process can be divided in different steps. A flowchart of the code can be found in Figure 4.14.

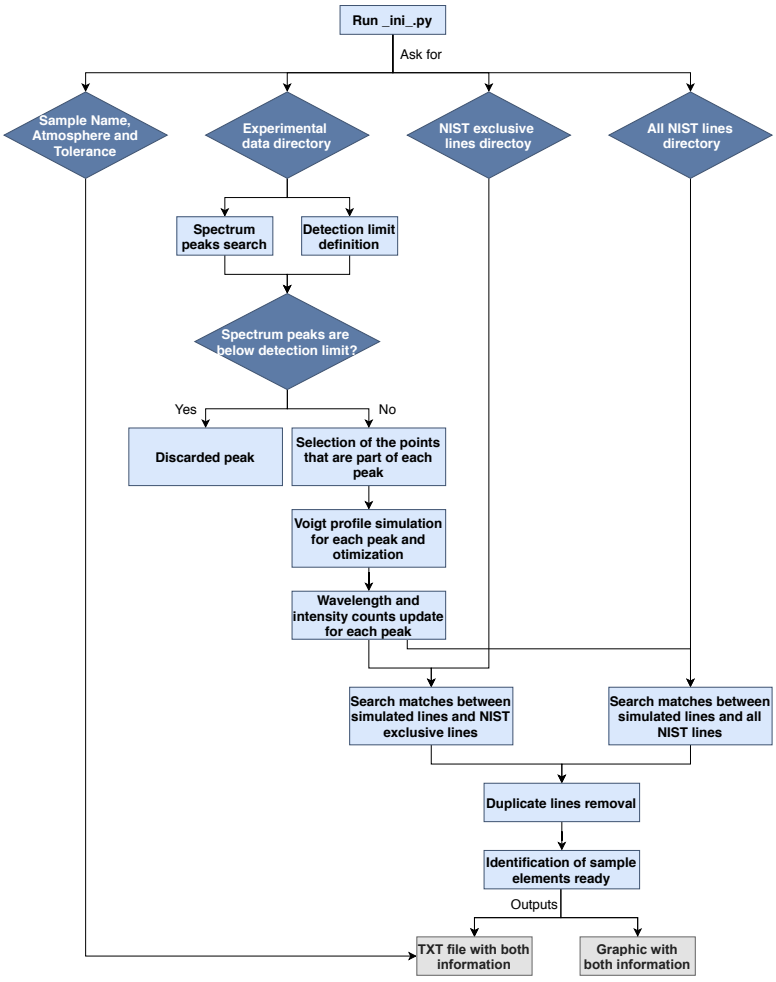

FIGURE 4.14: Flowchart of the search elements in experimental spectrum routine.

A detailed explanation of the different stages will be made in the following subsections.

4.4.1.1 Experimental Data and Limit of Detection

Before proceeding with the spectral analysis, it is essential to remove the baseline, to minimize the influences of electronic noise.

Using the data with the subtracted baseline, the `find_peaks`* function of `scipy` was used to detect the peaks in the spectrum.

In order to find the minimum concentration necessary to reliably test the presence of an element in a sample, the system's Limit of Detection, LOD, must be calculated using the Equation 3.3. As until now it was not possible to perform the tests for the calibration curve for all elements of the periodic table, the LOD was estimated to be about 3 times the noise level. All detected peaks below this value are discarded.

4.4.1.2 Peak Data Definition

For each peak detected, it was necessary to define the points of the experimental spectrum that compose it. An array was created for each peak, with 17 consecutive points, centered on the central wavelength (i.e., 8 to the left and 8 to the right of the peak). Afterwards, the local minima at left and right of the peak, were determined to set the boundaries of the spectral line. The previous array, until then composed by 17 points, is now transformed to only contain the points between the two local minima (i.e., the one from each side of the peak), as seen in Figure 4.15.

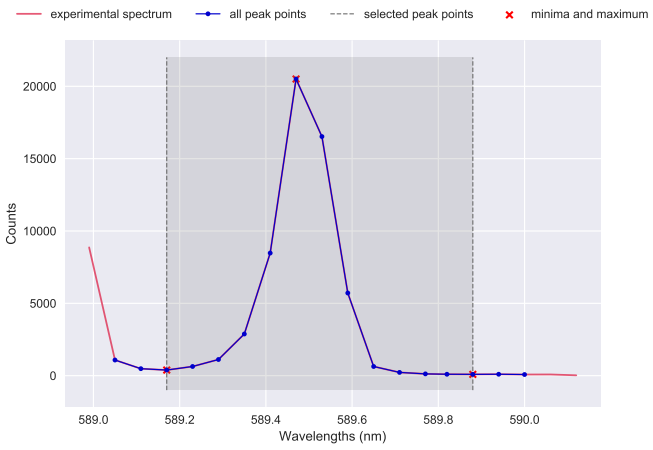

FIGURE 4.15: Explanation of the peak points selection criteria. In dark red the experimental spectrum is shown, in blue the 8 points on the left and on the right of the peak, in the red crosses the maximum and minimum points and in the shaded area, the selected peak points between the left and right minima.

*https://docs.scipy.org/doc/scipy/reference/generated/scipy.signal.find_peaks.html

4.4.1.3 Self Absorption Effect

Self-absorption phenomena, occurs when light emitted by an element on the center of the plasma is absorbed in another part of the plasma, closer to the periphery [77]. This happens mainly when there are elements with high concentrations, creating high intensity lines. A representative scheme can be seen in the Figure 4.16.

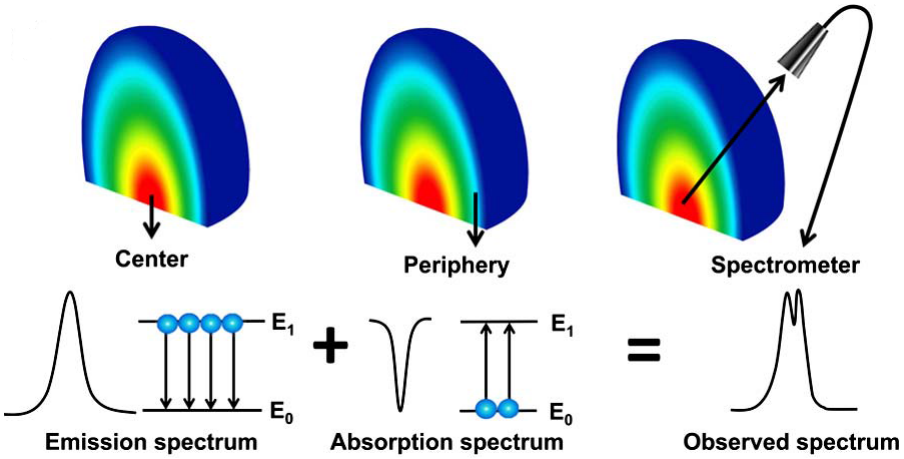

FIGURE 4.16: Self-absorption exemplified scheme (adapted from [77]).

At the spectrum level, this effect is characterized by the evidence of a flat-topped profile or even a dip centered on the peak wavelength, as can be seen in Figure 4.17.

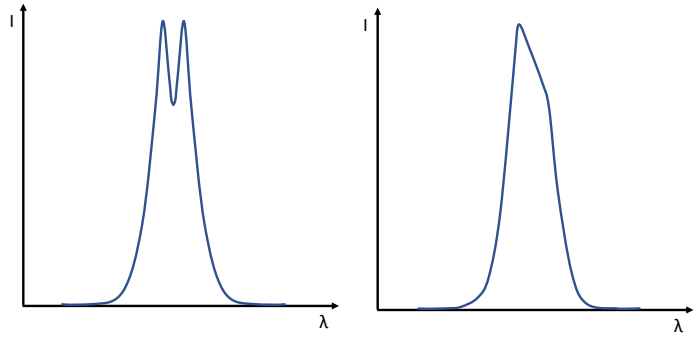

FIGURE 4.17: Self-absorption shapes. Left: dip profile, also called self-reversal; Right: flat-topped profile.

This effect can condition the routine described in the latter subsection because more than one peak can be detected by the `scipy` for the same theoretical line, resulting in multiple arrays. The solution to this problem is to compare the intensities of the central peaks of these arrays and chosen the one that presents the highest intensity. The other one is discarded.

4.4.1.4 Voigt Profile

In LIBS spectrum, the profile that most closely matches the shape of the lines is the Voigt profile [7]. This profile is a convolution between Gaussian [78] and Lorentzian [79] profiles, and the associated expressions are given in Equations 4.9 and 4.10, respectively,

$$G(x;\mu,\sigma) = \frac{1}{\sigma\sqrt{2\pi}} e^{-\left(\frac{x-\mu}{2\sigma}\right)^2} \tag{4.9}$$

$$L(x;\mu,\gamma) = \frac{1}{\pi\gamma}\left(\frac{\frac{1}{2}\gamma^2}{(x-\mu)^2 + \left(\frac{1}{2}\gamma\right)^2}\right) \tag{4.10}$$

where μ is the mean of Gaussian profile and the location peak of the Lorentzian profile, σ is the standard deviation, and γ is the full width at half maximum of the Lorentzian profile. The expression typically used to calculate the Voigt profile, is the following:

$$V(x;\mu,\sigma,\gamma) = \int_{-\infty}^{+\infty} G(x';\mu,\sigma)L(x-x';\mu,\gamma)dx' \tag{4.11}$$

that can be written using the Faddeeva function as indicated in the Equation 4.12,

$$V(x;\sigma,\gamma) = \frac{Re[\omega(z)]}{\sigma\sqrt{2\pi}} \tag{4.12}$$

where $\omega(z)$ is the Faddeeva function and $z = \frac{x+i\gamma}{\sqrt{2}\sigma}$ [80]. In Figure 4.18, the three profiles are compared, with a μ of 0.5 nm, a σ of 0.1 nm and a γ of 0.1 nm.

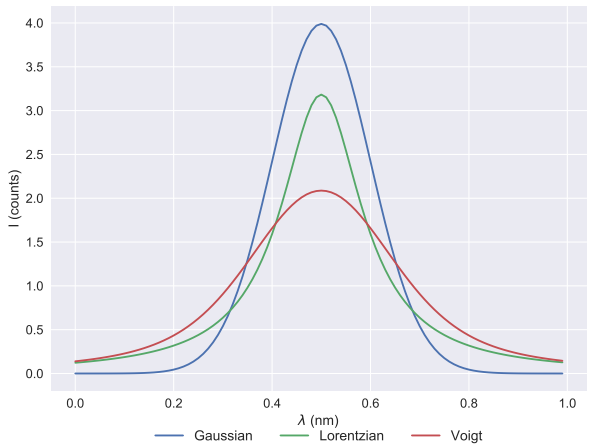

FIGURE 4.18: Simulation of the three different profiles, Gaussian (blue), Lorentzian (green) and Voigt (red) using μ=0.5 nm, σ=0.1 nm and γ=0.1 nm.

With Equation 4.12, a Voigt profile was simulated for each detected peak, using the experimental data that belongs to each individual line. As initial parameters, the values from Table 4.7 were used. An amplitude parameter (amp) has also been added, to control the height of the peak.

TABLE 4.7: Initial parameters used to Voigt profile simulation.

Parameter	Value
μ	Peak Wavelength (nm)
σ	0.075 nm
γ	0.03 nm
amp	Peak counts

The parameters were found by simulating Gaussians and Lorentzians and looking for values that originated similar profiles to those from experimental lines, in all the experimental range. Based on these values, an optimization was made using a `scipy` function called `curve_fit`*, resulting on the best fit for each line. To ensure that no unreasonable lines appear, i.e., an unusually high amplitude parameter, the uncertainty associated with this parameter was also calculated. To do so, the covariance matrix (`pcov`) provided by the `curve_fit` function was used. The values in the diagonal of the matrix correspond to the variance of each parameter of the fit and the square root of each of these values results in the uncertainty. All simulations that present an uncertainty, associated to the *amp* parameter, larger than 10000 counts, were automatically discarded, because they originated situations of non-convergence. In those situations, the experimental values are used. The results, of a Voigt simulation, for a complete Petalite spectrum can be found in Figure 4.19.

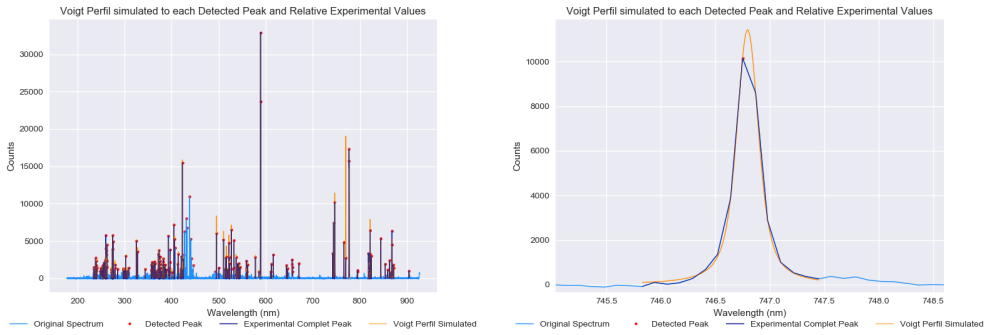

FIGURE 4.19: Voigt profile simulation for: Left - a complete Petalite spectrum; Right - a specific peak. The blue line is the original spectrum, the red points are the detected peaks, the dark blue line the experimental values used for each peak simulation and the orange line is the simulated profile.

*https://docs.scipy.org/doc/scipy/reference/generated/scipy.optimize.curve_fit.html

On the right side of Figure 4.19, a Voigt profile simulation for a single line is given, showing the experimental peak, coupled with a good correction by the simulated Voigt profile.

This simulation allows the correction of the peak wavelength of each line, given by the value of μ and a new estimation of the line counts, obtained by calculating the maximum point of the Voigt profile.

4.4.2 Elements Search

After defining the line data and profile, the line search can now be implemented using the entire NIST database and the NIST exclusive lines (previouly ordered by Boltzmann Intensities). For both cases, the first twenty lines of each element were used, ensuring that only lines with high probability of detection are included.

The choice of the criteria for the line's search, proved to be a complex task, due to the experimental lines being misaligned with the theoretical ones (NIST database). The most probable cause was the spectrometer resolution and calibration. Due to its finite resolution, two lines of different wavelengths, if too close, may fall within the same pixel, forming a singular peak.

Therefore, different strategies were implemented in order to obtain the greater number of elements expected to be present in the samples under study and maximize the matches between NIST and experimental lines of these elements.

Different methods were tested taking into account the channel CCDs resolution, mentioned in subsection 3.1.1. In all the methods a presence of at least 3 lines in common was needed to validate the presence of a chemical element. A description of each method is given in the following points:

1. For each line, exclusive and nonexclusive, the tolerance value was the resolution value common to a greater number of channels, that is 0.03 nm (Figure 3.2);

2. The total mean resolution across all channels was calculated, 0.05 nm, and set as the tolerance for this method;

3. The tolerance value referred in the first method was changed to the lowest resolution value for each channel, according to the Table 4.8.

TABLE 4.8: Applied tolerance for each spectrometer channel using the respective worst resolution value.

Channel	1	2	3	4	5	6	7	8
Tolerance (nm)	0.05	0.04	0.04	0.03	0.06	0.08	0.07	0.12

4. The tolerance values chosen were the mean resolution value for each channel, as shown in Table 4.9.

TABLE 4.9: Applied tolerance for each spectrometer channel using the respective mean resolution value.

Channel	1	2	3	4	5	6	7	8
Tolerance (nm)	0.04	0.03	0.03	0.02	0.05	0.06	0.05	0.10

5. For each spectral line, the resolution value in its point was added to the peak wavelength and, from the value of the sum, a tolerance of 0.03 nm was applied. This was made because the Voigt profile simulation and theoretical line (NIST) showed, in a large number of cases, differences very close to the resolution values. As an example, the Li NIST line is present at a wavelength of 812.62 nm, and the Voigt simulation showing it to be at a wavelength of 812.51 nm, representing a 0.11 nm shift. Figure 3.2 shows that the resolution fluctuates, for the most part, between 0.09 and 0.11 nm in this channel, being coincident to the shift.

6. The last one, was similar to the fifth, albeit with a larger tolerance, of 0.05 nm.

All these methods were tested for a group of samples that contained pure targets and mineral samples. The results are in the Tables 4.10 and 4.11.

TABLE 4.10: Table with the test results for all methods in pure samples. The check marks indicate that the element was found by the method and the x that was not found.

Sample	Method					
	1	2	3	4	5	6
Ar	x	x	✓	✓	✓	✓
Cr	✓	✓	✓	✓	✓	✓
Cu	✓	✓	✓	✓	✓	✓
Fe	✓	✓	✓	✓	✓	✓
Kr	x	x	✓	✓	✓	✓
Ne	✓	✓	✓	✓	✓	✓
Si	✓	✓	✓	✓	✓	✓
Ti	✓	✓	✓	✓	✓	✓

TABLE 4.11: Table with the test results for all methods in mineral samples. The check marks indicate that the element was found by the method and the x that was not found.

Sample	Method					
	1	2	3	4	5	6
Turquoise (Al, Cu, P, H, O)	x	x	O	O	Al, Cu, P	Al, Cu, P
Montebrasite (Al, Li, P, H, O)	x	x	Li	Li	Li	Al, Li
Spodumene (Al, Li, Si, O)	Si	Si	Li, Si, O	Li, Si, O	Li, Si, O	Al, Li, Si, O
Petalite (Al, Li, Si, O)	Si	Si	Li, Si, O	Li, Si, O	Li, Si, O	Al, Li, Si, O
Pollucite (Al, Cs, Na, H, O, Rb, Si)	Si	Al, Si, O	Na, O, Rb, Cs, Al	O, Al, Si	Na, O, Al, Si	Al, Na, O, Rb Si

Tables 4.10 and 4.11 allow for the conclusion that the worst methods were the 1^{st} and 2^{nd}, detecting only 75% of the pure elements, and 13% and 20% of the composition of two out of five minerals. The methods 3 to 6 show the same results for pure samples, successfully identifying all the elements. Looking at the mineral samples for methods 3^{rd} and 4^{th}, 57% and 49% of the sample's composition was found. For the 5^{th} and 6^{th} method, 59% and 85% of the sample composition was successfully identified, respectively. For this test, the H is discarded because the routine used was drawn to validate elements with three or more visible lines. As H presented only one detectable line, it was never validated. As the best method proved to be the 6^{th}, it will be the one used in studies of the sample's composition.

4.4.3 Mineral and Pure Samples Composition Database

Using the information in the Mineralogy Database [55], a Mineral and Pure Samples Composition Database was created, with some of the minerals that are most commonly used in the laboratory. In that database, for each of these minerals a txt file was created (with the name of the mineral) where its composition can be found, indicating the chemical elements and the respective percentages. The same was done for each of the chemical elements of NIST, so that it can also be used in pure samples.

4.4.4 Graphic Interface

To allow this routine to be used in a more versatile and interactive way, from the user's perspective, an interface window was created, as can be seen in Figure 4.20.

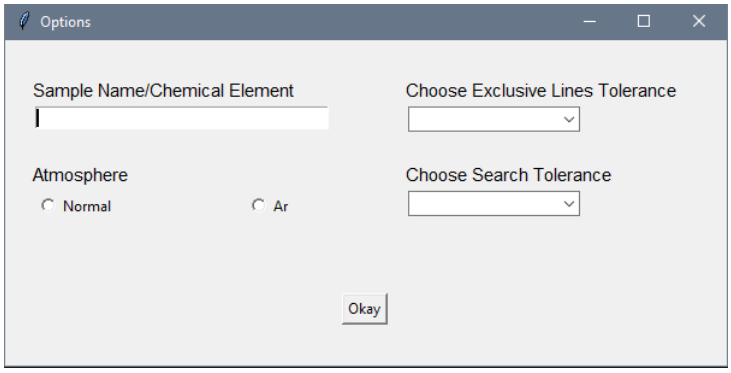

FIGURE 4.20: Search Elements Routine Interface

Through it, it is possible to input the sample name or, in the case of pure samples, a chemical element symbol must be given. This will be used later, as the name of the txt where the data is stored. In addition, it is possible to choose the tolerance value used in the NIST exclusive lines database, with options ranging from 0.00 nm to 0.08 nm, in steps of 0.01 nm. The recommended value is 0.03 nm and was indicated as default. Finally, the tolerance to apply between all and exclusive NIST lines and the experimental ones can be selected to. Once again, the recommended value, justified in the subsection 4.4.2, is marked as default.

4.4.5 Output information

At the end of the search process, a chart is generated with all the collected information, as indicated in Figure 4.21. Additional information is processed using the database introduced in Section 4.4.3 and the atmosphere composition chosen in the interface, Normal (N, O, C) or Argon (Ar). Combining all this information the elements found were grouped into:

- sample composition elements (Expected Found Elements);
- sample composition elements that were not found (Expected but Not Found);
- atmosphere elements (Atmosphere Elements);
- none of the above groups (Not Expected Elements).

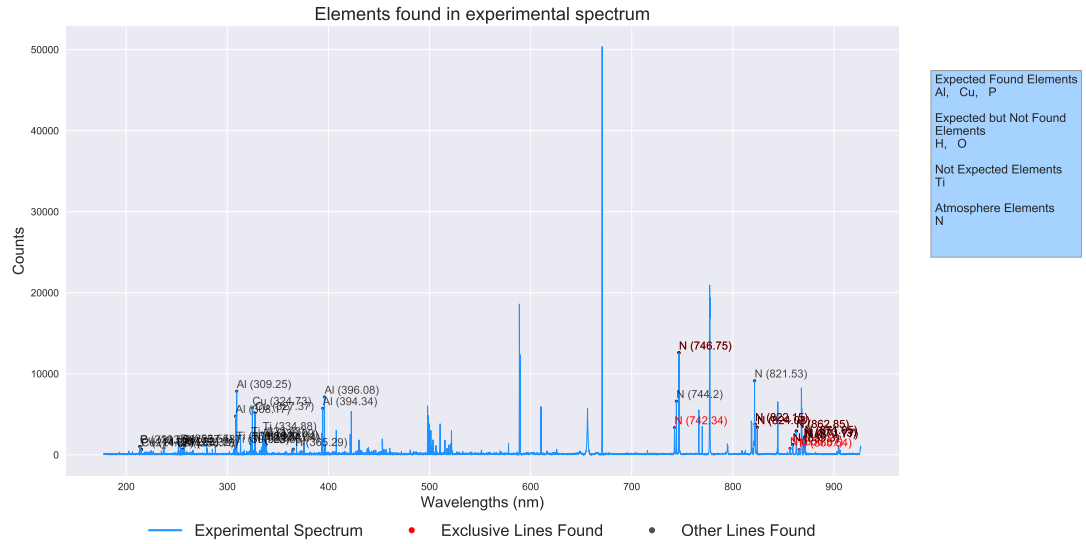

FIGURE 4.21: Graphic with all lines found for a Turquoise spectrum. In blue the original spectrum, in red the exclusive lines found, and in grey the nonexclusive lines.

In Figure 4.21 all the experimental spectrum is represented, with the detected exclusive lines marked in red, alongside their element name and wavelength value. The same information is also shown for non-exclusive wavelengths. All these results can be exported in a txt file.

4.5 Analysis Overview

With the results obtained by Element Exclusive Line routine, the exclusive wavelengths of 77 elements of the periodic table were found, belonging to NIST database, with a guaranteed separation of 0.03 nm between them. The Boltzmann intensities for each exclusive line were also determined, which were used to sort the results in descending order.

The OSCAR LIBS database proved to be more incomplete, regarding the range of elements with spectral information, as it only presented 37 elements. On the other hand, the NIST database compiled information from 77 elements, which represents twice as many elements.

The study of the common lines to NIST and OSCAR showed how different the information contained in these databases is. A very small number of common lines was

found for 22 elements, leaving 15 elements present in the two databases without any line in common.

The analysis of the atmosphere elements allowed for the characterization of the experimental lines associated with the different elements that comprise the atmosphere. Thus, allowing for the search of other elements in the spectrum, taking in account that these lines should be considered as atmosphere lines.

The study of the baseline simulation methods allows for the conclusion that the best algorithm for LIBS spectra is Asymmetric Least Squares Smoothing, as it presented a smaller dispersion in the noise level and a higher proximity with the shape of the spectra.

Regarding the Element Search Tool, the routine appears to be a good starting to the development of a robust element search tool. However, there is still a need to fine-tune some parameters that can only be set after widening the range of test samples. One of the important points to bear in mind is the tolerance that is being given in the search for matches and the minimum number of lines to affirm the presence of the chemical element in the sample.

Chapter 5

Case Studies

5.1 Hydrothermal Vein Sample

The Turquoise mineral is formed by the alteration of Montebrasite as explained in Figure 5.1. This process is problematic to the mining industry because it rises difficulties in the separation between Montebrasite and Turquoise, originating a decrease in the Lithium concentration in the final product. In the future the LIBS technique can be one option for the mining companies due to it allows a rapid detection of Li in minerals.

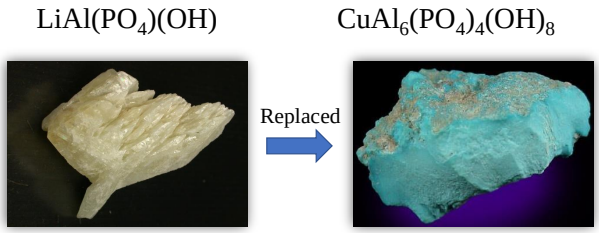

FIGURE 5.1: Turquoise formation process. Left - Montebrasite Mineral. Image from [81]. Right - Turquoise Mineral. Image from [82].

In order to measure if Turquoise still has significant Li infiltrations in its chemical composition, a hydrothermal vein sample from Argemela, a district in Portugal shown in Figure 5.2, was studied.

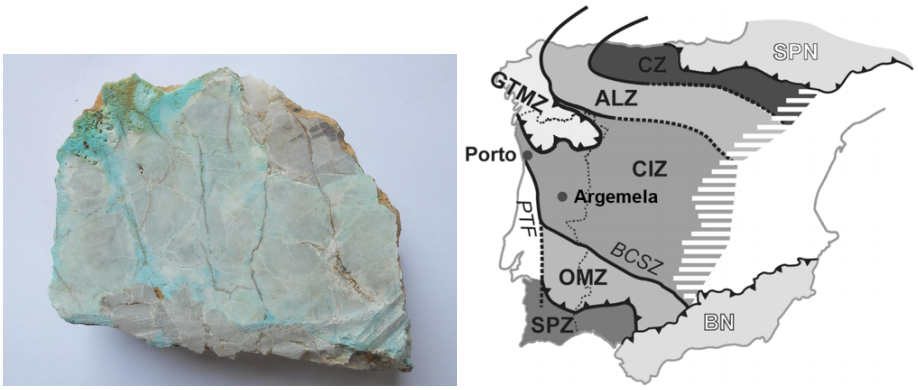

FIGURE 5.2: Left - Hydrothermal vein Sample. Right - Argemela location on the Iberian Peninsula. Figure adapted from [83].

Argemela is part of the southern Central Iberian Zone (CIZ) and can be divided in two main areas: Argemela Tin Mine and Argemela Hill Top. The hydrothermal vein was collected in the Argemela Tin Mine and is part of a swarm of sub-vertical veins that are mostly composed by Montebrasite, Quartz and Turquoise [84].

TABLE 5.1: Concentrations of the chemical elements in Turquoise, Montebrasite and Quartz. According to [55].

Chemical Element	Concentrations (%)		
	Montebrasite	Turquoise	Quartz
Lithium (Li)	4.74	0	0
Cooper (Cu)	0	7.81	0
Phosphorous (P)	21.16	15.23	0
Aluminium (Al)	18.43	19.90	0
Silicon (Si)	0	0	46.74

The elemental concentrations of each mineral under study, and that will be relevant to the analysis, can be consulted in Table 5.1.

5.1.1 Experimental Procedure

To perform the study, the hydrothermal vein sample was cut in half, ensuring that the surface was flat. No further sample preparation was required. After this, a specific area of the sample containing the 3 different minerals were selected for mapping.

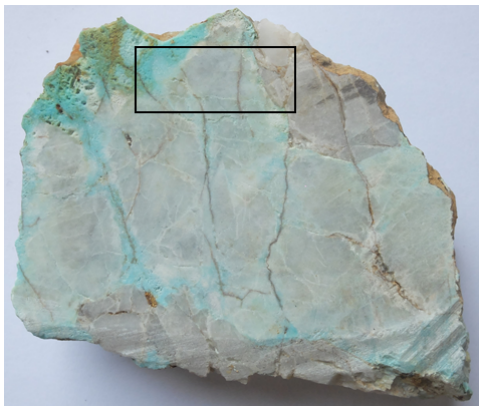

FIGURE 5.3: Map selected area composed by Montebrasite, Turquoise and Quartz.

5.1.1.1 Energy Study

An energy study was made using the Li exclusive line 812.62 nm. This line was selected because the purpose of this analysis is to detect Li in the sample and not quantify it. For that, it is best to use an exclusive line even if with lower intensity. Next, it is important to choose an energy that does not saturate the line of interest.

The Montebrasite area - the mineral containing Li in the highest concentration - was analyzed using several energies, to find both the minimum energy necessary to detect Li and the energy that would saturate the 812.62 nm line. Energies ranging from 6.9 to 143.2 mJ were used, and it was noted that an energy of 6.9 mJ (Q-Switch delay of 400 μs) is enough to detect the existence of the desired line. Furthermore, above 121.9 mJ (Q-Switch delay of 260 μs), the line is saturated.

The same study was made in Turquoise region to assure that the energy used was not too low, not revealing the line of Li if present in the sample in a low concentration. Starting from the previously found minimal Q-Switch delay, energy of 6.9 mJ, Q-Switch delays up to 260 μs with intervals of 10μs, were tested.

Only after energies of 21 mJ (Q-Switch delay of 380 μs) the signal is above the detection limit, but still very low. To have the best sensitivity to the Li line, the highest energy was chosen that does not saturate Li line in montebrasite area, 121.9 mJ corresponding to a Q-Switch delay of 260 μs).

5.1.1.2 Mapping Analysis

A LIBS mapping of the rectangular zone marked in Figure 5.3 was made. The LIBS protocol is outlined in Figure 5.4.

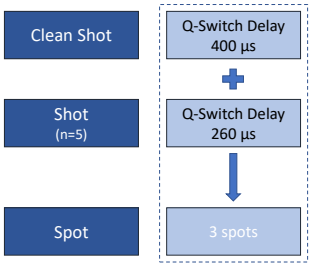

FIGURE 5.4: LIBS protocol.

For this, a 26 × 11 points grid was performed, with a step of 1 mm between spots, taking into account the laser spot size (around 300 μm) and the level of detail needed for this analysis. The mapping area was composed by Turquoise, Montebrasite and Quartz and can be seen in Figure 5.5.

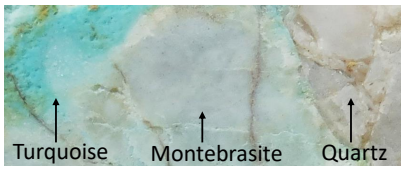

FIGURE 5.5: Distribution of the minerals into the mapping area.

The mapping results obtained for each element, can be seen in Figures 5.6 and 5.7.

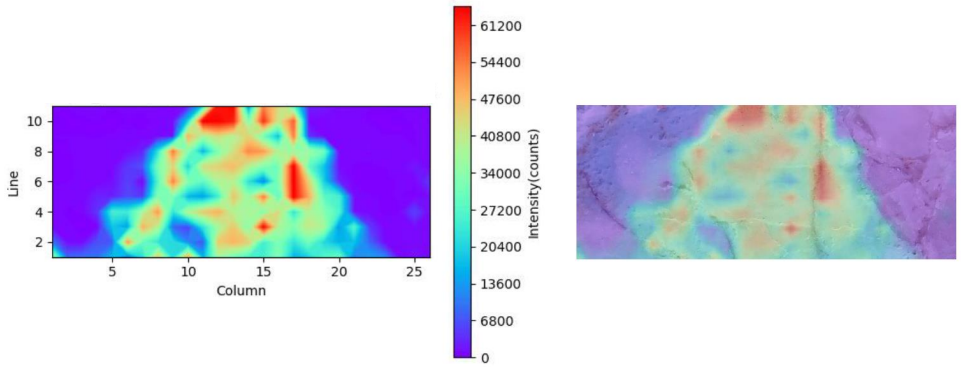

FIGURE 5.6: Map results (left) and map overlaid on the sample (right) for Lithium (812.62 nm).

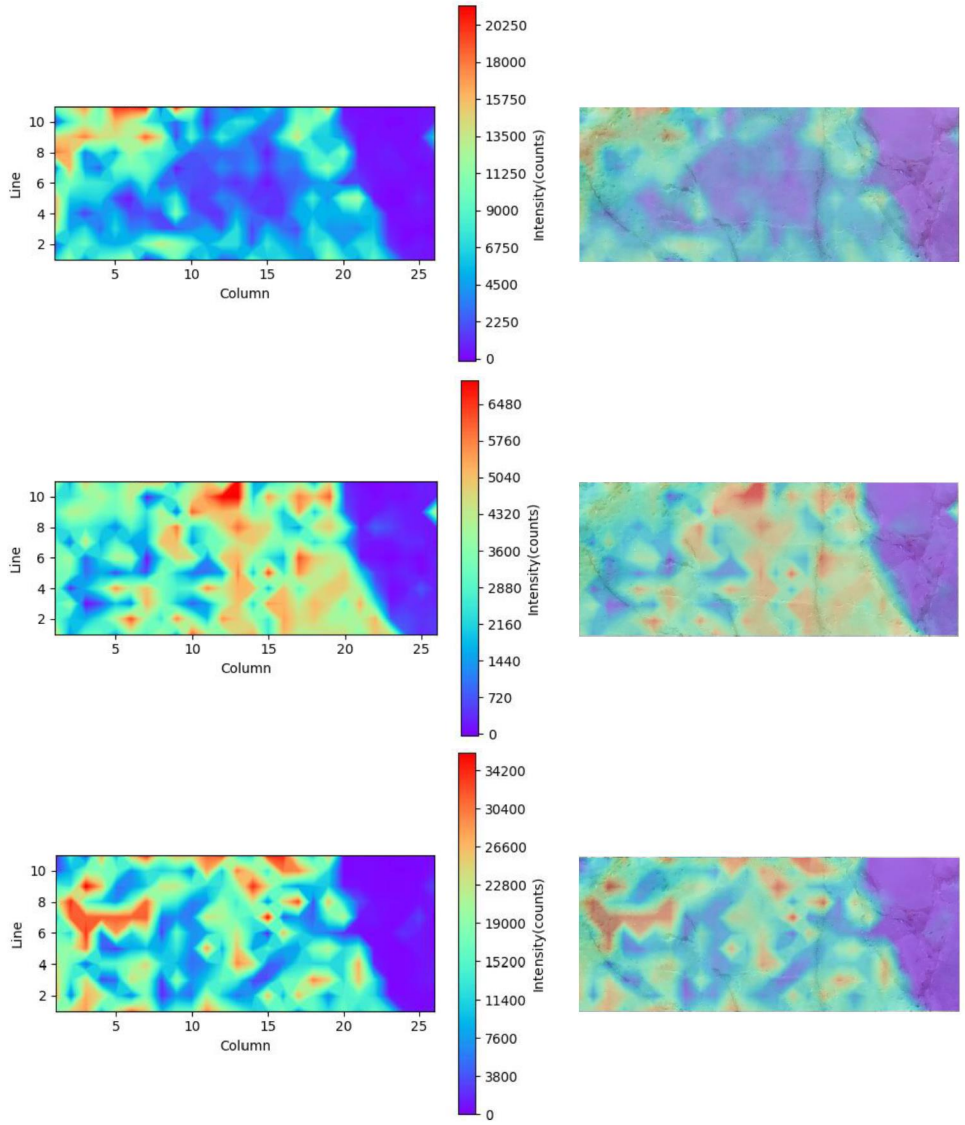

FIGURE 5.7: Map results (left) and map overlaid on the sample (right) for: First line - Copper (327.37 nm). Second Line - Phosphorous (213.59 nm); Third Line - Aluminum (369.09 nm).

All maps were successful, with all desired areas being visible, including its transition zones, which is lost in bulk analysis. The distribution of the elements is in accordance with the mineralogical composition. Observing the Li map and comparing with the Figure 5.5, it can be verified that Turquoise and Quartz show the lower intensities, whilst the Montebrasite region presents the highest ones. However, some points with intermediate counts are already visible in the Montebrasite area, which is an indicator that slight alterations are already occurring. Regarding to the P map, the Montebrasite area shows higher counts, being in accordance with the concentrations of this element in each of these minerals. The Al map shows a very

variable distribution into the Turquoise and Montebrasite regions but was present in both. Lastly, for this specific geological region, Turquoise samples do not show significative levels of Li which can give an indication of the advanced degree of its alteration state.

5.1.2 Petrographic Blade Mapping Analysis

For geologists, LIBS mapping on petrographic blades are of high importance because they allow the comparison between the detailed distribution of each chemical element (provided by LIBS map) with the mineralogical, structural and chemical characteristics obtained through petrographic analysis. The blade in case, has a thickness of approximately 30 μm and was from the same vein of the hydrothermal sample. However, in this case, the Montebrasite is in a more advanced state of alteration. The petrographic blade can be seen in Figure 5.8.

FIGURE 5.8: Petrographic Blade.

As the blade is very fragile, it was necessary to drastically reduce the energy used for the laser shots, to avoid breaking it. Thus, an energy test was performed, allowing to conclude that it was safe to use the 380 μs of Q-Switch delay (energy of 21 mJ), as the exclusive Li line was already visible in Turquoise regions at this energy, despite it being very weak.

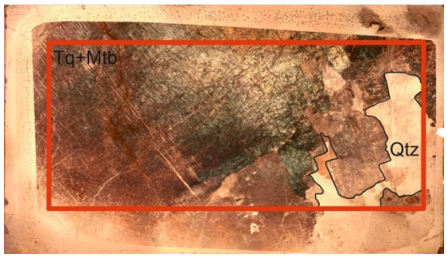

FIGURE 5.9: Crossed Nicols result for the petrographic blade. The red lines represent the mapping area.

A map of 44×18 points was made, with only one shot per spot, into the area highlighted by a red rectangle in the Figure 5.9. In the same Figure it is possible to see the result of a Crossed Nicols. Due to the advanced alteration state of the Montebrasite, both this mineral and Turquoise are mixed over the blade, being only distinguishable the zone relative to Quartz, which is in the upper right corner of the blade, in transparent color.

5.1.2.1 Mapping Results

The results of the LIBS mapping can be seen in Figures 5.10 and 5.11.

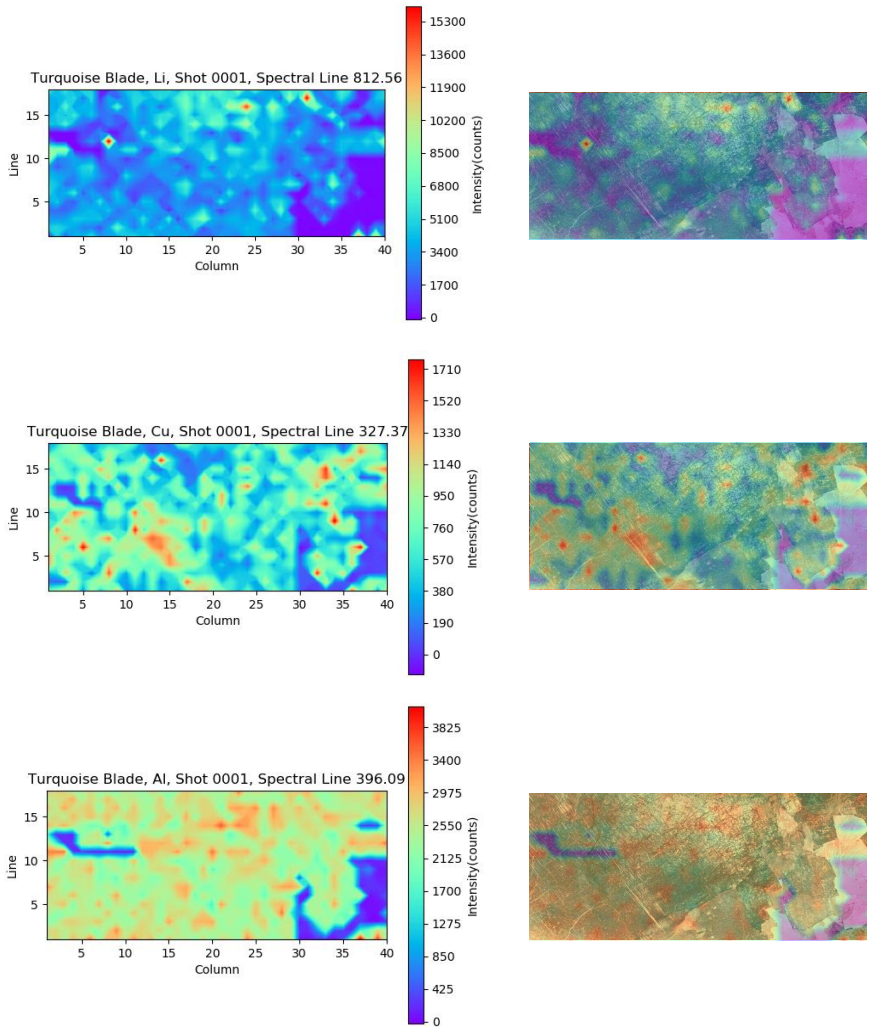

FIGURE 5.10: Petrographic blade result for Li, Cu and Al.

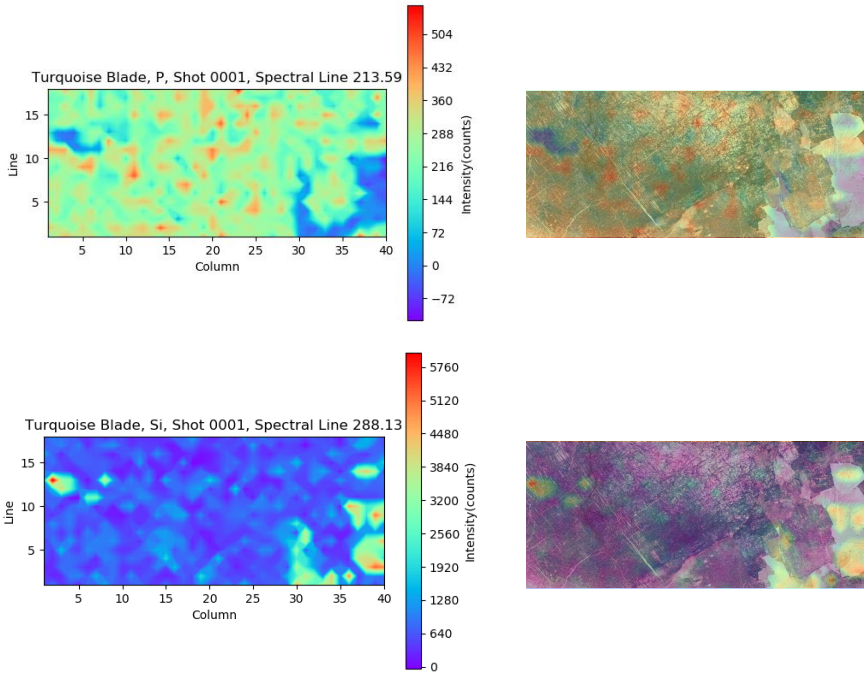

FIGURE 5.11: Petrographic blade result for P and Si.

Observing the maps, it can be seen that in the region composed of Montebrasite mixed with Turquoise, the elements Li, Cu, P and Al are present all over the area, naturally having points with greater intensity than others, which is in agreement with the mineralogical composition. In addition, low intensities of these same elements are visible in the Quartz zone, with Silicon presenting high counts. In summary the results were successful and they are in accordance to the petrographic study. This approach is very promising once it gives geologists a fast and visual way to double check, directly the results of a petrographic blade.

5.1.2.2 Crater dimensions study

Lastly, the laser damage in the petrographic blade was studied. A Leica Microscope* was used to analyze the crater diameter, in a Quartz spot and a in a Montebrasite mixed with Turquoise spot.

*https://www.leica-microsystems.com/products/microscope-objectives/

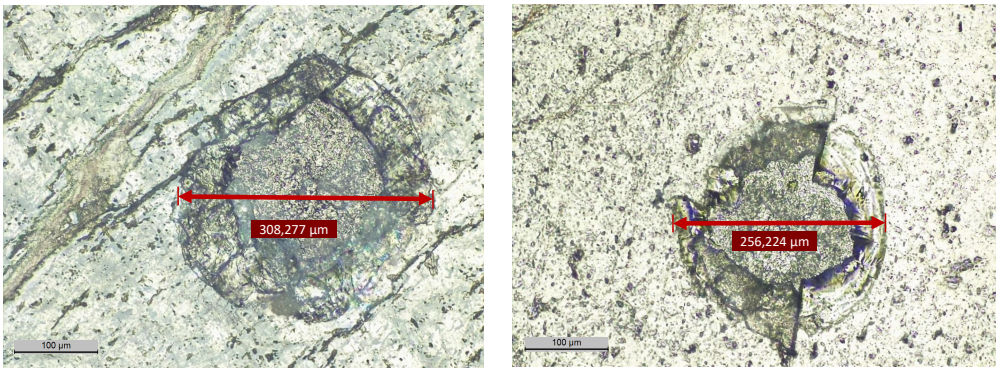

FIGURE 5.12: Microscope image obtained, using $\times 20$ lens, for: Left - Montebrasite mixed with Turquoise area observing a crater with 308.27 μm; Right - Quartz area with a crater of 256.22 μm.

The microscope analysis allowed for an estimate of the damage in the sample. Taking into account that the laser spot size is of $\sim$ 300 μm, and crater diameter caused by a single shot at 380 μs was about 256 μm in Quartz and about 308 μm in Montebrasite mixed with Turquoise, they are similar. The fact that the crater has a small diameter in Quartz, can be an indicator that the hardness of this mineral is higher than that of Montebrasite and Turquoise. This conclusion is corroborated by the Mosh scale, were Quartz shows a hardness of 7, the Montebrasite a hardness between $5_{\frac{1}{2}}$ and 6, and Turquoise a hardness between 5 and 6.

Profilometry was performed too, to assess the depth of the crater in both type of spots: in Quartz and in Montebrasite mixed with Turquoise. The profilometer used in this study is a BRUKER Dektak XT Mechanical Profilometer*, shown in Figure 5.13.

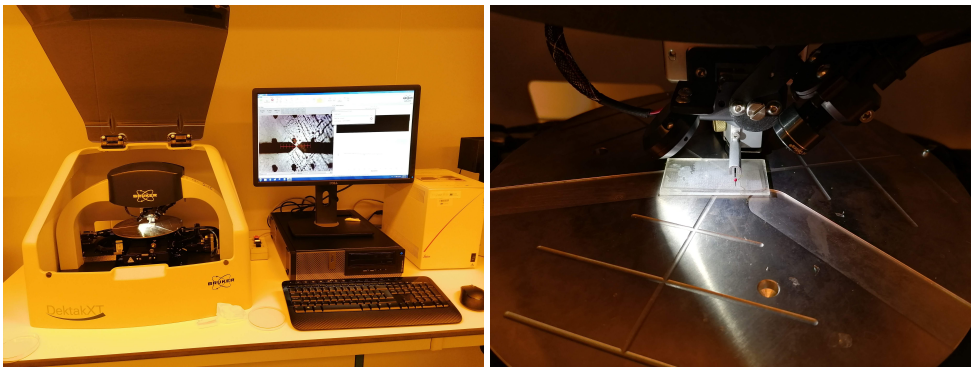

FIGURE 5.13: Left - Profilometer BRUKER Dektak XT. Right - Profilometer scanning needle and sample holder apparatus.

*https://www.bruker.com/products/surface-and-dimensional-analysis/stylus-profilometers/dektak-xt/overview.html

At first, one column of the map was chosen, and a 2D profilometry was made, with a scan resolution of 0.14916 μm, a scan length of 17899.2 μm and the applied force by the stylus was 3 mg. The results obtained can be seen in Figure 5.14.

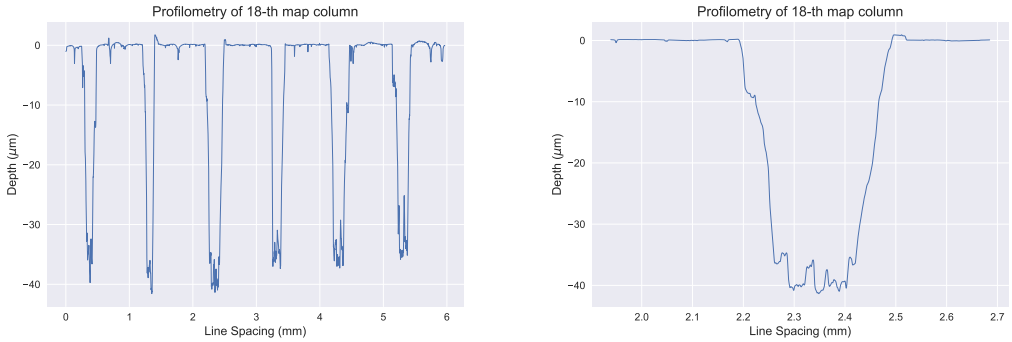

FIGURE 5.14: Left - Profilometry along the first 6 craters of map column; Right - Profilometry zoom in into the 3^{rd} crater.

The graphic of Figure 5.14, allows to conclude that the depth of the craters varies between 35 μm and 41 μm. Thus, the shots reach the supporting blade.

Lastly, a 3D profilometry map was performed in a Quartz spot and in a spot of Montebrasite mixed with Turquoise, allowing for a more detailed analysis of the characteristics of the crater. The results from this study, can be seen in Figure 5.15.

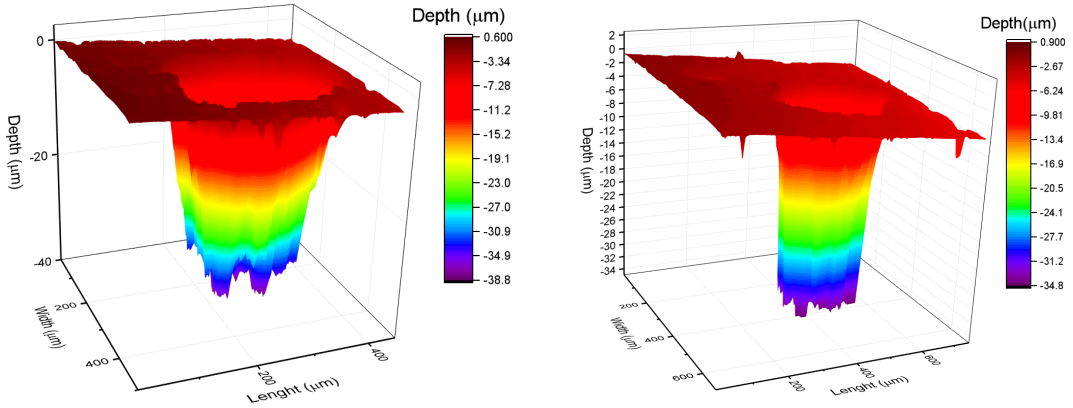

FIGURE 5.15: Left - 3D Profilometry map in a Quartz spot; Right - 3D Profilometry map in a Montebrasite mixed with Turquoise spot.

The results show craters with depths of 35 μm for Quartz and 29 μm for Montebrasite and Turquoise and diameters of 310 μm and 250 μm, respectively. These values are just an example because, as shown in the column profilometry, the craters dimension was variable. Although, this study allows to build a general idea about the damage caused by the laser shots in this type of samples.

5.1.3 Analysis Overview

The Hydrothermal Vein sample study revealed that Turquoise has a very low amount of Li, which allowed to rule out the possibility of a high degree of infiltrations of this element in the Turquoise.

The LIBS technique proved to be an adequate tool to carry out this type of studies on rock samples with successful results in all the approaches.

It was possible to make a map on a petrographic blade without damaging it. This sets a precedent for the LIBS technique to be used as a complementary method to petrography, allowing to see the distribution of all chemical elements within the sample.

The microscope and profilometry analysis allow to measure the crater characteristics in the different minerals, showing depth values between 29 μm and 41 μm and diameters between 250 μm and 310 μm.

5.2 Petalite vs Spodumene

Lithium is a chemical element, typically found in a group of minerals called Aluminosilicates of Li [85]. In these group, the minerals with higher economic importance are Petalite, Spodumene and Lepidolite, because they are the most litiferous, i.e., they have the highest concentrations of Lithium in its composition [86]. In this section a process of differentiation between two minerals, Petalite and Spodumene, is studied. Due to the escalating demand for Li, element which can only extracted, in a cost-efficient way, from spodumene, there is a need to improve this mineral identification. The application of the LIBS methodology to this problem will have large ramifications in industry. Spodumene and Petalite, showed in Figure 5.16, are composed by the same chemical elements, although they are in different concentrations. The chemical formula and concentrations of both minerals are in the Table 5.2.

FIGURE 5.16: Specimen of: Left - Spodumene; Right - Petalite.

TABLE 5.2: Mineral chemical formulas and element concentrations according to [55].

Mineral	Chemical Formula	Concentrations (%)			
		Li	Al	Si	O
Spodumene	$LiAlSi_2O_6$	3.73	14.50	30.18	51.59
Petalite	$LiAlSi_4O_{10}$	2.09	8.75	36.72	52.43

Taking this information into account, it is to be expected that the behavior of the spectral lines being different for both minerals. To simplify the analysis, a group of three characteristic lines were selected for each element, which the wavelengths presented in Table 5.3. The Oxygen lines were not used in this study because this element was part of the atmosphere and its line intensities were going to be influenced by the concentration of this element in the atmosphere.

TABLE 5.3: Wavelengths chosen for each chemical element.

Element	Li	Al	Si
Wavelengths (nm)	460.24	309.25	212.39
	610.22	394.34	251.58
	812.56	396.09	288.13

5.2.1 Experimental Procedure

To perform this study, 13 samples (7 spodumenes and 6 petalites) were selected, all of them monomineralic (Table 5.4).

TABLE 5.4: Set of Spodumenes and Petalites.

Number	Sample	Origin
1	Spodumene	Brazil
2	Spodumene	Brazil
3	Spodumene	Brazil
4	Spodumene	Brazil
5	Spodumene	Brazil
8	Petalite	Brazil
9	Petalite	Brazil
10	Petalite	Queiriga
11	Petalite	Bajoca
16	Spodumene	California
41	Spodumene	Capoeira
42	Petalite	CHN3
182	Petalite	NIST (certified)

The LIBS protocol used to execute this study was illustrated in 5.17.

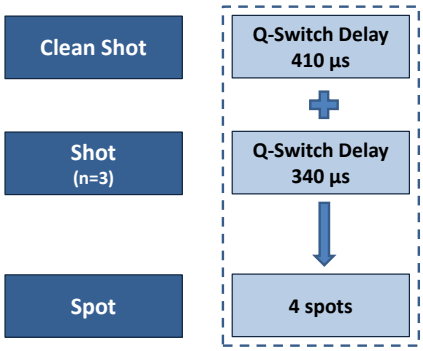

FIGURE 5.17: Protocol for differentiation between Petalite and Spodumene.

This protocol was applied to each sample. Because these samples were not previously cut, was necessary to be careful and place the sample as perpendicular as possible to the laser plane, in order to be able to move the sample without moving it away from the laser focus.

To make this differentiation a Principal Component Analysis (PCA) was applied. This method is very useful to interpret datasets with many variables, which in practice translates into a problem with many dimensions. This technique allows a reduction of dimensionality, in order to easily understand its information, identifying the differences and similarities, and creating data patterns [87]. In this process, a group of new orthogonal variables is created, in a lower number, but avoiding relevant data loss [88]. These new variables are result of a linear combination of the dataset variables and they are the so-called Principal Components [89]. With data projection, the direction that maximizes its variance is defined as the first principal component. The other components, i.e., i-th principal components, are orthogonal to the first one.

5.2.2 Results

With the collected data, the results obtained for a Q-Switch delay of 340 μs (energy of 48.5 mJ) was selected for the PCA implementation, as none of the selected lines reached saturation at this energy value. The intensity counts used for the PCA analysis, were the result of the mean of the twelve shots performed for each sample. For all the spectra, the baseline was previously removed using the Asymmetric Least Squares Smoothing method, discussed in Subsection 4.3.1.2. To performed

the PCAs the `PCA`* function of the `sklearn`, a machine learning `Python` module was used.

To simplify the identification of the different samples in the PCA, the correspondences indicated in the Table 5.5 were chosen.

TABLE 5.5: Relation between the PCA label and the sample name.

Number	PCA label	Mineral	Number	PCA label	Mineral
1	S1	Spodumene	10	S8	Petalite
2	S2	Spodumene	11	S9	Petalite
3	S3	spodumene	16	S10	Spodumene
4	S4	Spodumene	41	S11	Spodumene
5	S5	Spodumene	42	S12	Petalite
8	S6	Petalite	182	S13	Petalite
9	S7	Petalite			

The PCA obtained, using the 9 wavelengths indicated in Table 5.3 as variables, can be seen in Figure 5.18.

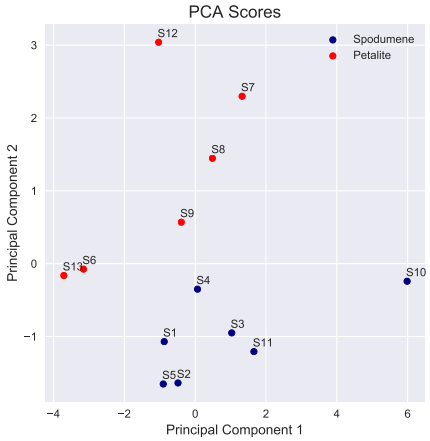

FIGURE 5.18: 2D PCA score plot obtained for 340 μs of Q-Switch delay. The red points represent the Petalite samples and the blue points the Spodumene ones.

For 340 μs, the PC1 score was 58% and the PC2 score was 22%, whereby this PCA used 80% of the total information.

Observing the graphic, it can be seen that the Spodumenes and Petalites were organized in two well defined clusters. In this case, the Principal Component Analysis was able to correctly distinguish these two minerals, by just using the intensities of 3 characteristic lines of the 3 compositional elements. In order to know which variables strongly influences the principal components and which ones are used for the discrimination a loading plot was made, as indicated in Figure 5.19.

*https://scikit-learn.org/stable/modules/generated/sklearn.decomposition.PCA.html

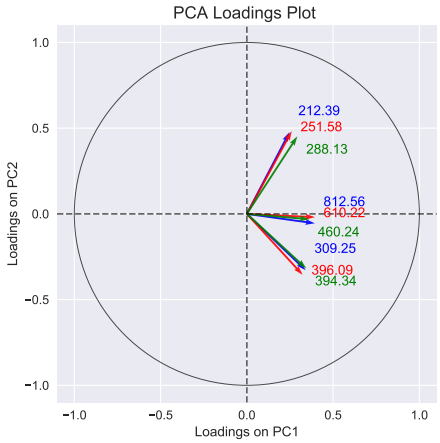

FIGURE 5.19: PCA loading plot obtained for 340 μs of Q-Switch delay. Here its possible to see the load representation of each wavelength (indicated at red, blue and green) in each principal component.

Through the loading graphic it is possible to see that all the lines were grouped in three specific directions, indicating that these variables were very positively correlated. Observing the projections of all the vectors on the principal components axis, it is possible to conclude that the Si wavelengths are the variables that most positively influence the PC2, while the Li lines were the variables that most influence positively the PC1. Thus, the Li lines having a higher weight on this PCA.

Because the Li concentrations in both minerals are very close, in some more complex cases, using Li lines for this discrimination may not be the best option. Thus, the same PCA, without considering the Li characteristic lines, was made and the results can be seen in Figure 5.20.

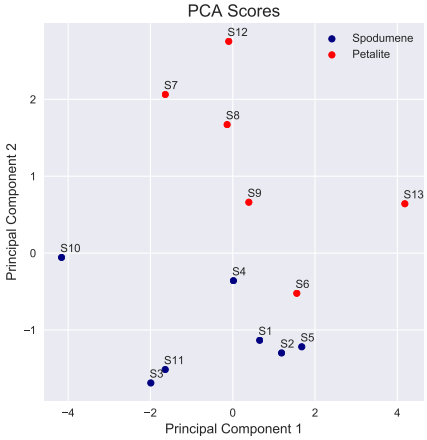

FIGURE 5.20: 2D PCA score plot obtained for 340 μs Q-Switch delay without Li's lines. The red points represent the Petalite samples and the blue points the Spodumene ones.

Observing the new PCA, one more time, the differentiation between Spodumene and Petalite is visibly, so the Al and Si variables were sufficient to correctly discriminate these minerals.

Although, it is important to extend the number of samples of both minerals, to better define the boundary between them and improve the algorithm results.

5.2.3 Analysis Overview

The Principal Component Analysis was able to correctly group the set of samples selected. In all cases, two clusters of samples are visible without the presence of intersections or outliers. This highlights the potential of the LIBS technique, since, despite all the limitations of the system, it provides data with enough quality to enable to distinction between two minerals with the same chemical composition.

The Principal Component Analysis was also proved to be an important tool to reduce the dimensionality of the data set, providing a good result.

It was possible to distinguish the two minerals without having to resort to Li's characteristic lines. The results using only the Al and Si lines were very similar to the previous ones, showing both two clusters of samples.

Taking into account the small number of samples this study is already promising. However, it was verified the necessity of analyze a larger number of samples, which would allow to improve the output information and, consequently, provide a better determination of the boundary between those two groups of minerals.

5.3 Lithium Quantification

The quantification of an analyte using LIBS can be a hard task, because there are many system fluctuations, as discussed in Section 3, that influence the spectral intensities. In addition to this, minerals and rocks shown heterogeneities and typically have complex composition. Another problem is the matrix effect that changes the intensities and line areas, making them not proportional to the concentration of the element [90].

In literature, there are many methods used to quantify the LIBS measurements. A few that cover most of the methods used will be analyzed in more detail. Devangard *et al.* reports the using of a calibration curve to estimate the unknown concentrations in order to quantifying Mn in Glass matrices [91]. The spectra are previous normalized to an internal standard (Fe), to improve the results. The results of this univariate methods were compared with the results obtained using Principal Component Regression and Partial Least Squares. The author presents an improvement of this metric when using multivariate methods.

Tomoko Takahashi and Blair Thornton describe four distinct methods that starts with the traditional calibration curve. The calibration-Free (CF-LIBS) it is another technique showed. It uses the Boltzmann and Saha-Boltzmann equations to determine the plasma electron density and its temperature, allowing to obtain the concentration of unknown samples. Some multivariate methods were referred too, as well as PLS, PCR and Artificial Networks [51].

Guangmeng Guo *et al.* shows the results obtained for quantification of samples from soils, with the Calibration Curve method, PLS and Support Vector Regression (SVR). The best results were obtained for PLS method [92].

Yang Hu *et al.* used Artificial Networks to quantify geological samples using a nanosecond LIBS and analyze the matrix effect [56].

The idea that the use of multivariate analysis leads to better results seems to be consensual, because it had the capacity of avoiding the matrix effects, due to taking into account the entire spectrum or a part of it, instead of a single elemental line.

5.3.1 Experimental Procedure

A drill hole, 18 PNR RC 005, from a pegmatite mine in Barroso, a region in the North of Portugal, was studied with the goal validating the Li measurements obtained by LIBS.

The drill hole has an extension of 128 meters, along which the powder from of the reverse circulation drilling process was sampled, meter by meter, and stored. In this study the final 49 meters were studied, with all of them being composed by Pegmatite. A portion of the powder was sent for ICP-MS analysis, whilst the rest was used for the LIBS analysis.

As the samples were in powder format, little sample preparation was required. First, the powder was milled and sieved. After this, two pellets were made with the procedure described in Appendix C.1.

The protocol used for the LIBS analysis is shown in Figure 5.21

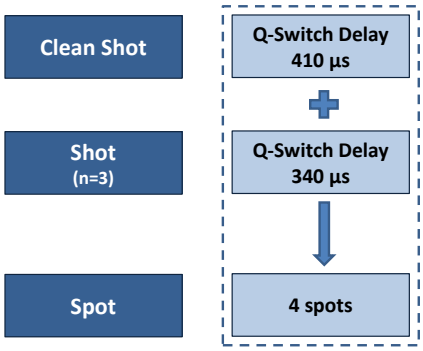

FIGURE 5.21: Protocol used for the drill pellets LIBS analysis.

As the 812.62 nm Li line showed very low counts, even when using a Q-Switch delay of 340 μs, the Li line selected for the study was the 610.37 nm, as it both showed the higher peak intensities and no evidence of self-absorption in them.

With the twelve shots collected for each meter sample, at 340 μs, the peak area was calculated. For this, the spectral values, contained between the local minima of each side of the Li line, were used. The mean of the calculated areas was used as the final value for the intensity, to reduce the dispersion of the data and improve the results. The ICP-MS concentrations were used as reference values.

For the quantification of the data, a machine learning method was used. For this purpose Neural Networks were used, specifically a Multi-Layer Perceptron (MLP). This algorithm uses a N-dimensional dataset, and the output should have P dimensions. A Neural Network can be thought as a linear sequence of layers, each composed by one or more neurons, where the outer edges are the input/output layers (with size Y and P, respectively) and, the middle ones are the so-called hidden layers, as shown in Figure 5.22 [93, 94].

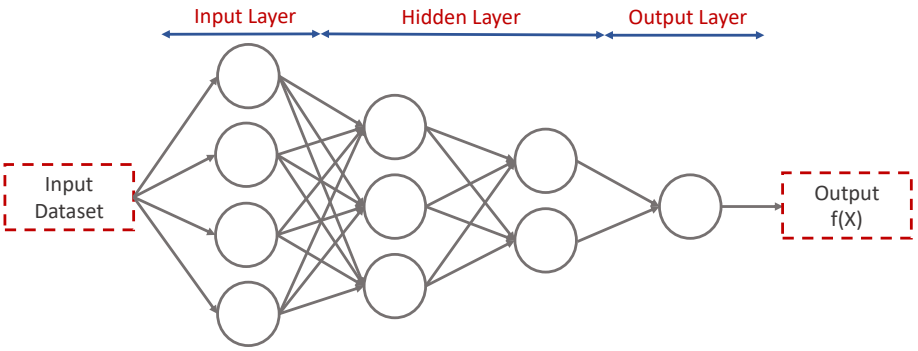

FIGURE 5.22: Schematic of a Neural-Network.

Each neuron of the network accepts N inputs and outputs and its result is dependent of the activation function, as illustrated in Figure 5.23. The Y result depends on the weight, w_i, associated with each X_i and the bias of the neuron (Equation 5.1). The weight represents the importance of the i-th input for the output. On the other hand, the bias represents, the ease of activating the node.

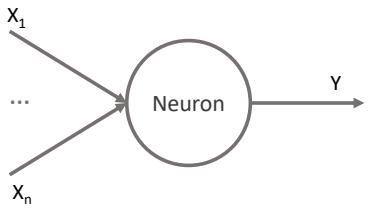

FIGURE 5.23: Schematic of a Neuron with N inputs.

$$Y = f\left(\sum_i w_i x_i + bias\right) \tag{5.1}$$

The function `MLPRegressor`* from `sklearn`† `Python` module was used, to performed the quantifications. This method uses a backpropagation training algorithm in which the output layer as no activation function. The loss function is determined by the square error, i.e., the squared difference between the predicted value and the "real" one.

The Leave-One-Out cross-validator was also used to improve the training of the model. With this methodology, only one sample of the dataset is selected to be tested, at a time, whilst all others are used as a training set. This type of approach

*https://scikit-learn.org/stable/modules/generated/sklearn.neural_network.MLPRegressor.html
†https://scikit-learn.org/stable/about.html#citing-scikit-learn

usually leads to better results, as shown in [95]. Thus, the `LeaveOneOut`* function of `sklearn` module was implemented too.

5.3.2 Results

In order to assess about how disperse is the dataset, a plot was made and a linear regression was performed. The graphic obtained is in Figure 5.24.

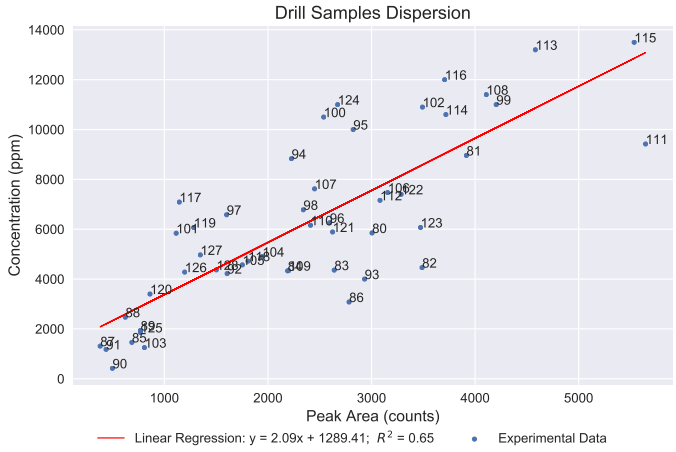

FIGURE 5.24: Plot of the drill hole dataset and its linear regression.

The correlation coefficient obtained for the linear regression was just 0.65, which shows that the data is quite dispersed. Through this fit, a LOD of 53 ppm and LOQ of 173 ppm were determined, which are considerably above those found for the ideal case, exposed in subsection 3.4.3 for the same Li line.

The concentrations predicted by the MPL Regression with the Leave-One-out cross validation, can be seen in Tables 5.6 and 5.7. As the estimated concentrations present some deviations of the expected values, a Semi - Quantification based on 3 Levels were made. The goal is to divide the Li concentrations of interest into three different sets according to the prospection values: $<464\ \mu g/g$, >464 and $<4640\ \mu g/g$ or $>4640\ \mu g/g$. The final set is the most interesting one, as Li exploration is only viable if its concentrations are higher than $4640\ \mu g/g$ that corresponds to a Li_2O concentration of $1\ \mu g/g$.

*https://scikit-learn.org/stable/modules/generated/sklearn.model_selection.LeaveOneOut.html

TABLE 5.6: Results obtained for drill samples quantification, using MPL Regression with Leave-One-Out cross validation.

Sample Meter	Conc. ICP-MS ($\mu g/g$)	Conc. MPL ($\mu g/g$)	Classification ($\mu g/g$)	Validation
80	5850	7620	>4640	True
81	8960	9911	>4640	True
82	4460	8945	>4640	False
83	4360	6701	>4640	False
84	4330	5538	>4640	False
85	1460	1731	>464 and <4640	True
86	3080	7103	>4640	False
87	1310	959	>464 and <4640	True
88	2470	1571	>464 and <4640	True
89	1940	1940	>464 and <4640	True
90	420	1257	>464 and <4640	False
91	1180	1103	>464 and <4640	True
92	4220	4048	>464 and <4640	True
93	4000	7478	>4640	False
94	8830	5569	>4640	True
95	10000	7050	>4640	True
96	6260	6550	>4640	True
97	6580	4018	>464 and <4640	False
98	6780	5888	>4640	True
99	11000	10574	>4640	True
100	10500	6322	>4640	True
101	5840	2799	>464 and <4640	False
102	10900	8727	>4640	True
103	1250	2037	>464 and <4640	True
104	4900	4904	>4640	True
105	4570	4419	>464 and <4640	True
106	7470	7969	>4640	True
107	7620	6152	>4640	True
108	11400	10302	>4640	True
109	4340	5563	>4640	False
110	6160	6077	>4640	True

TABLE 5.7: Results obtained for drill samples quantification, using MPL Regression with Leave-One-Out cross validation (continuation).

Sample Meter	Conc. ICP-MS (μg/g)	Conc. MPL (μg/g)	Classification (μg/g)	Validation
111	9420	14700	>4640	True
112	7160	7786	>4640	True
113	13200	11444	>4640	True
114	10600	9322	>4640	True
115	13500	13986	>4640	True
116	12000	9234	>4640	True
117	7090	2870	>464 and <4640	False
118	4720	4555	>464 and <4640	False
119	6070	3222	>464 and <4640	False
120	3400	2169	>464 and <4640	True
121	5890	6629	>4640	True
122	7400	8311	>4640	True
123	6070	8848	>4640	True
124	11000	6651	>4640	True
125	1860	1940	>464 and <4640	True
126	4280	3011	>464 and <4640	True
127	4970	3389	>464 and <4640	False
128	4370	3784	>464 and <4640	True

Tables 5.6 and 5.7 show that the concentrations given by the semi-quantification model are accurate in 36 of 49 samples, representing a success rate of 74%. Nevertheless, there is a large variation of estimated concentrations, with the %BIAS ranging from 0.02% up to 130%. In addition, 50% of the samples under study showed Li concentrations above 4640 (μg/g), in other words, only 25 meters present good results for prospection, falling short of the expectations set for the vein.

These results highlight the difficulty in correctly quantifying geological samples, due to the large number of factors in play, all contributing to the quantification errors. The use of a protocol with larger shot ranges can help to diminish the variability of the measurements. It is also necessary to improve the algorithm used and resort to artificial intelligence to achieve a more robust quantification. The application of signal processing that can take into account the physical phenomena can also contribute for better results. Despite the negative aspects, this methodology shows a significant improvement, when compared to the simple calibration curve

that was previously studied. Furthermore, it is also important to keep in mind that the division of the powder between LIBS and ICP-MS does not guarantee equal concentrations in both samples.

5.3.3 Analysis Overview

The MPL Regressor was able to semi-quantify the samples, with a success rate of 74% over the tested data set, in spite of all problems inherent to the quantification of geological samples.

In this way, it is necessary to develop a more complex approach that allows to correct the spectra considering the physical phenomena that are present, to be able to obtain better results. Increasing the protocol number of shots can help too to decrease the variability of measurements and thus allow more accurate quantification.

Another ICP-MS measurement of the same samples analyzed in LIBS can be a good option to discard differences into the concentration of the both powder slots, because this will allow to determine whether the constraints in quantification are the result of the characteristics of the samples or from the method itself.

Chapter 6

Conclusion and Future Work

6.1 Conclusion

In a general view, LIBS shows to be a good analytical tool. It is a very versatile tool, allowing to study samples of various types, both in powder, bulk or blade format. With this method it is still possible to make localized measurements, mappings, differentiations between minerals and semi-quantifications, in a short time.

In the first part of this thesis, a study about the characteristics and limitations of the system, was made. The spectrometer channel CCD resolutions were determined, as well as the best channel for each overlap region, in 6 of the 7 channels. The laser pulse study allowed to determine the magnitude of the power fluctuations and the relation between the FHWM behavior and the energy. The Quality Control graphics showed that, in general, all the measurements were between the 2 standard deviations of the average value. The Li calibration curve, performed with the Li_2CO_3 pellets for the 610.37 nm and 812.62 nm Li lines, showed very good correlation coefficients, of 0.984 and 0.989, respectively. The LOD, found for the first line, was 6 ppm and for the last one, 62 ppm. The precision of the system was in the order of the 20%.

Passing now for the spectral manipulation and the development of the analytical tool for spectral element lines search, the process begun with the construction of an Element Exclusive Lines routine. It allows to determine the exclusive wavelengths of 77 elements of the periodic table, using the information contained in the NIST

database. After this, was possible to determine the atmosphere elements and contaminations, in order to identify more clearly this line into the LIBS spectra. Some algorithms were tested for baseline simulation to find which was the best one for the LIBS spectra, with the ALSS showing the best results. After this process, the Element Search Tool was developed and tested in pure samples and minerals, being capable of detected with success all the pure samples composition and, in average, 85% of the mineral sample's composition.

The Hydrothermal Vein sample study allowed to detect Li presence into the Montebrasite and a residual amount into the Turquoise and Quartz, with the possibility of Li high infiltration in Turquoise being discarded. This was performed using a qualitative analysis, with resource to surface mappings in a hand sample. In the first ever study of this type, the same analysis was also performed in a petrographic blade with just ~ 30 μm of thickness. All the results were in accordance with the expected. A damage study was already determined, using a microscope and a profilometer, and the results illustrated a crater depth between 29 ad 41 μm and a diameter in the order of the laser spot size, 300 μm.

The differentiation Spodumene - Petalite, was the next step. The PCA score plot showed two groups of samples, and this process had similar results even without the variables correspondent of Li lines, indication that this discrimination was not based on this element. Although an increase of the samples set is important to improve the results and improve the robustness of the method.

Finally, the Drill Hole semi-quantification, using Neural Networks, was able to correctly classify 74% of the samples under study. This result shows the necessity of applying more complex analysis and manipulations of the spectra, for example using scattering baseline corrections and Artificial Intelligence, to reduce the varieties in shot-to-shot measurements and correct the matrix effect, improving the final results.

6.2 Future Work

There are some points to develop in order to improve the performance of the LIBS system, as well as the range of analyzes that can be done. The implementation of a

fixed photodetector into the LIBS chamber, will allow to make a real-time study of the laser drift.

The addition of a camera to the LIBS system, will be useful to study the plasma plume behavior under a larger set of parameters, such as different sample characteristics, repetition rates and atmospheric conditions.

The element search tool still needs to be optimized. The increase of the pure samples set will improve the calibration of the system, allowing to perform a spectral analysis for a higher number of chemical elements, contributing to an improvement of the performance of this routine.

The study of different gate time delays will allow the acquisition of the spectra in several plasma states.

The introduction of scattering baseline corrections can improve the shot-to-shot variabilities.

Lastly, the increase of the database of monomineralic spodumenes and petalites will improve the capacity of the presented algorithms to distinguish between those similar minerals.

Appendix A

A.1 Quality Control Interface

The Quality Control graphic interface was created in `Python` and can be seen in Figure A.1.

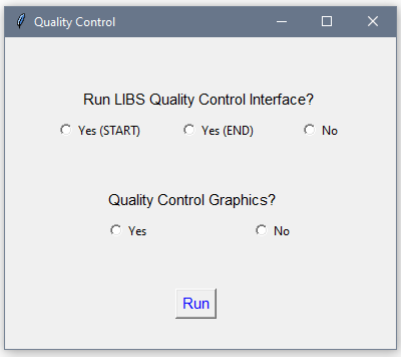

FIGURE A.1: Quality Control Interface.

This interface allows the user to choose between performing the beginnig or end day measurements. It is also possible to choose neither option and run the Quality Control graphics with the existing data.

All the folders necessary to save the data measurements are created automatically by this routine. After the folders creation, a message appears to remind the user to mention this sub-folder in AvaSoft, the program responsible for recording the spectra.

After this, the LIBS system is put into operation, with the laser, translation stages and the spectrometer being controlled by the scripts previously developed by members of the LIBS team.

When the shots are performed, according to the protocol in Figure 3.11, another message appears asking for the data to be converted from RAW8 to TXT, so that it

can be easily interpreted in `Python`. To preserve the original data, a zip file is created with all the information and saved in a specific directory.

Finally, if the option to generate graphs was activated, the data will be analyzed and two graphics will be processed for each Q-Switch value, one referring to the measurements made at the beginning of the day and the other relative to those made at the end.

Appendix B

B.1 Laser Pulse Shapes

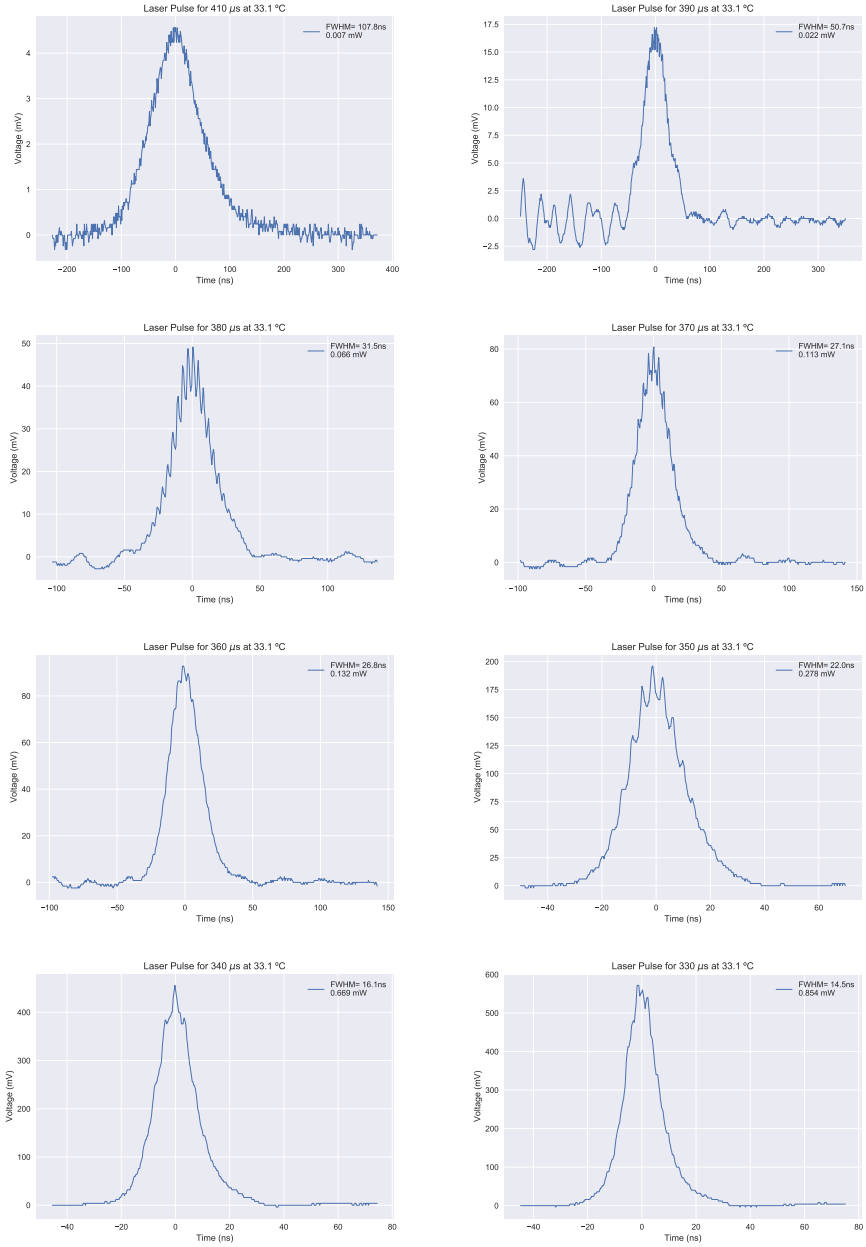

FIGURE B.1: Laser Pulse Shaper for Q-Switch Delays between 410 μs and 330 μs.

Appendix C

C.1 Sample preparation

Sample preparation starts with the weighing the compound with a precision balance with four decimal places (Figure C.1 - Left). After this both compounds are mixed, using a mortar and a pestle until the mixture is well homogenized.

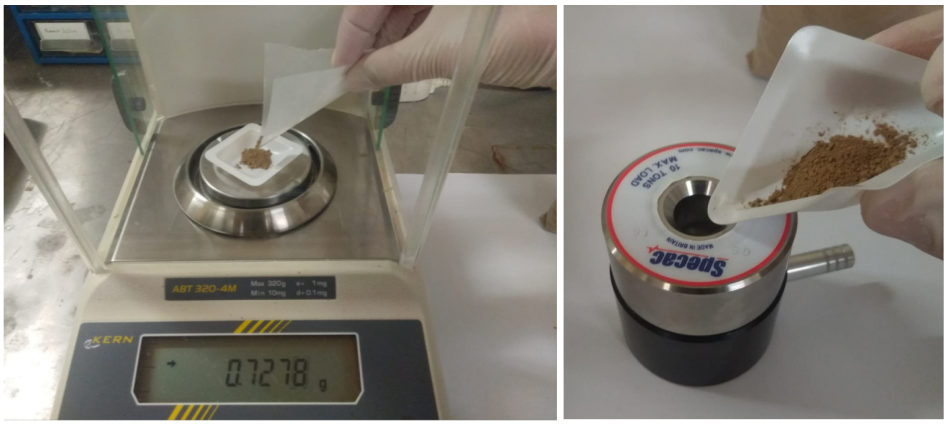

FIGURE C.1: Left: Weighing of the compound. Right: Slide the compound into the die body.

Afterwards, the compound is put into the die body of evacuable pellet die (Figure C.1 - Right)

Insert a steel pellet into the die body and push until it is fixed in place. Repeat all the process above, for the second pellet. When finished, insert the die plunger with the side, whose edges are not chipped, facing down and press it again. The rubber o-ring is then fitted to the die plunger until it is well adjusted to the body (Figure C.2).

FIGURE C.2: Left: Die plunger and o-ring into the die body. Right: Die body into the press.

Put the die body into the press in the position indicated in Figure C.2 - Right and centered in the lower bolster. From here on out the process follows then one described in the manufacturer website*.

*https://www.specac.com/en/documents/instructional/2i-15011-14-atlas-manual-hydraulic-press

Appendix D

D.1 Baseline Simulations

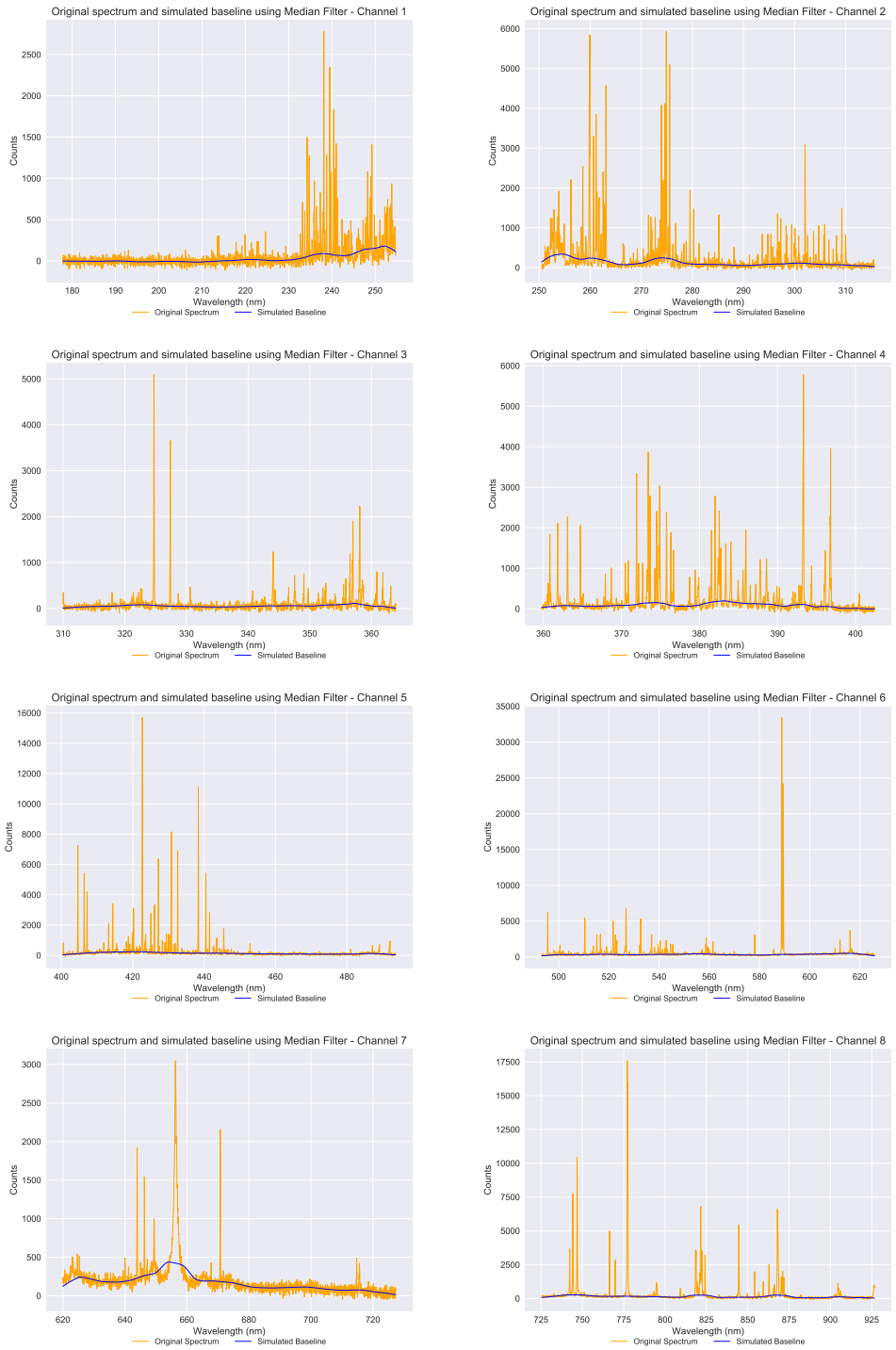

FIGURE D.1: Median Filter baseline simulation for Fe spectra, for each spectrometer channel.

FIGURE D.2: Asymmetric Least Squares Smoothing baseline simulation for Fe spectra, for each spectrometer channel.

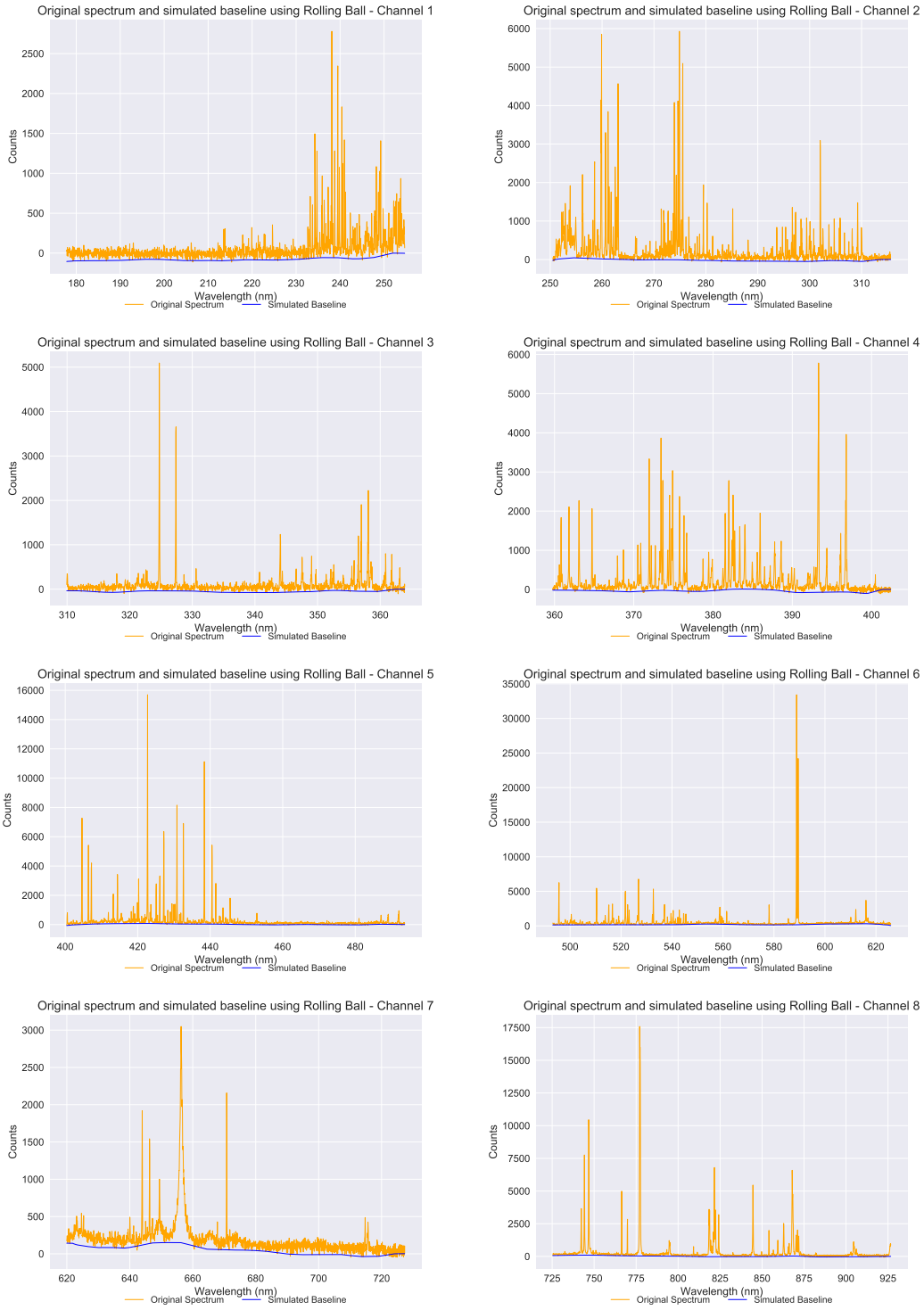

FIGURE D.3: Rolling Ball baseline simulation for Fe spectra, for each spectrometer channel.

Bibliography

[1] J. A. Ober, "U.S. Geological Survey Minerals Yearbook - 2000 - Lithium," 2000. [Online]. Available: https://s3-us-west-2.amazonaws.com/prd-wret/assets/palladium/production/mineral-pubs/lithium/450400.pdf

[2] B. W. Jaskula, "U.S. Geological Survey Minerals Yearbook 2010 - Lithium," 2012. [Online]. Available: https://s3-us-west-2.amazonaws.com/prd-wret/assets/palladium/production/mineral-pubs/lithium/myb1-2010-lithi.pdf

[3] United States Geological Survey (USGS), "Mineral Commodity Summaries 2020," no. 703, pp. 98–99, 2020.

[4] B. Tadesse, F. Makuei, B. Albijanic, and L. Dyer, "The beneficiation of lithium minerals from hard rock ores: A review," *Minerals Engineering*, vol. 131, pp. 170 – 184, 2019. [Online]. Available: http://www.sciencedirect.com/science/article/pii/S0892687518305089

[5] M. T. Sweetapple and S. Tassios, "Laser-induced breakdown spectroscopy (LIBS) as a tool for in situ mapping and textural interpretation of lithium in pegmatite minerals," *American Mineralogist*, vol. 100, no. 10, pp. 2141–2151, oct 2015.

[6] R. S. Harmon, C. J. M. Lawley, J. Watts, C. L. Harraden, A. M. Somers, and R. R. Hark, "Laser-induced breakdown spectroscopy-An emerging analytical tool for mineral exploration," *Minerals*, vol. 9, no. 12, pp. 1–45, 2019.

[7] D. A. Cremers and L. J. Radziemski, *Handbook of Laser-Induced Breakdown Spectroscopy*, 2nd ed. Wiley Sons Ltd, 2013.

[8] V. N. Rai and S. N. Thakur, "Physics of plasma in laser-induced breakdown spectroscopy," *Laser-induced breakdown spectroscopy*, pp. 83–111, 2007.

[9] A. K. Pathak, N. K. Rai, A. Singh, A. K. Rai, P. K. Rai, and P. K. Rai, "Medical applications of laser induced breakdown spectroscopy," vol. 548, no. 1, 2014.

[10] M. Gazmeh, M. Bahreini, S. H. Tavassoli, and M. Asnaashari, "Qualitative analysis of teeth and evaluation of amalgam elements penetration into dental matrix using laser induced breakdown spectroscopy," *Journal of Lasers in Medical Sciences*, vol. 6, no. 2, pp. 67–73, 2015.

[11] A. Giakoumaki, K. Melessanaki, and D. Anglos, "Laser-induced breakdown spectroscopy (LIBS) in archaeological science-applications and prospects," *Analytical and Bioanalytical Chemistry*, vol. 387, no. 3, pp. 749–760, 2007.

[12] A. Botto, B. Campanella, S. Legnaioli, M. Lezzerini, G. Lorenzetti, S. Pagnotta, F. Poggialini, and V. Palleschi, "Applications of laser-induced breakdown spectroscopy in cultural heritage and archaeology: A critical review," *Journal of Analytical Atomic Spectrometry*, vol. 34, no. 1, pp. 81–103, 2019.

[13] G. S. Senesi, J. Cabral, C. R. Menegatti, B. Marangoni, and G. Nicolodelli, "Recent advances and future trends in LIBS applications to agricultural materials and their food derivatives: An overview of developments in the last decade (20102019). Part II. Crop plants and their food derivatives," *TrAC Trends in Analytical Chemistry*, vol. 118, pp. 453–469, 2019.

[14] M. Markiewicz-Keszycka, X. Cama-Moncunill, M. P. Casado-Gavalda, Y. Dixit, R. Cama-Moncunill, P. J. Cullen, and C. Sullivan, "Laser-induced breakdown spectroscopy (LIBS) for food analysis: A review," *Trends in Food Science and Technology*, vol. 65, pp. 80–93, 2017. [Online]. Available: http://dx.doi.org/10.1016/j.tifs.2017.05.005

[15] F. Colao, R. Fantoni, V. Lazic, A. Paolini, F. Fabbri, G. G. Ori, L. Marinangeli, and A. Baliva, "Investigation of LIBS feasibility for in situ planetary exploration: An analysis on Martian rock analogues," *Planetary and Space Science*, vol. 52, no. 1-3, pp. 117–123, 2004.

[16] S. Nisar, G. Dastgeer, M. Shafiq, and M. Usman, "Qualitative and semi-quantitative analysis of health-care pharmaceutical products using laser-induced breakdown spectroscopy," *Journal of Pharmaceutical Analysis*, vol. 9, no. 1, pp. 20–24, 2019.

[17] B. Thornton, T. Takahashi, T. Sato, T. Sakka, A. Tamura, A. Matsumoto, T. Nozaki, T. Ohki, and K. Ohki, "Development of a deep-sea laser-induced breakdown spectrometer for in situ multi-element chemical analysis," *Deep-Sea Research Part I: Oceanographic Research Papers*, vol. 95, pp. 20–36, 2015. [Online]. Available: http://dx.doi.org/10.1016/j.dsr.2014.10.006

[18] S. K. Hussain Shah, J. Iqbal, P. Ahmad, M. U. Khandaker, S. Haq, and M. Naeem, "Laser induced breakdown spectroscopy methods and applications: A comprehensive review," *Radiation Physics and Chemistry*, vol. 170, p. 108666, 2020. [Online]. Available: http://www.sciencedirect.com/science/article/pii/S0969806X1931343X

[19] B. Zhang, P. Ling, W. Sha, Y. Jiang, and Z. Cui, "Univariate and multivariate analysis of phosphorus element in fertilizers using laser-induced breakdown spectroscopy," *Sensors (Switzerland)*, vol. 19, no. 7, 2019.

[20] D. M. Díaz Pace, N. A. Gabriele, M. Garcimuño, C. A. D'Angelo, G. Bertuccelli, and D. Bertuccelli, "Analysis of minerals and rocks by laser-induced breakdown spectroscopy," *Spectroscopy Letters*, vol. 44, no. 6, pp. 399–411, 2011.

[21] N. J. Mcmillan, S. Rees, K. Kochelek, and C. Mcmanus, "Geological applications of laser-induced breakdown spectroscopy," *Geostandards and Geoanalytical Research*, vol. 38, no. 3, pp. 329–343, 2014.

[22] L. Streubel, L. Jacobsen, S. Merk, M. Thees, D. Rammlmair, J. Meima, and D. Mory, "Rapid Analysis of Geological Drill-Cores with LIBS: On the use of laser-induced breakdown spectroscopy," *Optik & Photonik*, vol. 11, no. 5, pp. 23–27, 2016.

[23] Y. Hu, Z. Li, and T. Lü, "Determination of elemental concentration in geological samples using nanosecond laser-induced breakdown spectroscopy," *Journal of Analytical Atomic Spectrometry*, vol. 32, no. 11, pp. 2263–2270, 2017.

[24] Y. Zhang, Y.and Li, W. Li, Z. Sun, and Y. Bi, "Classification of Geological Samples Based on Soft Independent Modeling of Class Analogy Using Laser-Induced Breakdown Spectroscopy," *Journal of Spectroscopy*, vol. 2018, 2018.

[25] T. Mainman, "Stimulated optical radiation in ruby," no. 187, pp. 493–494, 1960.

[26] F. Brech and L. Cross, "Optical microemission stimulated by a ruby laser," vol. 16, no. 59, 1962.

[27] J. Debras-Guédon and N. Liodec, "De l'utilisation du faisceau d'un amplificateur a ondes lumineuses par émission induite de rayonnement (laser à rubis), comme source énergétique pour l'excitation des spectres démission des éléments," *Comptes-Rendus de lAcadémie des Sciences*, vol. 257, pp. 3336–3339, 1963.

[28] P. D. Maker, R. W. Terhune, and C. M. Savage, "Optical third harmonic generation," in *Proc. 3rd Int. Conf. Quantum Electronics*, vol. 2. Columbia University Press, New York, 1964, p. 1559.

[29] E. F. Runge, R. W. Minck, and F. R. Bryan, "Spectrochemical analysis using a pulsed laser source," *Spectrochimica Acta*, vol. 20, no. 4, pp. 733 – 736, 1964. [Online]. Available: http://www.sciencedirect.com/science/article/pii/0371195164800709

[30] M. Young, M. Hercher, and C. Y. Yu, "Some characteristics of laser-induced air sparks," *Journal of Applied Physics*, vol. 37, pp. 4938–4940, 1966.

[31] C. Pasquini, J. Cortez, L. M. C. Silva, and F. B. Gonzaga, "Laser Induced Breakdown Spectroscopy," *Journal of the Brazilian Chemical Society*, vol. 18, no. 3, pp. 463–512, 2007. [Online]. Available: https://doi.org/10.1590/S0103-50532007000300002.

[32] D. A. Cremers and L. J. Radziemski, "Detection of chlorine and fluorine in air by laser-induced breakdown spectrometry," *Analytical Chemistry*, vol. 55, no. 8, pp. 1252–1256, 1983.

[33] L. J. Radziemski, D. A. Cremers, and T. R. Loree, "Detection of beryllium by laser induced breakdown spectroscopy," *Spectrochimica Acta Part B: Atomic Spectroscopy*, vol. 38, no. 1, pp. 349 – 353, 1983. [Online]. Available: http://www.sciencedirect.com/science/article/pii/0584854783801335

[34] L. J. Radziemski, T. R. Loree, D. A. Cremers, and N. M. Hoffman, "Time-resolved laser-induced breakdown spectrometry of aerosols," *Analytical Chemistry*, vol. 55, no. 8, pp. 1246–1251, 1983.

[35] D. A. Cremers and L. J. Radziemski, "Direct detection of beryllium on filters using the laser spark," *Applied Spectroscopy*, vol. 39, no. 1, pp. 57–60, 1985.

[36] D. A. Cremers, L. J. Radziemski, and T. R. Loree, "Spectrochemical analysis of liquids using the laser spark," *Applied Spectroscopy*, vol. 38, no. 5, pp. 721–726, 1984.

[37] D. A. Cremers, "The analysis of metals at a distance using laser-induced breakdown spectroscopy," *Applied spectroscopy*, vol. 41, no. 4, pp. 572–579, 1987.

[38] L. J. Radziemski and D. A. Cremers, "Laser-induced breakdown spectroscopy: principles, applications, and instruments," in *Optical Spectroscopic Instrumentation and Techniques for the 1990s: Applications in Astronomy, Chemistry, and Physics*, vol. 1318. International Society for Optics and Photonics, 1990, pp. 71–75.

[39] J. J. Zayhowski, "Passively Q-switched Nd: YAG microchip lasers and applications," *Journal of alloys and compounds*, vol. 303, pp. 393–400, 2000.

[40] W. Aslam Farooq, W. Tawfik, F. N. Al-Mutairi, and Z. A. Alahmed, "Qualitative analysis and plasma characteristics of soil from a desert area using LIBS technique," *Journal of the Optical Society of Korea*, vol. 17, no. 6, pp. 548–558, 2013.

[41] T. A. Labutin, S. M. Zaytsev, and A. M. Popov, "Automatic identification of emission lines in laser-induced plasma by correlation of model and experimental spectra," *Analytical Chemistry*, vol. 85, no. 4, pp. 1985–1990, 2013.

[42] S. Bashir, N. Farid, and K. Mahmood, "Influence of Ambient Gas and its Pressure on the Laser-induced Breakdown Spectroscopy and the Surface Morphology of Laser Ablated Cd," *Applied Physics A*, vol. 107, pp. 203–212, 2012.

[43] N. Idris, K. Lahna, and M. Ramli, "Study on Emission Spectral Lines of Iron, Fe in Laser-Induced Breakdown Spectroscopy (LIBS) on Soil Samples," *Journal of Physics: Conference Series*, vol. 846, no. 1, 2017.

[44] T. Hussain and M. A. Gondal, "Laser induced breakdown spectroscopy (LIBS) as a rapid tool for material analysis," *Journal of Physics: Conference Series*, vol. 439, no. 1, 2013.

[45] O. Svelto, *Principles of Lasers*, 5th ed. Elsevier, 2010.

[46] R. Paschotta, *Field Guide to Laser Pulse Generation*, 2008. [Online]. Available: https://doi.org/10.1117/3.800629

[47] "Q-Switching - RP Photonics Encyclopedia," accessed: October 26, 2020. [Online]. Available: https://www.rp-photonics.com/q_switching.html

[48] F. Anabitarte, A. Cobo, and J. López-Higuera, "Laser-Induced Breakdown Spectroscopy: Fundamentals, Applications, and Challenges," *ISRN Spectroscopy*, vol. 2012, 10 2012.

[49] M. F. L'Annunziata, "Chapter 8 - Electromagnetic Radiation: Photons," in *Radioactivity*, 2nd ed., M. F. L'Annunziata, Ed. Elsevier, 2016, pp. 269 – 302. [Online]. Available: http://www.sciencedirect.com/science/article/pii/B9780444634894000083

[50] S. J. Blundell and K. M. Blundell, *Concepts in thermal physics*. OUP Oxford, 2009.

[51] T. Takahashi and B. Thornton, "Quantitative methods for compensation of matrix effects and self-absorption in LIBS signals of solids," *Spectrochimica Acta - Part B Atomic Spectroscopy*, vol. 138, pp. 31–42, 2017. [Online]. Available: https://doi.org/10.1016/j.sab.2017.09.010

[52] N. Bonod and J. Neauport, "Diffraction gratings : from principles to applications in high-intensity lasers," *Advances in Optics and Photonics*, vol. 8, no. 1, pp. 156–199, 2016. [Online]. Available: https://hal.archives-ouvertes.fr/hal-01330435

[53] A. E. Paulick, "Development of Laser-Induced Breakdown Spectroscopy as a Rapid Diagnostic Tool for Bacterial Infection," 2018. [Online]. Available: https://scholar.uwindsor.ca/etd/7653

[54] "Avantes - how to choose the right grating," accessed: September 28, 2019. [Online]. Available: https://www.avantes.com/introductions/958-introduction-spectrometers/440-how-to-choose-the-right-grating

[55] "Mineralogy Database," accessed: June 2, 2020. [Online]. Available: http://www.webmineral.com

[56] Y. Hu, Z. Li, and T. Lü, "Determination of elemental concentration in geological samples using nanosecond laser-induced breakdown spectroscopy," *Journal of Analytical Atomic Spectrometry*, vol. 32, no. 11, pp. 2263–2270, 2017. [Online]. Available: http://dx.doi.org/10.1039/C7JA00239D

[57] A. Gupta, J. M. Curran, S. Coulson, and C. M. Triggs, "Comparison of intra-day and inter-day variation in LIBS spectra," *Forensic Chemistry*, vol. 3, pp. 36–40, 2017. [Online]. Available: http://dx.doi.org/10.1016/j.forc.2016.12.002

[58] D. Guimarães, M. L. Praamsma, and P. J. Parsons, "Evaluation of a new optic-enabled portable X-ray fluorescence spectrometry instrument for measuring toxic metals/metalloids in consumer goods and cultural products," *Spectrochimica Acta - Part B Atomic Spectroscopy*, vol. 122, pp. 192–202, 2016. [Online]. Available: http://dx.doi.org/10.1016/j.sab.2016.03.010

[59] C. L. Goueguel, "First-Order Multivariate Calibration in Laser-induced Breakdown Spectroscopy Laser-induced Breakdown Spectroscopy," 2019, accessed: September 15, 2020. [Online]. Available: https://towardsdatascience.com/first-order-multivariate-calibration-in-laser-induced-breakdown-spectroscopy-ca5616dd5b38

[60] J. Guezenoc, A. Gallet-Budynek, and B. Bousquet, "Critical review and advices on spectral-based normalization methods for LIBS quantitative analysis," *Spectrochimica Acta - Part B Atomic Spectroscopy*, vol. 160, no. June, p. 105688, 2019. [Online]. Available: https://doi.org/10.1016/j.sab.2019.105688

[61] J. P. Castro and E. R. Pereira-Filho, "Twelve different types of data normalization for the proposition of classification, univariate and multivariate regression models for the direct analyses of alloys by laser-induced breakdown spectroscopy (LIBS)," *Journal of Analytical Atomic Spectrometry*, vol. 31, no. 10, pp. 2005–2014, 2016.

[62] M. Thompson, S. L. R. Ellison, R. Wood *et al.*, "QUALITY ASSURANCE SCHEMES FOR ANALYTICAL LABORATORIES * HARMONIZED GUIDELINES FOR SINGLE- LABORATORY VALIDATION OF METHODS OF ANALYSIS (IUPAC Technical Report)," *Pure Appl Chem*, vol. 74, no. 5, pp. 835–855, 2002.

[63] M. A. Ismail, H. Imam, A. Elhassan, W. T. Youniss, and M. A. Harith, "LIBS limit of detection and plasma parameters of some elements in two different metallic matrices," *Journal of Analytical Atomic Spectrometry*, vol. 19, no. 4, pp. 489–494, 2004.

[64] J. El Haddad, L. Canioni, and B. Bousquet, "Good practices in libs analysis: Review and advices," *Spectrochimica Acta Part B: Atomic Spectroscopy*, vol. 101, pp. 171 – 182, 2014. [Online]. Available: http://www.sciencedirect.com/science/article/pii/S0584854714002158

[65] B. Sezer, H. M. Velioglu, G. Bilge, A. Berkkan, N. Ozdinc, U. Tamer, and I. H. Boyaci, "Detection and quantification of a toxic salt substitute (licl) by using laser induced breakdown spectroscopy (libs)," *Meat Science*, vol. 135, pp. 123 – 128, 2018. [Online]. Available: http://www.sciencedirect.com/science/article/pii/S030917401730918X

[66] "OSCAR-Optical Science Center for Applied Research at Delaware State University LIBS database," accessed: October 25, 2019. [Online]. Available: https://oscar.desu.edu/libs/

[67] "NIST Atomic Spectra Database Lines Form," accessed: July 8, 2019. [Online]. Available: https://www.physics.nist.gov/PhysRefData/ASD/lines_form.html

[68] R. Chandrappa and U. C. Kulshrestha, *Major Issues of Air Pollution*. Cham: Springer International Publishing, 2015, pp. 1–48. [Online]. Available: https://doi.org/10.1007/978-3-319-21596-9_1

[69] E. Tognoni and G. Cristoforetti, "Signal and noise in Laser Induced Breakdown Spectroscopy: An introductory review," *Optics Laser Technology*, vol. 79, pp. 164–172, 05 2016.

[70] J. Liu, R. Zhang, X. Li, J. Chen, J. Liu, J. Qiu, X. Gao, J. Cui, and B. Heshig, "Continuous background correction using effective points selected in third-order minima segments in low-cost laser-induced breakdown spectroscopy without intensified CCD," *Opt. Express*, vol. 26, no. 13, pp. 16 171–16 186, Jun 2018. [Online]. Available: http://www.opticsexpress.org/abstract.cfm?URI=oe-26-13-16171

[71] L. Sun and H. Yu, "Automatic estimation of varying continuum background emission in laser-induced breakdown spectroscopy," *Spectrochimica Acta - Part B Atomic Spectroscopy*, vol. 64, no. 3, pp. 278–287, 2009. [Online]. Available: http://dx.doi.org/10.1016/j.sab.2009.02.010

[72] P. H. C. Eilers and H. F. M. Boelens, "Baseline Correction with Asymmetric Least Squares Smoothing," 2005.

[73] P. H. C. Eilers, "Parametric Time Warping," *Analytical Chemistry*, vol. 76, no. 2, pp. 404–411, 2004.

[74] M. S. Friedrichs, "A model-free algorithm for the removal of baseline artifacts," *Journal of Biomolecular NMR*, vol. 5, no. 2, pp. 147–153, 1995.

[75] M. A. Kneen and H. J. Annegarn, "Algorithm for fitting XRF, SEM and PIXE X-ray spectra backgrounds," *Nuclear Instruments and Methods in Physics Research, Section B: Beam Interactions with Materials and Atoms*, vol. 109-110, pp. 209–213, 1996.

[76] K. H. Liland, T. Almøy, and B. H. Mevik, "Optimal choice of baseline correction for multivariate calibration of spectra," *Applied Spectroscopy*, vol. 64, no. 9, pp. 1007–1016, 2010.

[77] J. M. Li, L. B. Guo, C. M. Li, N. Zhao, X. Y. Yang, Z. Q. Hao, X. Y. Li, X. Y. Zeng, and Y. F. Lu, "Self-absorption reduction in Laser-Induced Breakdown Spectroscopy using laser-stimulated absorption," *Optics Letters*, vol. 40, no. 22, p. 5224, 2015.

[78] E. W. Weisstein, "Gaussian Function. From MathWorld–A Wolfram Web Resource," accessed: March 25, 2020. [Online]. Available: https://mathworld.wolfram.com/GaussianFunction.html

[79] E. W. Weisstein, "Lorentzian Function. From MathWorld–A Wolfram Web Resource," accessed: March 25, 2020. [Online]. Available: https://mathworld.wolfram.com/LorentzianFunction.html

[80] "Scipy Voigt Profile," accessed: March 25, 2020. [Online]. Available: https://docs.scipy.org/doc/scipy-1.4.0/reference/generated/scipy.special.voigt_profile.html

[81] "Montebrasite," accessed: August 30, 2020. [Online]. Available: https://www.mindat.org/photo-380193.html

[82] "Turquoise," accessed: August 30, 2020. [Online]. Available: https://www.minerals.net/mineral/turquoise.aspx

[83] R. Gourvennec, J. M. Piçarra, Y. Plusquellec, Z. Pereira, J. T. Oliveira, and M. Robardet, "Lower Devonian faunas and palynomorphs from the Dornes Syncline (Central Iberian Zone, Portugal): stratigraphical and paleogeographical implications."

[84] C. Inverno and M. L. Ribeiro, "Fraturação e cortejo filoneano nas Minas da Argemela (Fundão)," *Com. Serv. Geolo. Portugal, t.66*, pp. 185–193, 1980.

[85] P. A. B. Fernando and J. A. Sampaio, *Rochas & minerais industriais: usos e especificações*, 2nd ed. CETEM/MCT, 2008. [Online]. Available: http://mineralis.cetem.gov.br/bitstream/cetem/1115/1/26.LITIO.pdf

[86] A. G. Collins, "Lithium abundances in oilfield waters," *U.S. Geological Survey Professional Paper*, pp. 116–123, 1976.

[87] S. Mishra, U. Sarkar, S. Taraphder, S. Datta, D. Swain, R. Saikhom, S. Panda, and M. Laishram, "Multivariate Statistical Data Analysis- Principal Component Analysis (PCA)," *International Journal of Livestock Research*, no. January, p. 1, 2017. [Online]. Available: http://www.ejmanager.com/fulltextpdf.php?mno=261590

[88] I. T. Jollife and J. Cadima, "Principal component analysis: A review and recent developments," *Philosophical Transactions of the Royal Society A: Mathematical, Physical and Engineering Sciences*, vol. 374, no. 2065, 2016.

[89] A. Kassambara, *Practical Guide To Principal Component Methods in R: PCA, M(CA), FAMD, MFA, HCPC, factoextra*, ser. Multivariate Analysis. STHDA, 2017, vol. 2. [Online]. Available: https://books.google.pt/books?id=eFEyDwAAQBAJ

[90] K. H. Lepore, C. I. Fassett, E. A. Breves, S. Byrne, S. Giguere, T. Boucher, J. M. Rhodes, M. Vollinger, C. H. Anderson, R. W. Murray, and M. D. Dyar, "Matrix Effects in Quantitative Analysis of Laser-Induced Breakdown Spectroscopy

(LIBS) of Rock Powders Doped with Cr , Mn , Ni , Zn , and Co," vol. 71, no. 4, pp. 1–27, 2017.

[91] P. Devangad, V. K. Unnikrishnan, M. M. Tamboli, K. M. M. Shameem, R. Nayak, K. S. Choudhari, and C. Santhosh, "Quantification of Mn in glass matrices using laser induced breakdown spectroscopy (LIBS) combined with chemometric approaches," *Analytical Methods*, vol. 8, no. 39, pp. 7177–7184, 2016. [Online]. Available: http://dx.doi.org/10.1039/C6AY01930G

[92] G. Guo, G. Niu, Q. Shi, Q. Lin, D. Tian, and Y. Duan, "Multi-element quantitative analysis of soils by laser induced breakdown spectroscopy (LIBS) coupled with univariate and multivariate regression methods," *Analytical Methods*, vol. 11, no. 23, pp. 3006–3013, 2019.

[93] "Neural network models (supervised)," acessed: October 7, 2020. [Online]. Available: https://scikit-learn.org/stable/modules/neural_networks_supervised.html

[94] I. Goodfellow, Y. Bengio, and A. Courville, *Deep Learning*. MIT Press, 2016. [Online]. Available: http://www.deeplearningbook.org

[95] C. Sammut and G. I. Webb, *Encyclopedia of Machine Learning*. Springer, 2010.